An Investigation of the Higgs Boson Production Channel $t\bar{t}H^0$, $H^0 \rightarrow b\bar{b}$ with the ATLAS Detector at the LHC

Janice Gail Drohan
University College London

A thesis submitted for the degree of Doctor of Philosophy
of the University of London

May, 2006

DECLARATION

I confirm that the work presented in this thesis is my own. Where information has been derived from other sources, I confirm that this has been indicated in the thesis.

Janice Gail Drohan

An Investigation of the Higgs Boson Production Channel $\mathbf{t\bar{t}H^0}$, $\mathbf{H^0 \rightarrow b\bar{b}}$ with the ATLAS Detector at the LHC

Janice Gail Drohan
University College London

Submitted for the degree of Doctor of Philosophy
at the University of London
May, 2006

ABSTRACT

The Large Hadron Collider, due for completion at the end of 2007, will provide an essential piece in the puzzle of electroweak symmetry breaking. Precision measurements from LEP predict a low mass Standard Model Higgs boson close to the current experimental lower limit. In this mass region identification of the Higgs boson will be difficult, requiring more than one channel to be studied. $t\bar{t}H^0, H^0 \rightarrow b\bar{b}$ is one of three channels proposed for this purpose. In order to reduce the large backgrounds full reconstruction of the two top-quarks in the event is necessary. This thesis investigates a number of new techniques to improve the reconstruction procedure of this channel using the fast simulation of the ATLAS detector, Atlfast. Methods investigated include the introduction of hadronic W candidates created from three jets combined with a new energy rescaling method for the W candidates. A new quantity to choose the jet pairings in the event, utilising jet and lepton energy uncertainties from Atlfast, is studied. An Artificial Neural Network is trained to select signal from background events. An increase in the expected signal significance from 1.8 to 2.4 for an integrated luminosity of 30fb^{-1} and Higgs mass of 120GeV is observed from the techniques proposed.

An important tool for any high energy physics experiment is an event display program. Visual representation is the most efficient way to transfer data from a computer to the human brain, providing the user with a powerful tool to investigate specific events. The Atlantis event display for the ATLAS experiment is presented, along with the development carried out to enable its use in the 2004 Combined Test Beam. The test beam used a full slice of the detector to provide an essential study of the performance capabilities of ATLAS.

Dedicated to my Parents

ACKNOWLEDGEMENTS

I'd like to thank my supervisor, Nikos Konstantinidis, for his help and advice over the last three and a half years and for providing opportunities to get involved in a range of interesting projects. I'd also like to thank the UCL Atlas group, especially Jon Butterworth, Mark Sutton and Simon Dean for their advice and suggestions during weekly physics meetings and Erkcan Ozcan for his time spent proof reading this thesis.

Thanks to all the UK students based at CERN for making my year there so enjoyable, especially to James Catmore and James Storey for some fantastic weekends hiking in the Alps. Thanks to Brinick Simmons for being a good friend, I couldn't have asked for a better person to share an office with. Joanna Fabbri and Fabrizio Sidoli, for some great nights out and many bottles of wine when they were needed most.

Thanks to my family for their unwavering support and encouragement throughout my life, especially my parents for all the opportunities they have provided. Lastly and most importantly, I'd like to thank Daniel Lister, for always being there, giving good advice, listening, having incredible patience and for keeping me smiling during the last six months of this PhD. I owe you so much!

Contents

List of Figures

List of Tables

CHAPTER 1

Introduction

In 2007 the ATLAS detector, one of the experiments for the Large Hadron Collider (LHC) at the European Organisation for Nuclear Research (CERN), will commence data collection. One of the primary goals of the experiment is to answer the question of how particles acquire mass. In our current understanding of particle physics, the Standard Model (SM), the mechanism by which this occurs necessitates the existence of a particle known as the Higgs boson. The mass of the Higgs boson, should it exist, is a free parameter of the SM. Previous searches for the particle at the LEP experiment have ruled out a mass below 114.4GeV [1], providing a hint of a signal at 115GeV [2, 3, 4, 5]. The LHC, colliding proton beams with an energy of 7TeV, will extend the search for the Higgs over the full range of possible masses. If the Higgs boson does exist it should be discovered at the LHC.

Precision measurements also made at LEP indicate that the Higgs mass should be close to the current experimental lower limit [6]. This mass range is one of the most difficult for ATLAS with three different production and decay channels contributing, with similar sensitivity, to a discovery. One of these channels involves Higgs production with an associated top-quark pair, where the Higgs boson decays to b-quarks. Investigation of possible improvements to the significance of this channel is the focus of this thesis.

An important tool for any high energy physics experiment is an event display program. Visual representation is the most efficient way to transfer data from a computer to the human brain, providing the user with a powerful tool to investigate specific events. This may include checking pattern recognition and analysis algorithms, obtaining an understanding of events and possible problems as well as selecting events to display in talks and papers. Development of the Atlantis event display and its adaptation for use in the 2004 Combined Test Beam was carried out as part of this thesis. In total, just over a year of this docterate was spent working on the Atlantis project.

An overview of the SM and the Higgs mechanism are provided in the first sections of chapter 2. The latter sections review the important discovery channels for different Higgs mass scenarios at the ATLAS detector. A description of the ATLAS detector is given in chapter 3 and the Atlantis event display is presented in chapter 4. Chapter 5 describes the event generation and simulation processes used to create the data samples for this study and the results of the analysis carried out are contained in chapter 6.

CHAPTER 2

Theory and Motivation

The Standard Model (SM) [7, 8] is our current understanding of the fundamental constituents that make up the Universe and their interactions with one another. It has been extremely successful at explaining and predicting the results of a wide range of experiments over the last thirty years. However, one aspect of the model that still remains unconfirmed is how the fundamental constituents acquire their mass. This chapter provides a brief introduction to the Standard Model followed by an overview of the mechanism proposed in 1964 to allow massive particles within the model. The main aim of the ATLAS experiment is to confirm the existence of the Higgs boson, a particle resulting from this mechanism. The final sections of this chapter describe the current theoretical and experimental constraints upon the Higgs mass and review the discovery potential of this particle at the LHC.

2.1 The Standard Model

2.1.1 Particles and Forces

The Standard Model describes all matter and interactions in terms of point-like particles with internal angular momentum characterised by the spin quantum number, s. All matter is made of fermions, particles with half-integer spin, and the forces that govern their interactions are mediated by bosons, particles with integer spin.

The fermions can be sub-divided into two categories, quarks and leptons. This distinction is made on the basis of their interactions: quarks carry the colour charge associated with the strong interaction whereas leptons do not. Quarks and leptons occur in six 'flavours'. These are presented in table 2.1, arranged in three generations of progressively more massive doublets. For each particle there exists an anti-particle with identical mass but opposite quantum numbers. Ordinary matter consists only of the lightest two quarks (u and d) and the lightest charged lepton (the electron).

	1st Generation	2nd Generation	3rd Generation
Quarks	u(up) d(down)	c(charm) s(strange)	t(top) b(bottom)
Leptons	ν_e(e-neutrino) e(electron)	ν_μ(μ-neutrino) μ(muon)	ν_τ(τ-neutrino) τ(tau)

Table 2.1: Fundamental constituents of fermionic matter.

Of the four types of interactions that are present in the Universe, three are included in the Standard Model. These are the electromagnetic interaction mediated by the massless photon, the weak force mediated by the massive $\mathrm{W}^{\pm}$ and Z^0 bosons and the strong interaction mediated by eight massless gluons. At the scale of typical particle masses the gravitational force is too weak to have any significant effect.

The range of each force is inversely proportional to the mass of the mediating boson. The electromagnetic force has infinite range while the weak force has a range limited to $\sim 10^{-18}$m. The strong force, although mediated by massless gluons, is limited to $\sim 10^{-15}$m. This is due to the self-interaction of gluons which causes the strength of the strong interaction to increase with distance. As quarks are separated the potential energy between them increases until it is favourable for the field to form new quark anti-quark pairs, continuing until all the quarks are bound within colourless objects. These objects can be either mesons ($q\bar{q}$) or baryons (qqq).

2.1.2 Symmetries and Gauge Theories

The Standard Model [7, 8] is a description of the strong, weak and electromagnetic interactions as 'gauge theories'. Such theories require invariance of the system under a set of local transformations: transformations that depend on position in space and time. This is related to the idea that conserved physical quantities, such as electric charge, are conserved in local regions of space and not just globally.

In the case of electromagnetism the gauge transformations in question are local complex phase transformations of the fields of charged particles. Consider the Lagrangian for a free electron of mass m, described by the Dirac Spinor ψ.

$$\mathcal{L} = \bar{\psi}(i\gamma^\mu\partial_\mu - m)\psi \tag{2.1}$$

If we impose the requirement of invariance under the local gauge transformation $\psi \rightarrow \psi' = e^{iQ\theta(x)}\psi$, where Q, the charge, is the generator of the $\mathrm{U(1)_Q}$ symmetry group, we are forced to introduce a vector field A^μ, which we subsequently associate with the photon field coupling to the electron with strength e. The resulting Lagrangian,

$$\mathcal{L}_{QED} = \underbrace{i\bar{\psi}\gamma^\mu\partial_\mu\psi}_{E_{kin}\ of\ \psi} - \underbrace{m\bar{\psi}\psi}_{Mass\ of\ \psi} + \underbrace{e\bar{\psi}\gamma^\mu\psi A_\mu}_{Interaction} - \underbrace{\frac{1}{4}F_{\mu\nu}F^{\mu\nu}}_{E_{kin}\ of\ A^\mu} \tag{2.2}$$

where $F_{\mu\nu} = \partial_\mu A_\nu - \partial_\nu A_\mu$, does not contain a mass term for the photon, predicting a massless gauge boson, as observed. The effect of requiring this invariance has been to transform the free system into an interacting one.

The Standard Model Lagrangian is invariant under local gauge transformations of the symmetry groups $\mathrm{SU(2)_L \otimes U(1)_Y}$ and $\mathrm{SU(3)}_C$. The strong force is described by quantum chromodynamics (QCD) and is based on the SU(3) symmetry group. The eight generators of the group correspond to the eight massless gluons. The electroweak Lagrangian corresponds to a $\mathrm{SU(2)}_L$ symmetry describing rotations in weak isospin space and a U(1) symmetry representing hypercharge transformations. Hypercharge Y is related to the electromagnetic charge Q and the third component of weak isospin T^3 by the relation $Q=T^3+Y/2$. There are four group generators in total, all predicted to be massless by the electroweak Lagrangian. This poses a problem as the $W^{\pm}$ and Z^0 bosons are known to be massive from experimental data. A solution to this lies in the concept of spontaneous symmetry breaking.

2.2 The Higgs Mechanism

The Standard Model in its early form was a theory of massless particles. The mechanism of spontaneous symmetry breaking proposed by Higgs [9, 10], Brout and Englert [11] and others [12] enabled the generation of massive gauge bosons in the theory whilst retaining its local gauge invariance.

The simplest way to illustrate the idea of spontaneous symmetry breaking is to consider the case of a needle placed upright upon a table with a small force applied downward along its axis. In this situation the needle is completely symmetric with respect to rotations around its axis. If the force upon the needle is increased it will eventually reach a point where it will bend and break. At this point, the needle can bend in any direction to reach a ground state with the same energy. In choosing the direction in which to buckle the needle will break the rotational symmetry of the system. It is this process that is known as spontaneous symmetry breaking.

To demonstrate this principle in terms of a gauge theory, consider the case of a complex scalar field $\phi = (\phi_1 + i\phi_2)/\sqrt{2}$ described by the Lagrangian:

$$\mathcal{L} = \underbrace{(\partial_\mu\phi)^*(\partial_\mu\phi)}_{\text{kinetic } T(\phi)} - \underbrace{(\mu^2\phi^*\phi + \lambda(\phi^*\phi)^2)}_{\text{potential } V(\phi)} \tag{2.3}$$

To make this Lagrangian invariant under the U(1) local gauge transformation, $\phi \to e^{-i\alpha(x)}\phi$, ∂_μ must be replaced by the covariant derivative $D^\mu = \partial_\mu - ieA_\mu$ where the gauge field transforms as $A_\mu \to A_\mu + \frac{1}{e}\partial_\mu\alpha$. The gauge invariant Lagrangian is therefore:

$$\begin{gathered}\mathcal{L} = (D_\mu\phi)^*(D_\mu\phi) - \mu^2\phi^*\phi - \lambda(\phi^*\phi)^2 - \frac{1}{4}F_{\mu\nu}F^{\mu\nu} \\ \text{where } F_{\mu\nu} = \partial_\mu A_\nu - \partial_\nu A_\mu.\end{gathered} \tag{2.4}$$

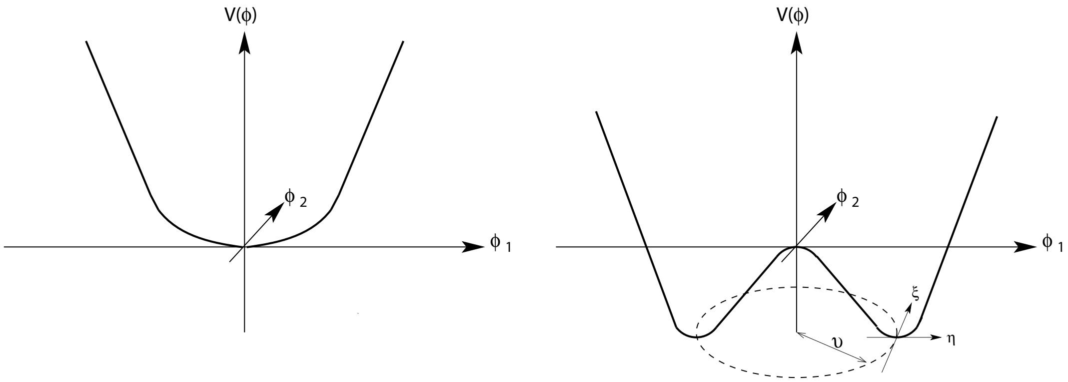

Figure 2.1: The potential V(ϕ) for a complex scalar field for the case where $\lambda > 0$ and (a) $\mu^2 > 0$ (b) $\mu^2 < 0$.

The potential of the field, assuming $\lambda > 0$, is shown in figure 2.1 for the cases where $\mu^2 > 0$ and $\mu^2 < 0$. In the case of $\mu^2 > 0$ the potential has a minimum at $\phi = 0$, however the situation becomes more interesting if $\mu^2 < 0$. In this case, $\phi = 0$ is a maximum and the minimum of the potential is given by a circle in the ϕ_1, ϕ_2 plane of radius ν, such that:

$$\phi_1^2 + \phi_2^2 = \nu^2 \text{ with } \nu^2 = -\frac{\mu^2}{\lambda}. \tag{2.5}$$

There are now an infinite number of states with the same lowest energy; the same situation as the needle example. If we translate the field ϕ to a minimum energy position at $\phi_1 = \nu$, $\phi_2 = 0$ we can define a new set of fields η and ξ:

$$\phi(x) = \sqrt{\frac{1}{2}}[\nu + \eta(x) + i\xi(x)] \tag{2.6}$$

where $\phi_1(x) \equiv \nu + \eta(x)$ and $\phi_2(x) \equiv \xi(x)$. The Lagrangian can now be expanded about the vacuum in terms of these fields by substituting equation 2.6 into equation 2.4 to give:

$$\begin{aligned} \mathcal{L}' = \frac{1}{2}(\partial_\mu \xi)^2 + \frac{1}{2}(\partial_\mu \eta)^2 - \nu^2 \lambda \eta^2 + \frac{1}{2} e^2 \nu^2 A_\mu A^\mu \\ - e\nu A_\mu \partial^\mu \xi - \frac{1}{4} F_{\mu\nu} F^{\mu\nu} + \textit{interaction terms}. \end{aligned} \tag{2.7}$$

The Lagrangian now contains terms representing the desired massive vector boson A$_\mu$, a massive scalar η and also what appears to be a massless boson ξ, known as a Goldstone boson. By giving a mass to A$_\mu$ the particle's polarisation degrees of freedom have been increased from two to three. Simply translating variables should not create a new degree of freedom. This suggests that the fields in equation 2.7 are not distinct physical particles. Since the difficulties in the Lagrangian involve the field $\xi \equiv \phi_2(x)$, a suitable gauge transformation can be chosen to eliminate $\phi_2(x)$. Writing the U(1) transform in terms of its real and imaginary parts:

$$\begin{aligned} &\phi \rightarrow \phi' = e^{-i\theta(x)}\phi \\ &\phi \rightarrow \phi' = (\cos\theta(x) + i\sin\theta(x))(\phi_1 + i\phi_2) \\ &\qquad\quad = (\phi_1\cos\theta(x) - \phi_2\sin\theta(x)) + i(\phi_1\sin\theta - \phi_2\cos\theta(x)) \end{aligned} \tag{2.8}$$

identifies the suitable gauge to be $\theta = -\tan^{-1}(\phi_2/\phi_1)$. This combined with the approximation:

$$\begin{aligned} \phi &= \sqrt{\frac{1}{2}}(\nu + \eta + i\xi) \\ &\approx \sqrt{\frac{1}{2}}(\nu + \eta)e^{i\xi/\nu}, \end{aligned} \tag{2.9}$$

to lowest order in ξ, points to a different set of real fields h, θ, A_μ (equation 2.10) being substituted into equation 2.4.

$$\begin{aligned} \phi &\rightarrow \sqrt{\frac{1}{2}}(\nu + h(x))e^{i\theta(x)/\nu} \\ A_\mu &\rightarrow +\frac{1}{e\nu}\partial_\mu\theta \end{aligned} \tag{2.10}$$

From this we obtain a Lagrangian (equation 2.11) describing just two interacting massive particles, a vector gauge boson, A$_\mu$, with m$_A$ = $e\nu$ and a massive scalar boson, h, with m$_h$=$\sqrt{2\lambda\nu^2}$. The unwanted massless Goldstone boson has been turned into the extra degree of freedom for the original gauge boson allowing it to become massive. This is known as the Higgs mechanism; by introducing a complex scalar Higgs field with two additional degrees of freedom, we have provided one of the degrees of freedom to the A$_\mu$ boson to allow it to become massive and the other becomes a massive scalar boson, known as the Higgs boson.

$$\begin{aligned} \mathcal{L}'' =& \frac{1}{2}(\partial_\mu h)^2 - \lambda\nu^2h^2 + \frac{1}{2}e^2\nu^2A_\mu^2 - \lambda\nu h^3 - \frac{1}{4}\lambda h^4 \\ &+ \frac{1}{2}e^2A_\mu^2h^2 + \nu e^2A_\mu^2h - \frac{1}{4}F_{\mu\nu}F^{\mu\nu} \end{aligned} \tag{2.11}$$

It is important to note that the Lagrangians 2.11 and 2.3 describe exactly the same physical system, it is just in the ground state that the U(1) symmetry of the system becomes 'hidden'.

Returning to the case of the electroweak Lagrangian, the SU(2) group has three generators which correspond to the gauge bosons $\{\mathrm{W}^1_\mu,\ \mathrm{W}^2_\mu,\ \mathrm{W}^3_\mu\}$ and a coupling denoted by g. The U(1) group has one boson B_μ and a coupling g′. The relative strength of these interactions is determined according to $g' = g\tan\theta_W$, where θ_W is the weak mixing angle.

The physical electroweak bosons $\mathrm{W}^\pm$, Z and γ correspond to linear superpositions of the gauge fields,

$$\begin{aligned} W^\pm &\equiv (W^1_\mu \mp iW^2_\mu)/\sqrt{2} \\ Z_\mu &\equiv cos\theta_W W^3_\mu - sin\theta_W B_\mu \\ A_\mu &\equiv cos\theta_W B_\mu + sin\theta_W W^3_\mu \end{aligned} \tag{2.12}$$

of which only the Z and W acquire mass through the Higgs mechanism. In order to break the $\mathrm{SU(2)_L \otimes U(1)_Y}$ symmetry a doublet of complex fields is introduced (equation 2.13) providing four extra degrees of freedom.

$$\phi = \begin{pmatrix} \phi^+ \\ \phi^0 \end{pmatrix} = \sqrt{\frac{1}{2}} \begin{pmatrix} \phi_1 + i\phi_2 \\ \phi_3 + i\phi_4 \end{pmatrix} \tag{2.13}$$

During spontaneous symmetry breaking, three of the extra degrees of freedom are given to the $\mathrm{W}^\pm$ and Z bosons allowing them to become massive and the other corresponds, as before, to a massive scalar Higgs boson. The photon remains massless as the electroweak Lagrangian remains invariant under local $\mathrm{U(1)}_{em}$ transformations with generator Q.

An explicit mass term for the fermions cannot be present in the Lagrangian as this would mix the right-handed and left-handed states that must be treated separately for the weak interaction. However, it is possible to have an interaction between the left handed fermion doublet, the right-handed fermion singlet and the scalar doublet (Higgs field), Φ. These interactions are known as Yukawa interactions and have the form:

$$\mathcal{L}_{Yukawa} = G_f(\bar{\psi}_L \Phi \psi_R + \bar{\psi}_R \Phi \psi_L) \tag{2.14}$$

where G_f is the coupling constant of the interaction.

The Yukawa interaction for the electron in the unitary gauge is given by:

$$\mathcal{L}_{Yukawa} = -\frac{G_e}{\sqrt{2}} \begin{pmatrix} \bar{\nu_L} \\ \bar{e_L} \end{pmatrix}^T \begin{pmatrix} 0 \\ v + H \end{pmatrix} e_R + \text{hermitian conjugate} \tag{2.15}$$

This results in two terms:

$$\frac{G_e v}{\sqrt{2}} \bar{e} e - \frac{G_e}{\sqrt{2}} \bar{e} H e \tag{2.16}$$

the first is a mass term for the electron, which is proportional to the vacuum expectation of the scalar field. From this we obtain a relation for the Yukawa coupling in terms of the electron mass, m_e, and the W boson mass, M_W:

$$G_e = g \frac{m_e}{\sqrt{2} M_W} \tag{2.17}$$

The second term gives the coupling between the electron and the scalar Higgs field, from which we can see that the coupling is proportional to the electron mass. In a similar way the quarks also acquire a mass through their Yukawa couplings with the Higgs field, with those couplings proportional to their mass.

A more detailed treatment of the Standard Model and the Higgs mechanism can be found in the books [13, 14, 15].

2.3 Constraints on the mass of the Higgs boson

The experimental observation of the Higgs boson is one of the most important physics goals of the ATLAS experiment. The Higgs mechanism allows the fundamental particles (leptons, quarks and gauge bosons) to remain weakly interacting up to high energies without violating the unitarity bounds of scattering amplitudes. These unitarity requirements determine the couplings of the Higgs boson to all other particles. Since all the couplings are predetermined the properties of the Higgs boson are fixed by its mass, which is the only unknown parameter of the Standard Model Higgs sector. Once the Higgs mass is known, all decay widths and production processes of the Higgs particle will be uniquely determined [16].

Although the Higgs boson mass is not theoretically predicted, it is constrained in two ways. Since the quartic self-coupling of the Higgs field grows indefinitely with rising energy, an upper limit on the Higgs mass is obtained by demanding that the SM particles remain weakly interacting up to a scale Λ. A lower limit on the Higgs mass can be derived from the requirement of stability of the electroweak vacuum [17, 18, 19]. Hence, if the Standard Model is assumed to be valid up to the Planck scale (no new physics appears up to that scale) then the Higgs boson mass is required to be in the range $130 < \mathrm{m_H} < 190$GeV. This bound becomes weaker if new physics appears at lower masses. If Λ is chosen to be 1TeV, the Higgs boson mass is constrained to be in the range $50 < \mathrm{m_H} < 800$GeV.

During the second phase of the LEP experiment at CERN, known as LEP2, a centre of mass energy of $\sqrt{s} = 209$GeV was achieved. The dominant production mechanism for the SM Higgs boson at this energy is the Higgs-strahlung process $e^+e^- \rightarrow Z^* \rightarrow ZH$. LEP2 carried out direct searches for the Higgs boson and established a lower bound of $\mathrm{m_H} > 114.4$GeV at the 95% confidence level [1]. Global fits to high precision electroweak data can also be used to indirectly constrain the Higgs mass via their sensitivity to higher order diagrams involving Higgs loops. Assuming the validity of the Standard Model, LEP2 data gives $\mathrm{m_H} = 89^{+42}_{-30}$GeV [6] (see figure 2.2). These data suggest that the Higgs mass is very close to the current experimental limit. At the time LEP2 was shut down, a potential signal had been observed at $\mathrm{m_H} = 115.0^{+1.3}_{-0.7}$GeV (90% confidence range) [2, 3, 4, 5].

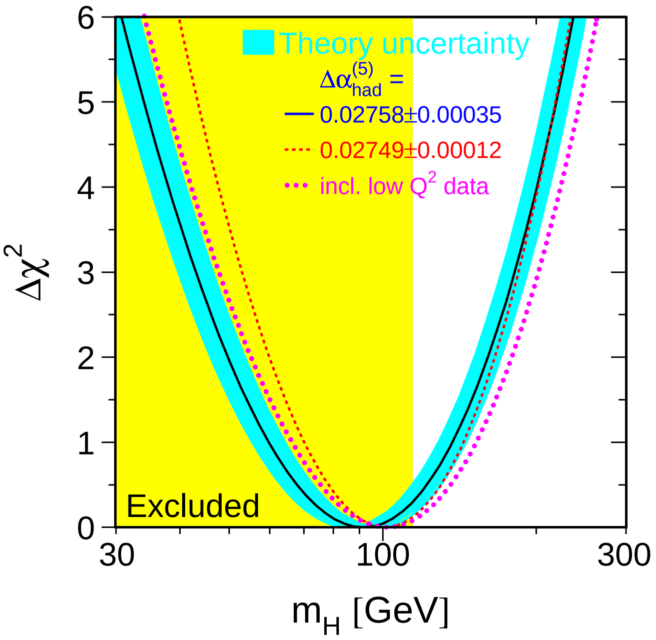

Figure 2.2: $\Delta\chi^2(m_H) = \chi^2_{min}(m_H) - \chi^2_{min}$ as a function of m_H [6]. The line is the result of the fit using 18 parameters. The associated band represents the estimate of the theoretical uncertainty due to missing higher-order corrections. The vertical band shows the 95% exclusion limit on m_H of 114.4 GeV.

2.4 Higgs Production and Decay at the LHC

There is no single production mechanism or decay process which dominates over the potential Higgs mass range (100GeV to 1TeV) observable with ATLAS. Several different discovery scenarios exist depending on the mass of the Higgs particle.

There are several Higgs production methods at the LHC that have the potential to lead to observable cross-sections. These include:

- gluon-gluon fusion
- WW and ZZ fusion
- Associated production with W and Z bosons
- Associated production with $t\bar{t}$

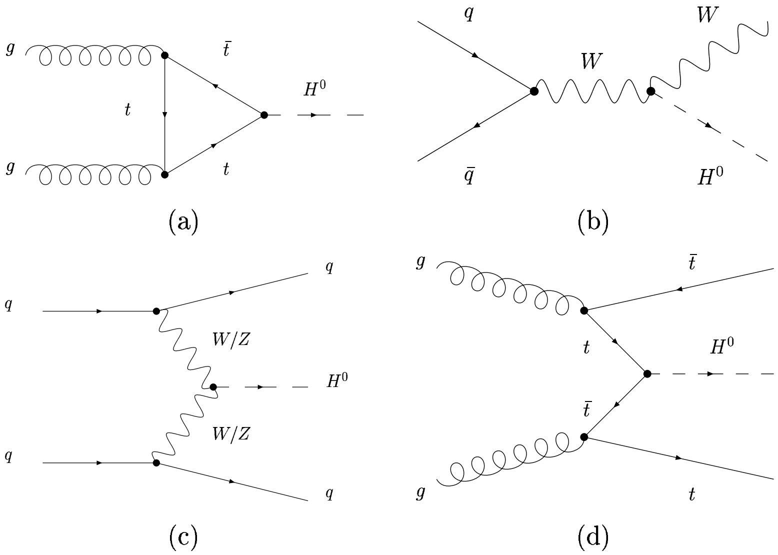

Figure 2.3: Higgs production diagrams at the LHC: (a) gluon-gluon fusion, (b) associated production with W (or) Z bosons (c) WW and ZZ fusion and (d) associated production with $\mathrm{t\bar{t}}$.

Figure 2.3 shows the Feynman diagrams for these production methods and figure 2.4 is a plot of the cross-sections as a function of the Higgs mass. The dominant Higgs production mechanism at the LHC will be the gluon fusion process which provides the largest production cross-section for the whole Higgs mass range of interest. For large Higgs masses the W and Z boson fusion processes become competitive and, at the lower end of the range, associated production with top quarks or W/Z bosons will provide alternative signatures for the search.

The decay of the Higgs boson after production depends on its mass. The Higgs couples preferentially to heavy particles so it decays primarily into the highest mass particles energetically allowed. Figure 2.5 shows the branching ratios of the Higgs boson as a function of its mass. For Higgs masses below ~140 GeV, the dominant decay mode is $b\bar{b}$ with a branching ratio up to 85%. From $\mathrm{m_H}\approx$140 GeV, the WW decay takes over the dominant role along with the ZZ decay mode. When the W pair becomes on-shell the ZZ branching ratio drops down to a level of 2%, rising again to a branching ratio of 30% above the ZZ threshold. Above the $\mathrm{t\bar{t}}$ threshold ($\mathrm{m_H}$= $2\mathrm{m_t}$), the $\mathrm{t\bar{t}}$ decay mode opens up to a maximum branching ratio of 20%. This is restricted due to leading WW and ZZ decay widths that grow with the third power

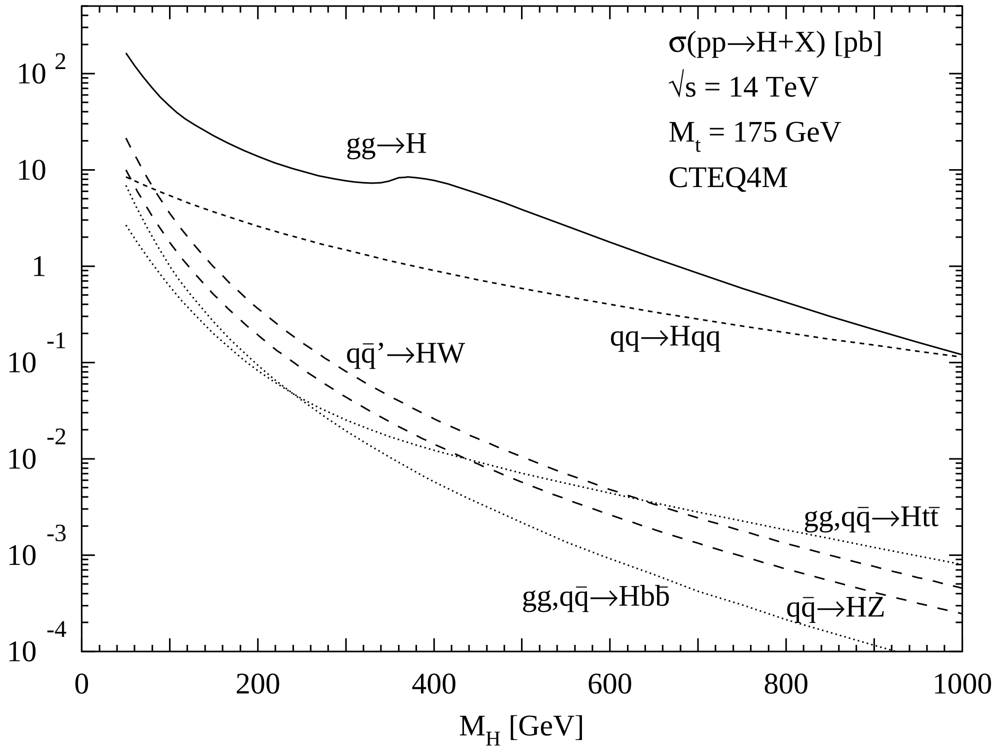

Figure 2.4: Higgs production cross-sections as a function of Higgs mass [16].

of the Higgs mass (due to the longitudinal W, Z components, which dominate for large Higgs masses), whereas the $t\bar{t}$ decay width increases only with the first power. Consequently, the total Higgs width grows rapidly at large Higgs masses and reaches a level of 600 GeV at m_H= 1TeV.

The above phenomenology leads to differing search strategies within three major mass ranges at the LHC. The most important channels within these ranges for ATLAS [20] are summarised below:

$\mathbf{m_H < 130}$ GeV

The dominant decay process within this mass range is to $b\bar{b}$ pairs. However, due to the large QCD background the signal from direct Higgs production will be very difficult to extract. When the Higgs boson is produced in association with a pair of top quarks it is possible to overcome this problem by requiring an isolated lepton in the event from a top decay. This is one of three channels that will contribute with similar sensitivity to a discovery in this mass region. The other two are $H \rightarrow \gamma\gamma$

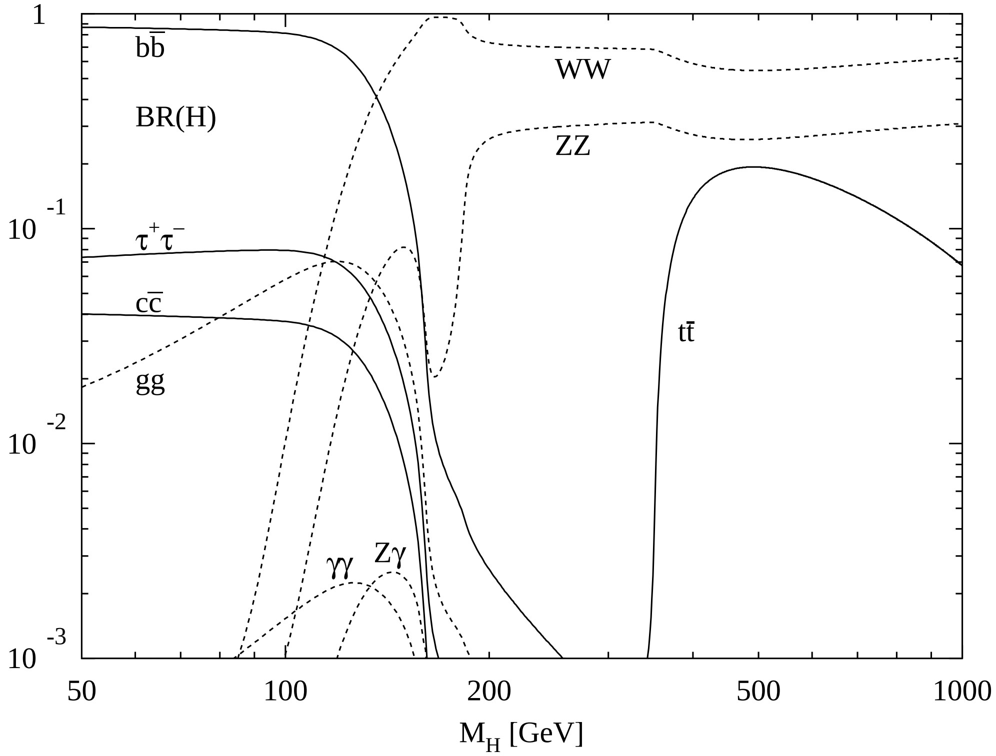

Figure 2.5: Branching ratios of the dominant decay modes of the SM Higgs particle [16].

(direct production) and $H \rightarrow \tau\tau$ (vector boson fusion) [21]. $H \rightarrow \gamma\gamma$ is a rare decay mode that requires excellent energy and angular resolution to observe its narrow mass peak above the irreducible prompt $\gamma\gamma$ continuum. Vector boson fusion is characterised by two opposite, high-p_T jets in the forward region with little central jet activity. The Higgs decay mode $H \rightarrow \tau\tau \rightarrow l\nu l\nu$ produced via vector boson fusion can be effectively discriminated from its backgrounds using a central jet veto.

$\mathbf{130 < m_H < 180}$ GeV

In this mass region the WW decay mode opens up, suppressing the ZZ mode. The channel $H \rightarrow WW(^*) \rightarrow l^+l^-\nu\bar{\nu}$, where the Higgs is produced via vector boson fusion has a signal significance greater than 5σ over the entire mass range for an integrated luminosity of 30fb^{-1}. In the mass region $155<\text{m}_\text{H}<180$GeV another possibility arises from direct Higgs production with the same decay mode. In this channel it is not possible to reconstruct the mass peak, instead an excess of events may be observed and then used to identify the presence of a Higgs boson signal and to extract information on its mass.

$180 < \mathbf{m_H} < 1$ TeV

For the Higgs boson mass range 180<$\mathrm{m_H}$<700GeV, the 'gold-plated' channel $H \to ZZ \to 4l$ provides the most reliable signal for the discovery of a Higgs boson at the LHC. The expected background, which is dominated by the continuum production of Z boson pairs, is smaller than the signal. The momenta of the final state leptons are high and their measurement does not place severe requirements on the detector performance. The discovery potential in this channel is primarily determined by the available integrated luminosity.

For Higgs masses above 800 GeV the $H \to ZZ \to 4l$ decay mode has too small a rate to be used. To access this mass range it is necessary to look for decays containing neutrinos and jets in the final state. Important processes are $H \to ZZ \to l^+l^-\nu\bar{\nu}$ and $H \to WW \to l\nu jj$. These channels require excellent $\not{E}_\mathrm{T}$ measurements and accurate reconstruction of $W/Z \to jj$ decays. At these Higgs masses, vector boson fusion becomes an important production mechanism comparable with the gluon fusion process. The features which distinguish this from other production mechanisms are the presence of two energetic forward jets in the final state and the lack of colour interchange between the initial state quarks. This causes suppressed hadronic activity in the central rapidity region allowing the use of powerful jet vetoes.

Discovery Potential

The discovery potential of these channels is determined by their expected significance. This is equal to the expected number of signal events divided by the square root of the expected number of background events, both determined by Monte Carlo simulation. Figure 2.6 shows the contribution from each of these channels for a Higgs

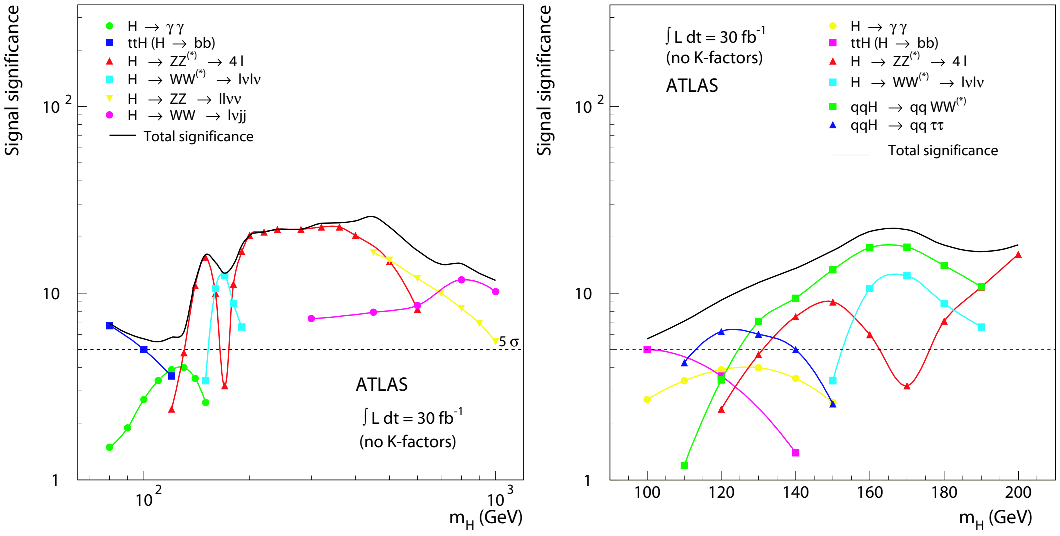

Figure 2.6: ATLAS sensitivity for the discovery of the Standard Model Higgs boson. The statistical significances are plotted for individual channels, as well as for the combination of all channels, assuming an integrated luminosity of $30\mathrm{fb}^{-1}$. The left hand plot is from the Physics TDR [20] and the right hand plot displays updated results for the low mass region [22].

discovery in terms of their expected significance. From these plots it can be seen that the low mass region is the most challenging for the ATLAS experiment.

CHAPTER 3

The ATLAS Detector

3.1 Large Hadron Collider (LHC)

The Large Hadron Collider (LHC) is a new experimental facility currently being built at the European Organisation for Nuclear Research (CERN) near Geneva. The experiment will produce two counter-rotating proton beams with energy of 7TeV, colliding them at four points around its 27km circular tunnel. The high centre of mass energy produced during such collisions facilitates the production of heavy particles and the high luminosity expected at the LHC, a measure of the intensity of the beams, will enable a large number of interesting interactions to take place. This high energy, high luminosity environment will enable the exploration of a variety of important questions. These include the origin of mass, the predominance of matter over anti-matter and the relationship of matter to the forces that act on it. A comparison of the expected LHC start-up energy and luminosity with those of previous proton-(anti-) proton facilities is shown in figure 3.1.

The LHC utilises a number of pre-existing CERN facilities, including the 27km circular tunnel that was previously home to the Large Electron Positron collider (LEP) and the full range of CERN proton machines that will become its injector chain. The LHC consists of twin aperture superconducting magnets producing a magnetic field of 8.33T, to accelerate the proton beams from 450GeV to 7TeV. A

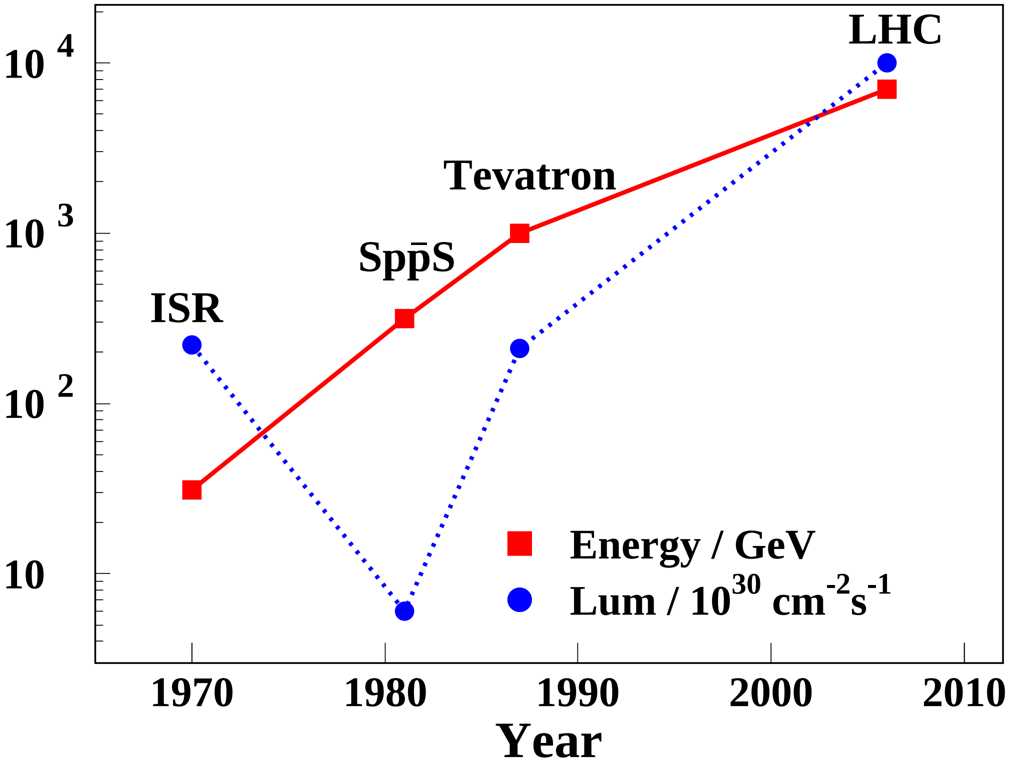

Figure 3.1: Energy and luminosity of various proton (anti-)proton experiments plotted against their start-up year.

cross-section of the LHC beam pipe is shown in figure 3.2 and a summary of the LHC beam parameters is given in table 3.1.

Four experiments will be located around the ring; ATLAS and CMS are multi-purpose detectors, ALICE is a heavy-ion detector designed to exploit the lead-lead runs of the LHC, and LHCb is an experiment to investigate CP violation in B^0_d and B^0_s systems. Figure 3.3 shows the layout of the experiments around the LHC ring.

The first collisions at the LHC are expected in December 2007. The current LHC schedule foresees a month of collisions at 900GeV, followed by a shutdown period between January and March. The first 14TeV collisions are expected around the end of June 2008, with the aim to collect a few fb^{-1} of data per experiment by the end of 2008.

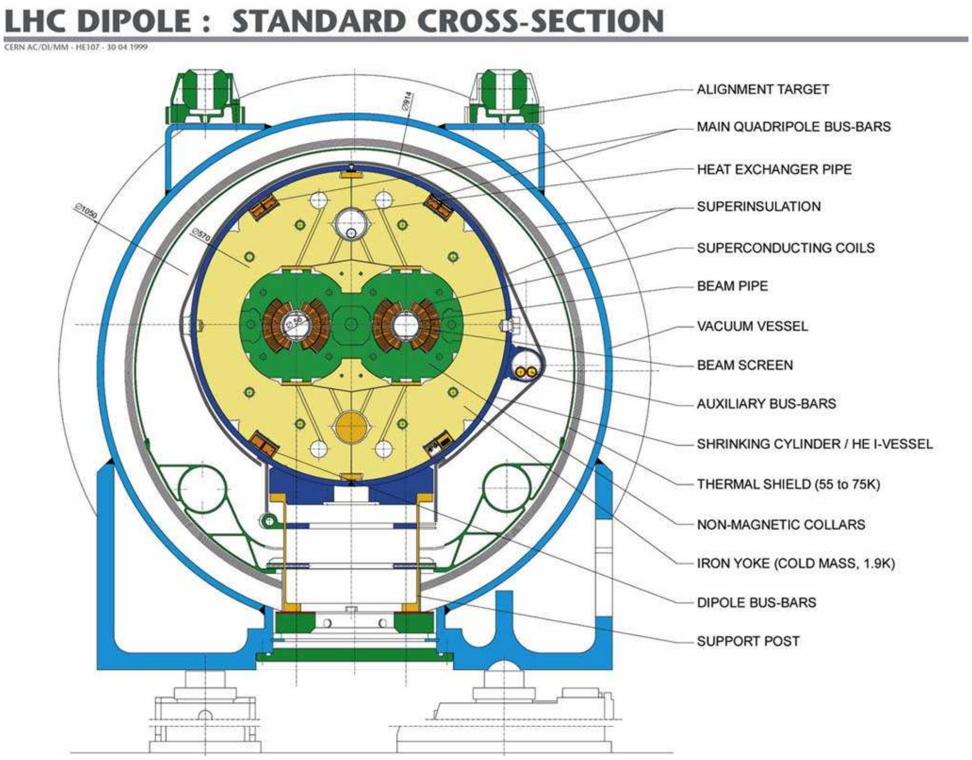

Figure 3.2: Cross section of the LHC dipole magnet [23].

3.2 Detector Concept and Terminology

The ATLAS [25, 26] detector, shown in figure 3.4, is the largest of the four LHC detectors with a total length of 42m, a radius of 11m and a weight of 7000 tonnes. It is a general purpose detector designed to fully exploit the discovery potential of the LHC. Its design is guided by the need to accommodate a large range of possible physics signatures, the major focus being sensitivity to a Higgs boson over the full range of allowed masses. The Higgs signatures alone require high resolution measurements of electrons, photons and muons; high resolution calorimetry for jets and missing transverse energy ($\not{E}_{\mathrm{T}}$); and excellent secondary vertex reconstruction for τ-leptons and b-quarks. Other signatures steering the design include particles predicted by supersymmetry and technicolor theories, new gauge bosons, the investigation of CP violation in B decays and precision measurements of the W and top-quark masses. These have additional requirements including charge identifica-

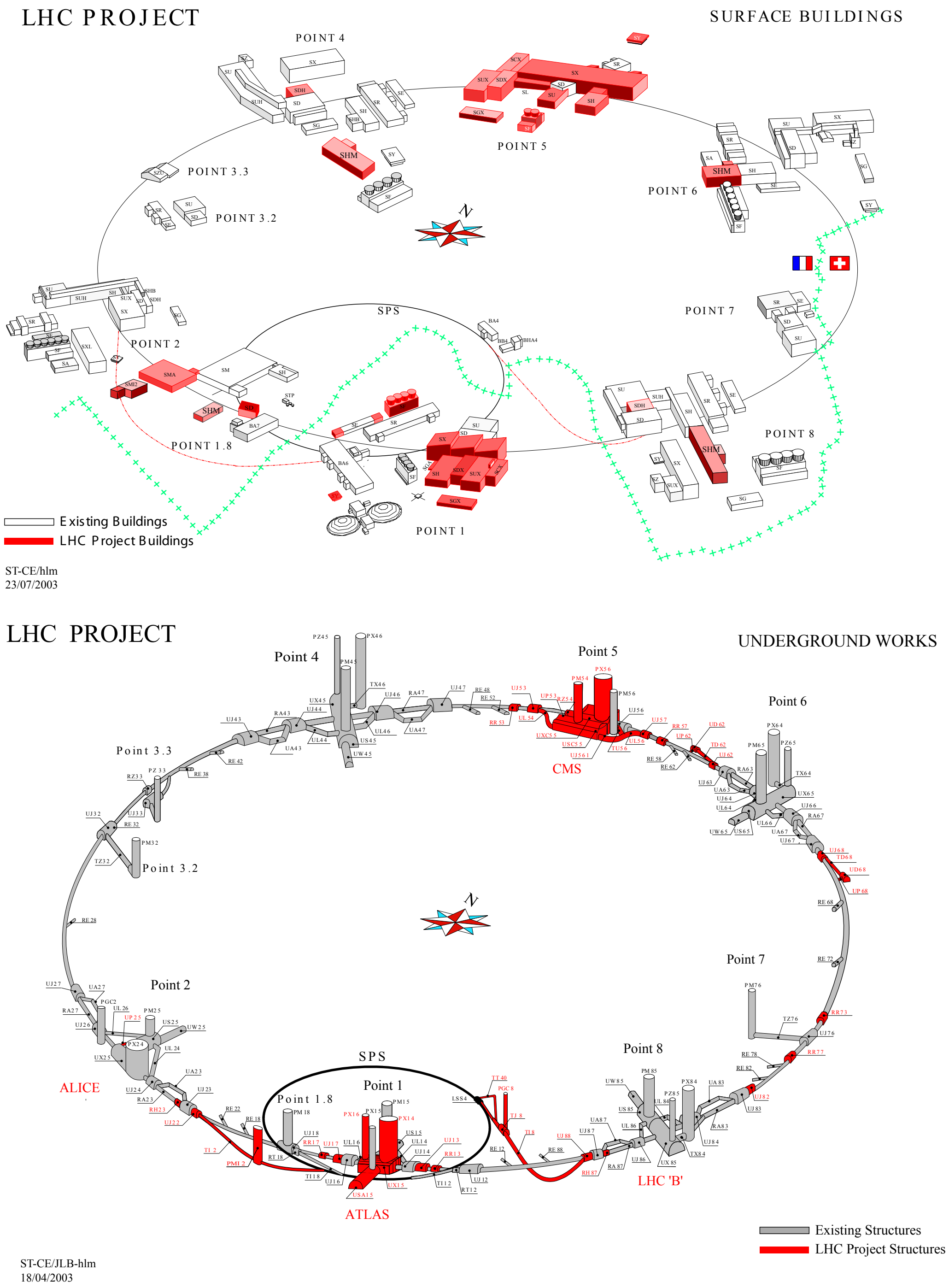
LHC PROJECT SURFACE BUILDINGS

ST-CE/hlm
23/07/2003

LHC PROJECT UNDERGROUND WORKS

ST-CE/JLB-hlm
18/04/2003

Figure 3.3: The LHC experimental facilities above and below ground [23].

Beam energy	7.0TeV
Time between collisions	24.95ns
Initial luminosity (Low)	2x$10^{33} cm^{-2} s^{-1}$
Luminosity (High)	$10^{34} cm^{-2} s^{-1}$
Luminosity lifetime	10hours
Particles per bunch	10^{11}
Bunch length (σ_z)	7.5cm
Bunch width (σ_x)	15.9 μm
Bunches per beam	2835
Beam current	0.53A
Magnetic field strength	8.33T
Dipole magnet temperature	1.9K

Table 3.1: Summary of LHC beam parameters.

tion up to a few TeV, b-tagging at high luminosity, the ability to fully reconstruct final states with low-$\mathrm{p_T}$ particles and the ability to trigger on low-$\mathrm{p_T}$ leptons.

The detector has an approximate cylindrical geometry, most frequently described using the coordinates (r, ϕ, z). The z-axis is defined along the beam direction. The azimuthal angle ϕ is measured around the beam axis and defined such that the positive x-axis points from the interaction point toward the centre of the LHC ring.

The 3-momentum of a highly relativistic particle is often described by three parameters: $\mathrm{p_T}(=\sqrt{p_x^2+p_y^2})$, ϕ and pseudorapidity η. The rapidity $y = \ln[(E+p_z)/(E-p_z)]$ of a Lorentz vector is defined such that rapidity differences are conserved under a boost along the z-axis. Without knowledge of the particle's mass a good approximation for this quantity within the relativistic limit is $\eta = -\ln(\tan\theta/2)$, where the polar angle θ is the angle between the beam direction and the direction of the particle. Cross-sections for inelastic proton-proton collisions are uniformly distributed in η.

For particles such as neutrinos that have an extremely small probability of interacting with the detector, it is possible to infer their presence by the apparent non-conservation of momentum of the observed particles. Due to the incomplete coverage of the detector at the beam pipe this is done by vectorially adding all the transverse momenta to calculate the missing transverse momentum, $\not{p}_\mathrm{T}$.

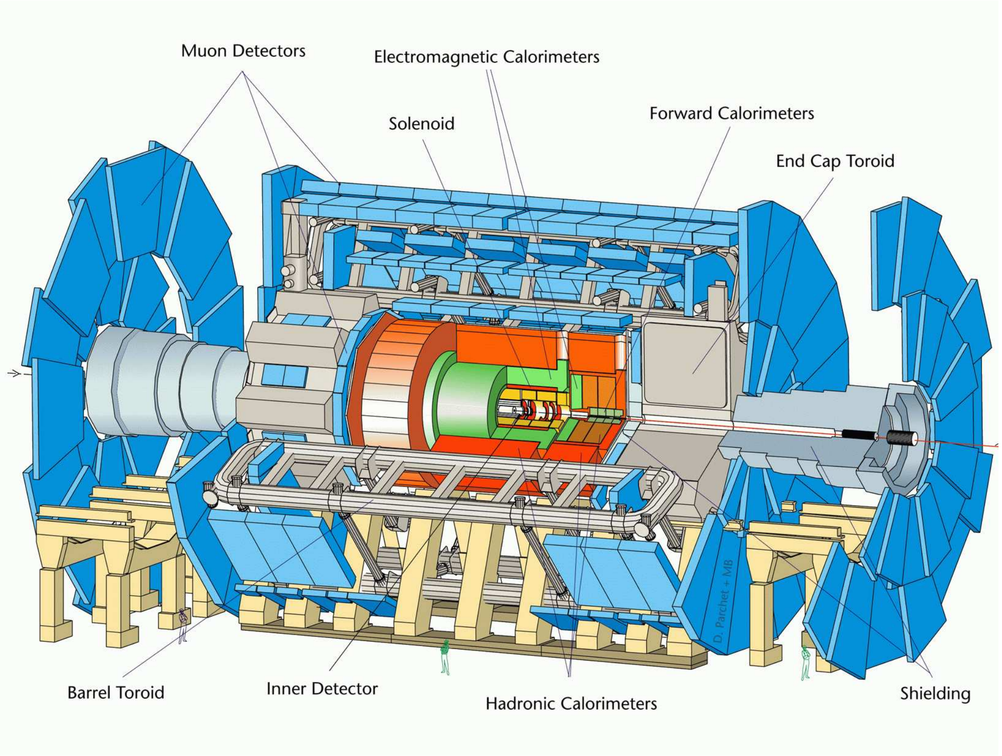

Figure 3.4: The overall layout of the ATLAS detector [24].

The ATLAS detector has three main components: the inner detector, the calorimeters and the muon spectrometer. Each of these are discussed in turn in the following sections.

3.3 Inner Detector

A cross-section of the inner detector is shown in figure 3.5. It consists of three distinct sub-systems, that on average, will record forty three position measurements for each charged particle between the beam pipe and the electromagnetic calorimeter. These position measurements can be reconstructed into tracks providing high precision momentum and charge information. Secondary vertex identification using the reconstructed tracks can be used to indicate the presence of short lived particles such as τ-leptons and b-quarks.

The inner detector design incorporates fine-resolution detectors at the inner most radii and continuous tracking elements at outer radii. Semi-conductor pixel detectors

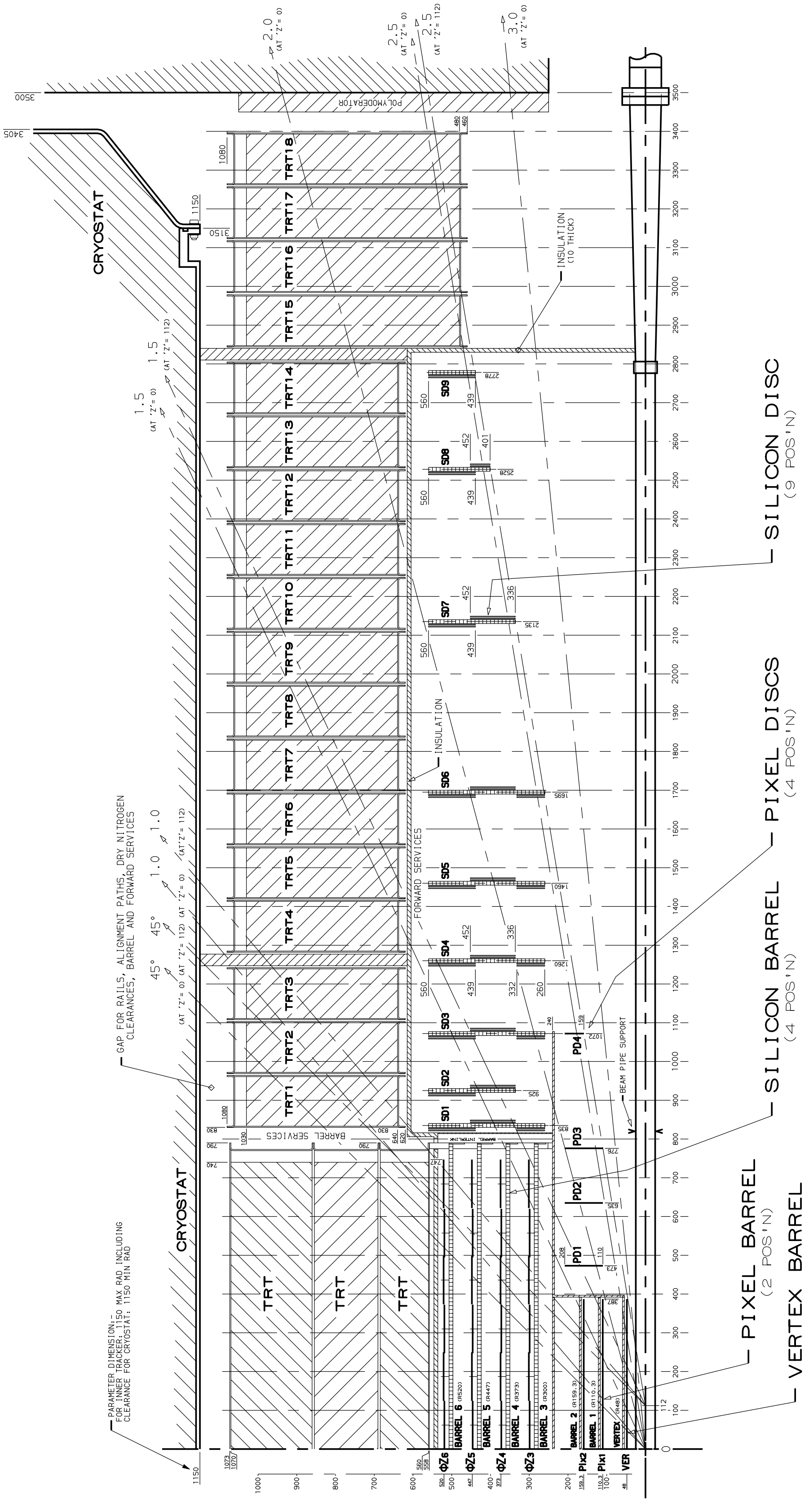

Figure 3.5: A cross-section of the inner detector engineering layout through the beam axis [27]. Units are given in centimetres.

provide the highest granularity as close to the beam pipe as possible, where the track density is greatest. The number of these precision layers is limited on account of the material and power dissipation that they introduce, as well as their high cost. Material between the interaction point and the calorimeter must be kept at a minimum to maximise the calorimeter performance. Decreased track density further from the beam pipe favours silicon microstrip detectors which have fewer read out channels and hence less material in the form of read-out systems. At outermost radii, straw tube technology provides continuous tracking with much less material per point at a much lower cost. The combination of silicon and straw tube technologies gives very robust pattern recognition and the relative precision of the measurements are well matched such that no one measurement dominates the momentum resolution.

The inner detector is 7m in length and 115cm in radius. It is contained within a 2T magnetic field, providing full tracking over a region of $|\eta|<2.5$. It is composed of three mechanically separate parts, a barrel section that occupies ±80cm along the z axis and two end-caps. In the barrel region, the high precision detectors are mounted on concentric layers around the beam axis. The end-cap detectors are mounted on disks perpendicular to the beam axis.

3.3.1 Pixel Detector

The pixel detector provides three precision measurements as close to the interaction point as possible. These measurements determine the impact parameter resolution and the ability of the inner detector to identify short lived particles.

Each pixel module is $62.4\times21.4\text{mm}^2$ in size and contains a reverse-biased silicon wafer as its active element. Silicon based detectors register the presence of a charged particle through the detection of electron-hole pairs produced when it traverses the material. Each wafer is segmented into 46,080 pixels, with a spatial resolution of 12μm in the $r-\phi$ direction and 60μm in z. The modules are mounted onto three barrels at average radii of ∼4cm, 11cm, 14cm and five disks in each end-cap between radii of 11cm and 20cm. In total there are 140 million readout channels in the pixel system.

The pixel detector will enable a large amount of interesting physics to be carried out in the B-sector at initial luminosity running and will provide good b-tagging performance for all phases of LHC. It is designed to withstand a large amount of ionising radiation, however it is expected that the innermost layer will have to be replaced every few years of high luminosity running.

3.3.2 Semi-Conductor Tracker (SCT)

The SCT system provides on average four precision measurements per track at intermediate radii. The SCT is comprised of $6.4\times6.4\text{cm}^2$ silicon wafers with 768 readout channels. Two wafers are bonded to produce 12.8cm long silicon detector strips and two pairs of these strips are glued back to back at a 40mrad angle to produce a module. These modules have a spatial resolution of 16μm in $r-\phi$, accurately measured from the hit strip, and 580μm in z, determined from the 40mrad angle between the front and back strips in the module. This design enables the SCT to have fewer read out channels and less material than the pixel detector but can still provide precise measurements, making it ideal for larger radii where the track density is lower. The modules are mounted on four barrel layers of radii 30cm, 37.3cm, 44.7cm and 52cm and nine end-cap wheels. In total, the SCT contains 61m^2 of silicon detectors.

3.3.3 Transition Radiation Tracker (TRT)

The TRT uses straw tube detectors to provide continuous tracking in the radial range 56cm to 107cm. Straw tube detectors are intrinsically radiation hard and can operate at very high rates due to their small diameter and the isolation of the sense wires within individual gas volumes.

The TRT contains 370,000 aluminium straws, each 4mm in diameter with a maximum length of 150cm. Each contains a gold-plated W-Re wire at the centre and is filled with a $Xe/CO_2/CF_4$ gas mixture. Each straw has a spatial resolution of 170μm obtained from drift-time measurements. When this is averaged over all straws, the TRT is accurate to 50μm.

The use of xenon gas provides electron identification through the detection of transition radiation photons that pass a higher threshold in the read out electronics than the charge liberated by a minimum ionising particle.

Transition radiation is emitted when particles traverse the boundary between media with different dielectric properties. The probability of a transition radiation photon being emitted at any particular boundary is small so the straws are surrounded by materials designed to contain many such transitions. One of its features is that the radiated energy increases with the Lorentz factor ($\gamma = E/m$) of the particle rather than the velocity. Particles with $\gamma >$1000 will produce high threshold hits with reasonable efficiency, providing a high electron identification efficiency with only a very small pion contamination.

3.4 Calorimeters

Tracking detectors are designed to measure position whilst minimising the effect this measurement has on the particle. In contrast, the principle of calorimetry is to measure the energy of the incident particle through total absorption, where a fraction of the total energy is transformed into a measurable quantity (charge or light). The intrinsic resolution improves with energy, making this type of detector extremely well suited to the LHC environment.

When a high energy electron or photon is incident upon matter it interacts predominantly through pair production ($\gamma \rightarrow e^+e^-$) and bremsstrahlung ($e \rightarrow e\gamma$) producing a cascade of secondary electrons and photons. As the shower develops the number of secondary particles increases and the average energy decreases. Such

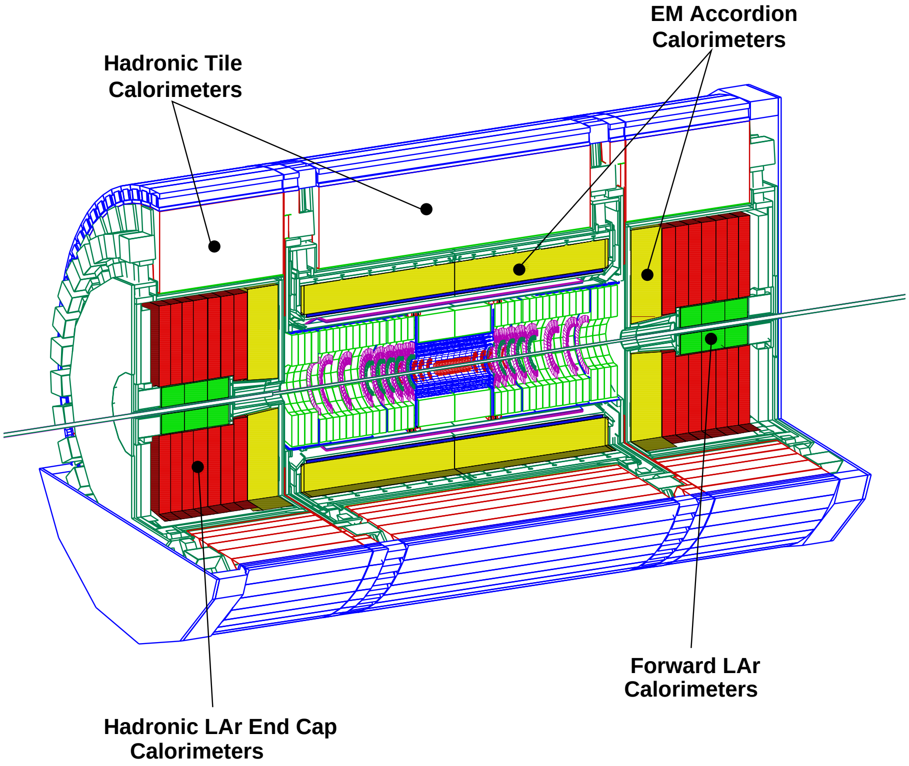

Figure 3.6: Three-dimensional cutaway view of the ATLAS calorimeters [24].

showers are characterised longitudinally by the radiation length (X_0) and have a narrow transverse profile.

High energy hadrons interact through a succession of inelastic hadron-nucleus collisions, resulting in the production of secondary hadrons (pions, kaons). Such showers have a larger lateral spread and a nuclear interaction length (λ) that is, depending on the material, an order of magnitude greater than X_0.

The ATLAS calorimeters, shown in figure 3.6, will provide energy measurements for electrons, photons and jets, as well as providing particle identification based on the shower shape and structure.

3.4.1 Electromagnetic Calorimetry

The electromagnetic calorimeter (ECAL) is a high granularity sampling calorimeter covering the region $|\eta|<2.5$. It is assembled from alternating layers of lead, to develop the shower, and liquid argon to detect the particles produced. These are arranged

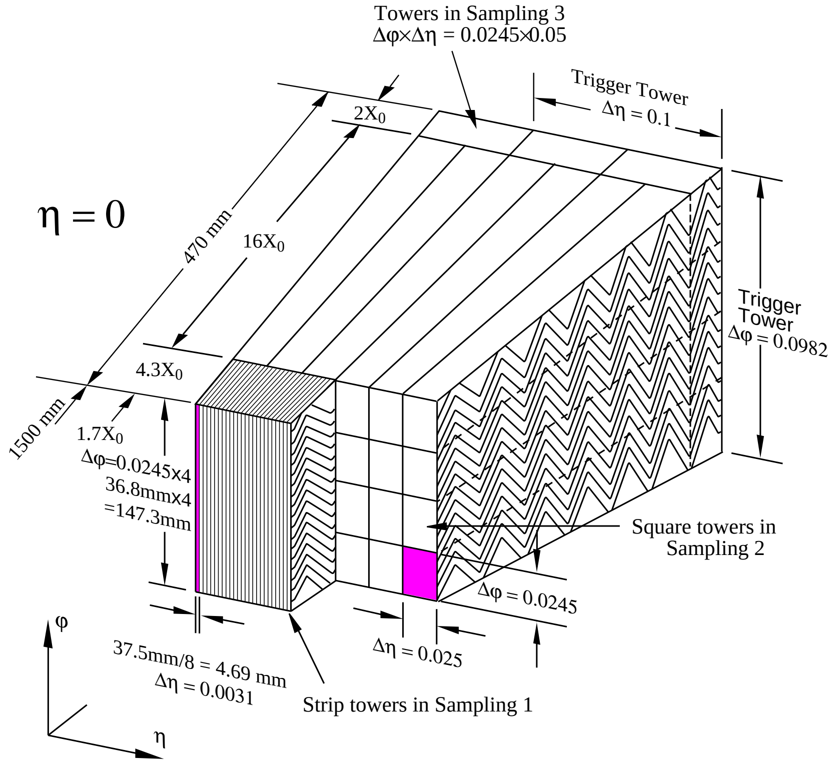

Figure 3.7: Sketch of the accordion structure of the ECAL [28]. The ‘pre-sampler’ is not shown in this figure.

in an accordion geometry (figure 3.7) providing continuous azimuthal coverage with minimal density variations.

Table 3.2 shows the segmentation in η and ϕ of the ECAL components. The first sampling is $6X_0$ in thickness and has a very high granularity in η (a pitch of approx 4mm). This sampling acts as a ‘pre-shower detector’, enhancing particle identification and providing a high precision η measurement. The second layer ($16X_0$) contains most of the shower, determining the particle energy and providing a second point for calculating particle direction. The back layer varies from $2X_0$ to $12X_0$ in length and is utilised for very energetic jets. Overall the ECAL has a thickness of at least $24X_0$ in the barrel and $26X_0$ in the end-caps.

In the region $|\eta|<1.88$ a 1cm thick LAr active layer, known as the ‘pre-sampler’, is present to correct for losses due to the $2X_0$ of material upstream of the calorimeter (inner detector, solenoid, cryostat). The design goal for the energy resolution of the

EM Calorimeter	**Barrel**	**End-cap**	
Coverage	$\|\eta\|<1.475$	$1.375<\|\eta\|<3.2$	
Longitudinal segmentation	3 samplings	3 samplings	$1.5<\|\eta\|<2.5$
		2 samplings	$1.375<\|\eta\|<1.5$
			$2.5<\|\eta\|<3.2$
Granularity ($\Delta\eta\times\Delta\phi$)			
Sampling 1	0.003×0.1	0.025×0.1	$1.375<\|\eta\|<1.5$
		0.003×0.1	$1.5<\|\eta\|<1.8$
		0.004×0.1	$1.8<\|\eta\|<2.0$
		0.006×0.1	$2.0<\|\eta\|<2.5$
		0.100×0.1	$2.5<\|\eta\|<3.2$
Sampling 2	0.025×0.025	0.025×0.025	$1.375<\|\eta\|<2.5$
		0.1×0.1	$2.5<\|\eta\|<3.2$
Sampling 3	0.050×0.025	0.050×0.025	$1.5<\|\eta\|<2.5$

Table 3.2: Pseudorapidity coverage, granularity and longitudinal segmentation of the ATLAS electromagnetic calorimeters.

electromagnetic calorimeter is

$$\frac{\sigma_E}{E} = \frac{0.1}{\sqrt{E(\mathrm{GeV})}} \oplus \frac{0.3}{E(\mathrm{GeV})} \oplus 0.01.$$

The first term in the equation is the sampling term and is due to fluctuations in the electromagnetic shower. The second term is due to pile-up and electronic noise. The third term is due to non-uniformity of the calorimeter such as leaks and dead material.

3.4.2 Hadronic Calorimetry

The hadronic calorimeter uses three different techniques to cover a large η range that has varying requirements and radiation environments. In the barrel and extended barrel regions, where $|\eta|<1.7$, the hadronic calorimeter consists of alternating iron plates and plastic scintillator tiles (this is known as the TILE calorimeter). The tiles are oriented perpendicular to the beam pipe and grouped into cells at approximately constant η by combining signals from different wavelength-shifting fibres into a single photomultiplier. The barrel and extended barrel consist of three samplings, the first two with a granularity in $\Delta\eta\times\Delta\phi$ of 0.1×0.1 and the third with 0.2×0.1.

Over the range 1.5<$|\eta|$<4.9, LAr is used as the detecting medium due to the high radiation levels. Between 1.5<$|\eta|$<3.2, a copper/LAr sampling calorimeter is used with a granularity in $\Delta\eta\times\Delta\phi$= 0.1×0.1 (0.2×0.2) up to $|\eta|$=2.5(3.2). In the very forward region, 3.2<$|\eta|$<4.9, a dense Cu/W LAr calorimeter measures both hadronic and EM showers, fulfilling missing transverse momentum and forward jet detection requirements.

The hadronic calorimeters have a total thickness of eleven interaction lengths (λ) at η=0. The design goal for the energy resolution is

$$\frac{\sigma_E}{E} = \frac{0.5}{\sqrt{E(\mathrm{GeV})}} \oplus 0.03.$$

3.5 Muon Spectrometer

With no strong interactions and a relatively large mass, muons lose energy primarily by ionisation. This allows them to pass through the calorimeters with minimal energy loss to dedicated detectors for identification and momentum measurement.

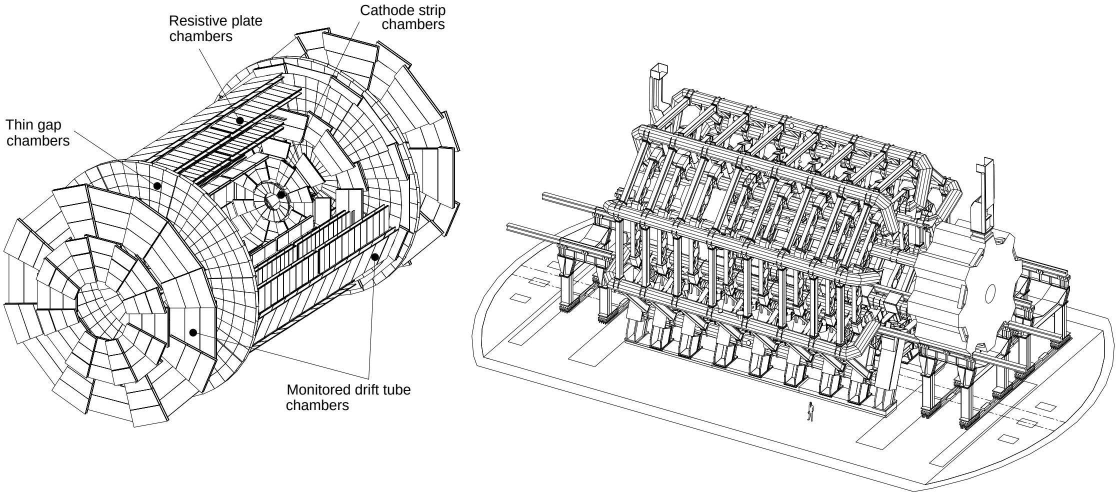

(a) (b)

Figure 3.8: Three-dimensional view of (a) the muon spectrometer instrumentation indicating the areas covered by the four different chamber technologies [24] and (b) the muon magnets [29].

The design of the muon spectrometer, shown in figure 3.8, is based on the magnetic deflection of muons in a system of three large superconducting air-core toroid magnets, instrumented with separate trigger and high precision tracking chambers. For good momentum resolution at high energies a large magnetic field over long distances is desirable, giving rise to the large scale of the muon system: 20m in diameter, 26m in length with an average magnetic field of 0.6T. The toroidal geometry produces a field that is mostly orthogonal to the muon trajectories.

The precision chambers are mounted on three cylindrical layers, known as stations, around the beam axis in the barrel at radii of 4m, 7.5m and 10m. In the end-caps, chambers are installed vertically on three disks/stations at 7m, 10m and 14m from the interaction point. Monitored Drift Tubes (MDTs) are used over most of the η range, with higher granularity Cathode Strip Chambers (CSCs) used closer to the beam line (over the range $2<|\eta|<2.7$) to withstand the demanding rate and background conditions. The chambers are arranged such that particles from the interaction point traverse three of the stations. In the barrel, chambers are arranged in projective towers with particles measured in 2×4 sensitive layers in the inner station and in 2×3 layers in the middle and outer stations.

The trigger system covers the pseudorapidity range $|\eta|<2.4$. Resistive Plate Chambers (RPCs) are used in the barrel and Thin Gap Chambers (TGCs) in the end-cap region. The trigger chambers: have excellent time resolution enabling them to identify the bunch crossing; provide triggering with well defined p_{T} cut-offs in a moderate magnetic field; and also provide a “second-coordinate” measurement in a direction approximately parallel to the magnetic field lines, complementing the measurements made by the precision chambers.

An overview of the muon chamber instrumentation is given in table 3.3.

3.6 Trigger

The total proton-proton inelastic cross-section at the LHC is estimated to be 80mb. In comparison, the production rate for a Standard Model Higgs boson with mass 120GeV is approximately 20pb. The ATLAS trigger has the task of reducing the

	Precision chambers		Trigger chambers	
	CSC	MDT	RPC	TGC
Number of chambers	32	1194	596	192
Number of readout channels	67,000	370,000	355,000	440,000
Area covered (m^2)	27	5500	3650	2900

Table 3.3: Summary of the number of chambers, the area covered, and the number of readout channels for the four muon chamber technologies.

LHC interaction rate of 40MHz to approximately 200Hz for storage, a limit set by restrictions in offline computing power and storage capabilities. The selection strategy has to ensure that rare signals will not be missed whilst providing an efficient rejection of high rate backgrounds, with the added complication that there are expected to be around twenty three interactions per bunch crossing at design luminosity.

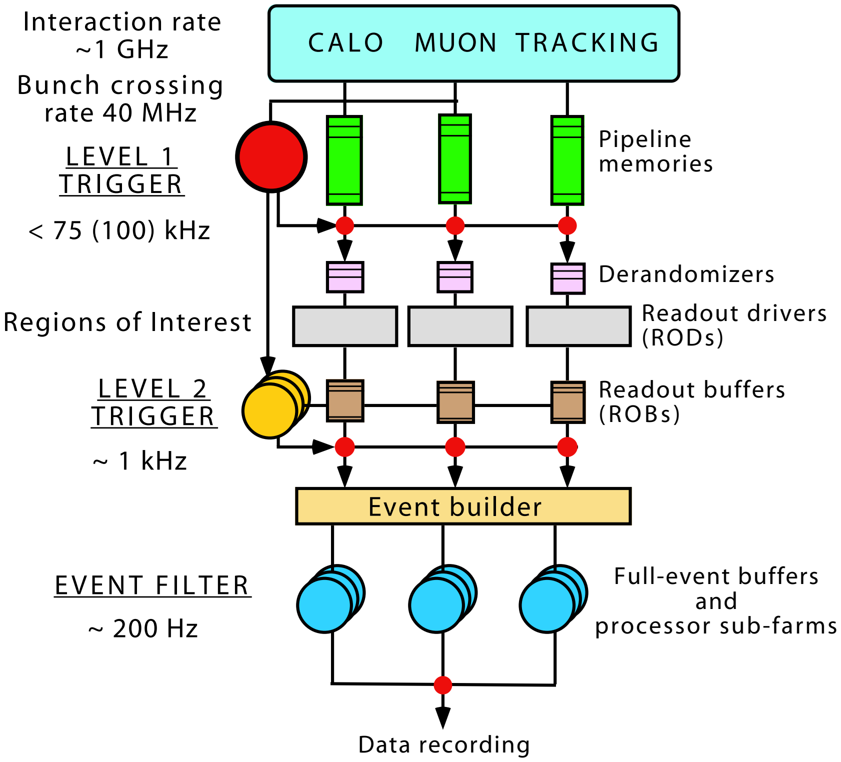

Figure 3.9: Block diagram of the Trigger/DAQ system [24].

The ATLAS trigger and data acquisition system [30, 31] is based on three levels of online event selection, shown in figure 3.9. Each trigger level refines the decisions made at the previous level and applies additional selection criteria.

The first level (LVL1) trigger makes an initial selection using information from the muon trigger chambers and reduced granularity data from each of the calorimeter systems. The calorimeter front end electronics read out data in towers of 0.1×0.1 in η and ϕ and run basic algorithms to search for localised energy deposits that might be due to electrons, photons, τ-leptons or hadrons using a number of threshold, isolation and veto cuts. For example, the electron/photon trigger uses a combination of thresholds for the cluster $\mathrm{E_T}$, isolation thresholds on the surrounding $\mathrm{E_T}$ in the electromagnetic calorimeter and veto thresholds on the associated hadronic towers. A calculation of $\not{E}_\mathrm{T}$ and the total scalar $\mathrm{E_T}$ are also performed. High transverse momentum muons are identified in the muon system and the overall LVL1 decision is based on a combination of objects in coincidence or veto. The LVL1 decision has to be made within 2μs.

At the second level trigger (LVL2) full granularity, full precision data are available from all the detectors, but only in Regions of Interest (RoI) identified by LVL1. Using this mechanism, only a few percent of the full event data needs to be accessed. LVL2 provides fast track reconstruction utilising information from the inner detector and muon systems. LVL2 also makes use of isolation in the muon system and more accurate $\mathrm{p_T}$ measurements, allowing tighter cuts to be made. LVL2 runs on a dedicated CPU farm with the aim to reduce the event rate to about 1kHz with an average execution time per event of 10ms.

At the third level, the Event Filter has access to the full event data as well as calibration and alignment information. This is used to make the final decision before the event is recorded with a target average execution time of 1s. Events are accepted if they satisfy at least one of the physics signatures given in a trigger menu. Table 3.4 contains examples of various selection criteria and the physics processes they cover.

Selection Signature	Examples of physics coverage
e25i	$W \rightarrow l\nu, Z \rightarrow ll$,top production,$H \rightarrow WW^{(*)}/ZZ^{(*)}, W^{'}, z^{'}$
2e15i	$Z \rightarrow ll, H \rightarrow WW^{(*)}/ZZ^{(*)}$
μ20i	$W \rightarrow l\nu, Z \rightarrow ll$,top production, $H \rightarrow WW^{(*)}/ZZ^{(*)}, W^{'}, z^{'}$
2μ10	$Z \rightarrow ll, H \rightarrow WW^{(*)}/ZZ^{(*)}$
γ60i	direct photon production, $H \rightarrow \gamma\gamma$
2γ20i	$H \rightarrow \gamma\gamma$
j400	QCD, SUSY, new resonances
2j350	QCD, SUSY, new resonances
3j165	QCD, SUSY
4j110	QCD, SUSY
τ60	charged Higgs
μ10+e15i	$H \rightarrow WW^{(*)}/ZZ^{(*)}, SUSY$
τ35+xE45	$qqH(\tau\tau), W \rightarrow \tau v, Z \rightarrow \tau\tau$,SUSY at large tan β
j70+xE70	SUSY
xE200	new phenomena
E1000	new phenomena
jE1000	new phenomena
$2\mu6 + \mu^{+}\mu^{-}$+mass cuts	rare B-decays (B $\rightarrow \mu\mu$X) and B $\rightarrow J/\psi(\psi^{'})$X

Table 3.4: Trigger menu, showing inclusive physics triggers. Labels of the form 'NoXXi', N is the minimum number of objects required, o indicates the type of selection (e=electron, γ=photon, μ=muon, τ=τ-hadron, j=jet, b=b-tagged jet, xE=$\not{E}_{\mathrm{T}}$, E=total energy, jE=total $\mathrm{E_T}$ obtained using only jets), XX is the $\mathrm{E_T}$ threshold and i indicates the isolation requirement. The relevant triggers for the analysis presented in this thesis are e25i and μ20i.

Chapter 4

The Atlantis Event Display

4.1 Introduction

Atlantis is an event display for the ATLAS experiment and is based on the ALEPH event display DALI [32, 33]. The primary goal of the program is to provide easy, fast, error-free visual investigation and physical understanding of the complicated events recorded by ATLAS. As events and detectors increase in complexity, conventional 3D Cartesian views of events are becoming less optimal. Atlantis displays event data using a collection of 2D/3D data orientated projections that proved to be extremely effective at ALEPH.

This chapter provides an overview of the Atlantis package, starting with an introduction to its features and the data orientated projections it displays. This is followed by a look at the program design and implementation, detailing specific areas of development carried out as part of this doctorate. Just over one year was spent working on the Atlantis project. During this time my responsibilities included: adding the ability to display several new data types; improving event access mechanisms; adapting for major changes in the event data model within the ATLAS computing framework; producing documentation and jointly organising and presenting two tutorials on the use of the display.

Atlantis was used during the 2004 tests of detector components both as a tool to aid debugging of reconstruction software and also as an 'online' event display, receiving and displaying data when read and reconstructed from the detector electronics. The final section of this chapter describes the features implemented in Atlantis to carry out these tasks. This was my main area of development during the year working on the project. The work to adapt the display for the test beam geometry was carried out in collaboration with other developers working on the Atlantis project.

4.2 Program Overview

Atlantis is a Java application with a mouse driven user interface. The main canvas area, where the projections are drawn, can display multiple views of the data with varying size and position. The user can interact with the views using mouse based interactions such as zoom, selection and query. A fish-eye transformation is also provided. This is a radially dependant zoom that enables detailed views of the inner detector to be shown on the same image as the muon system.

Associations between data objects, as well as the values of their member variables, provide criteria upon which the Atlantis user may filter a full ATLAS event. By choosing whether or not to show certain data, and if so in what colour, a more personalised and useful display may be obtained. Also, the user can dynamically create and manage their own associations and perform context dependent operations upon them.

Atlantis displays an idealised detector geometry. The purpose of this is to rapidly convey the context in which hits are to be viewed rather than to display a detailed image of the detector. Event data are read in from Extensible Markup Language (XML) files produced by a dedicated algorithm running in the ATLAS software framework, ATHENA [34].

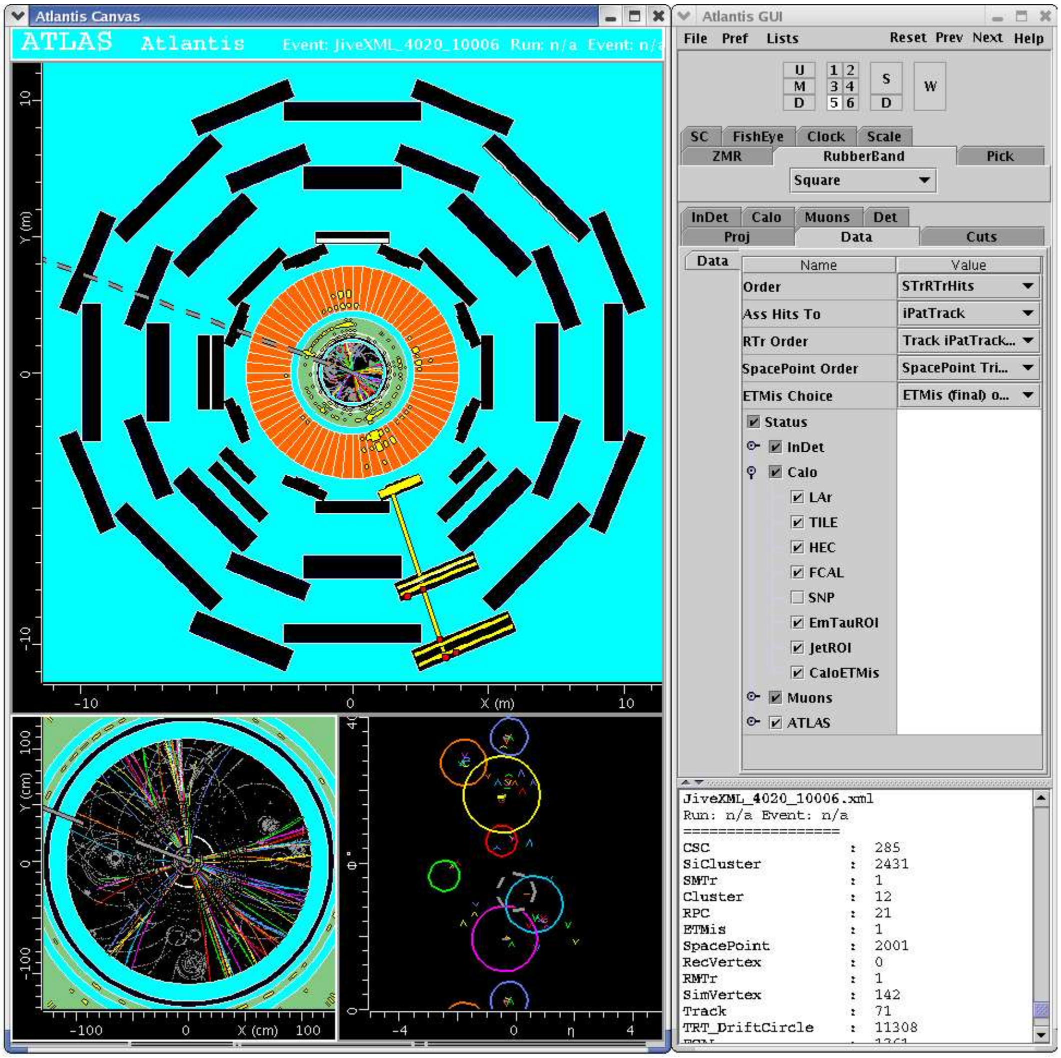

Name	Value
Order	STrRTrHits
Ass Hits To	iPatTrack
RTr Order	Track iPatTrack...
SpacePoint Order	SpacePoint Tri...
ETMis Choice	ETMis (final) o...

- ☑ Status
- ☑ InDet
- ☑ Calo
  - ☑ LAr
  - ☑ TILE
  - ☑ HEC
  - ☑ FCAL
  - ☐ SNP
  - ☑ EmTauROI
  - ☑ JetROI
  - ☑ CaloETMis
- ☑ Muons
- ☑ ATLAS

```
JiveXML_4020_10006.xml
Run: n/a Event: n/a
==================
CSC                    :  285
SiCluster              :  2431
SMTr                   :  1
Cluster                :  12
RPC                    :  21
ETMis                  :  1
SpacePoint             :  2001
RecVertex              :  0
RMTr                   :  1
SimVertex              :  142
Track                  :  71
TRT_DriftCircle        :  11308
```

Figure 4.1: Screen shot of the Atlantis event display, showing the main canvas on the left and the user interface on the right.

4.2.1 Data Orientated Projections

The projections incorporated into Atlantis include the intuitive Y/X, Y'/Z, X'/Z, ρ/Z projections[1] as well as the more powerful but less intuitive ϕ/ρ, ϕ/Z projections and the V-Plot (3D).

Y/X The Y/X projection is an easily understandable projection looking along the beam line. This projection is useful to view tracks and hits in the inner silicon detectors, providing an estimation of charge and $\mathrm{p_T}$, and to associate

---

[1] The primed coordinates are modified to take into account the primary vertex of the event, for example X'=X-X_{vertex}.

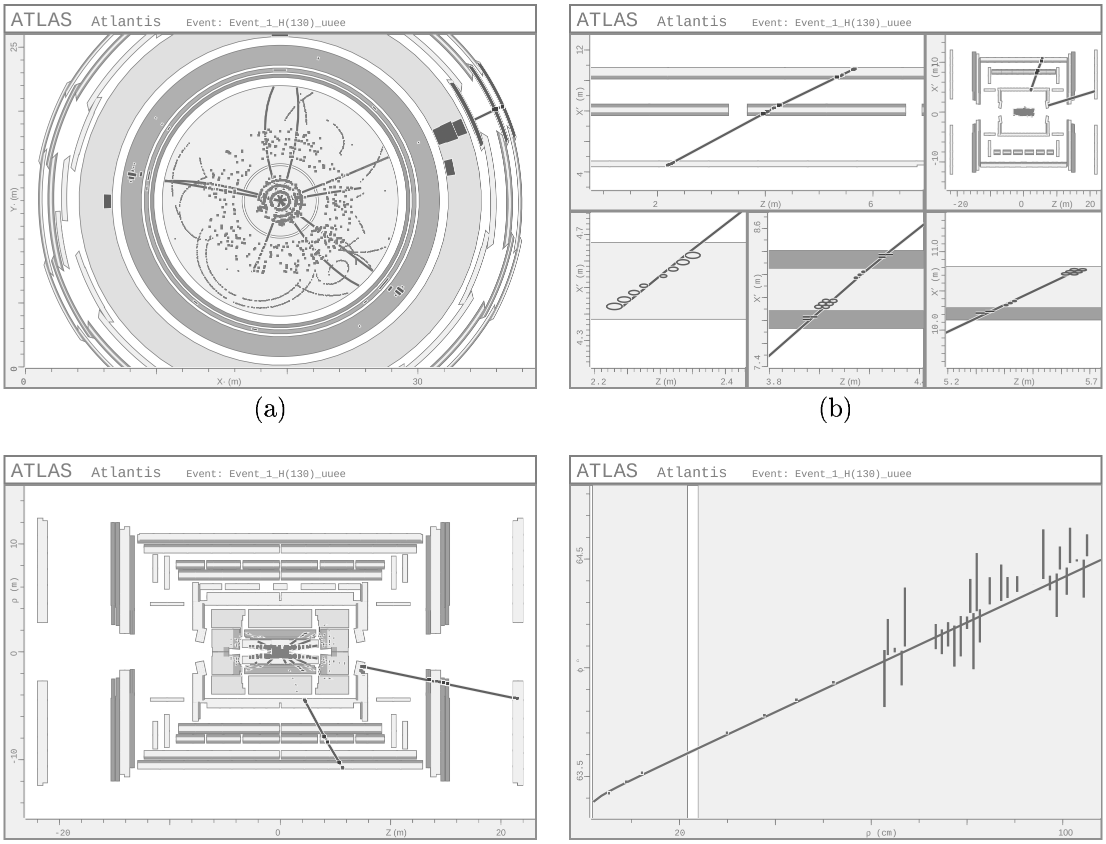

(a) (b)

(c) (d)

Figure 4.2: (a) The Y/X projection with fish-eye applied. (b) The X'/Z projection showing a single muon sector (top right), a zoomed view into the upper most muon track (top left) and a zoomed view for each muon MDT layer (bottom). (c) The ρ/Z projection. (d) The ϕ/ρ projection showing a track in the inner detector.

them with the TRT, LAr and TILE barrels. This projection is also useful to look at the Muon RPC ϕ-strips. End-cap information is not displayed for the calorimeters and muon system as these would fall on top of the tracking and calorimeter barrel data, complicating the picture. Separate views in this projection are available for the muon end-caps and forward calorimeters (FCAL). Figure 4.2a is the Y/X projection with a fish-eye transformation applied.

X'/Z The X'/Z projection is a useful view for the muon system and vertex region. The eight muon sectors, both barrel and end-cap, can be viewed individually. This enables comparisons between the reconstructed muon tracks and hits in the Monitored Drift Tubes (MDTs), seen as circles in this view (figure 4.2b).

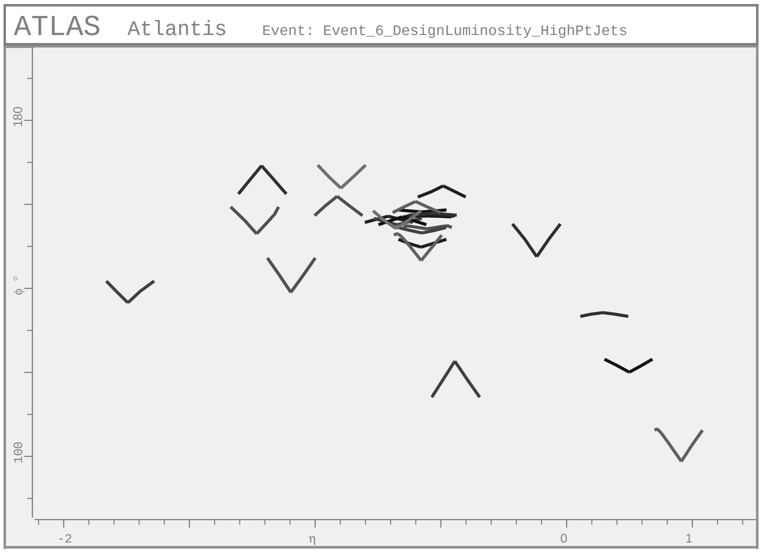

Figure 4.3: The V-Plot showing tracks reconstructed in the inner detector.

ρ/Z The ρ/Z projection is the only projection where all the main detector units can be displayed without overlapping (figure 4.2c). It enables the user to associate inner detector hits and tracks with the full calorimeter system. It provides a rough association to muon data from all sectors superimposed. This is a non-linear projection but is intuitively understandable, with tracks from the origin taking the form of approximately straight lines.

ϕ/ρ The ϕ/ρ projection can be regarded as a modified Y/X projection, with the same data being displayed in both. This is not an intuitive projection but allows a better angular separation of data from the innermost detectors. Pattern recognition is easier in this projection (figure 4.2d) as helices are approximately straight lines. Tracks not pointing to the origin are distinctly non-linear when approaching ρ=0 and both the particle's charge and $\mathrm{p_T}$ can be estimated from the track slope.

The V-Plot (figure 4.3) is an extremely useful and powerful projection. It is a modified form of the ϕ/η projection. ϕ/η provides optimal separation of tracks but does not provide charge, $\mathrm{p_T}$ estimation or ρ information for hits. The V-Plot provides a solution to this by drawing two points (ϕ,η_1),(ϕ,η_2) for each single point on the ϕ/η plot using the equation $\eta_1, \eta_2 = \eta \pm k \times (\rho_{max} - \rho)$, where ρ_{max} is normally the outer SCT radius and k can be set by the user. ϕ, η, ρ may be recalculated from each pair of points, making this a 3D projection. The following rules apply to interpret the V-Plot:

- Helices transform into a V-like pattern.
- For helices pointing to the origin with not too low p_T the arms of the V's are straight.
- For helices not pointing to the origin the arms of the V's are curved:
  - with the same sign of curvature for tracks separated from the origin in z,
  - with the opposite sign of curvature for tracks separated from the origin in ρ.
- Positive tracks give V's pointing downward.
- Negative tracks give V's pointing upward.
- The gradient of a V is proportional to $1/p_T$:
  - high p_T tracks give V's with a small opening angle,
  - low p_T tracks give V's with a large opening angle.

4.2.2 Advanced Features

Other features provided by Atlantis include a filtering algorithm, designed to remove inner detector space points that are not consistent with tracks originating from a given primary vertex position (figure 4.4a). The filtering algorithm is based on the fact that all the hits from a track with sufficiently high p_T are contained in a small solid angle in (ϕ,η) that starts from the track's initial z position, in contrast to hits from tracks originating from different z positions. If enough hits are contained

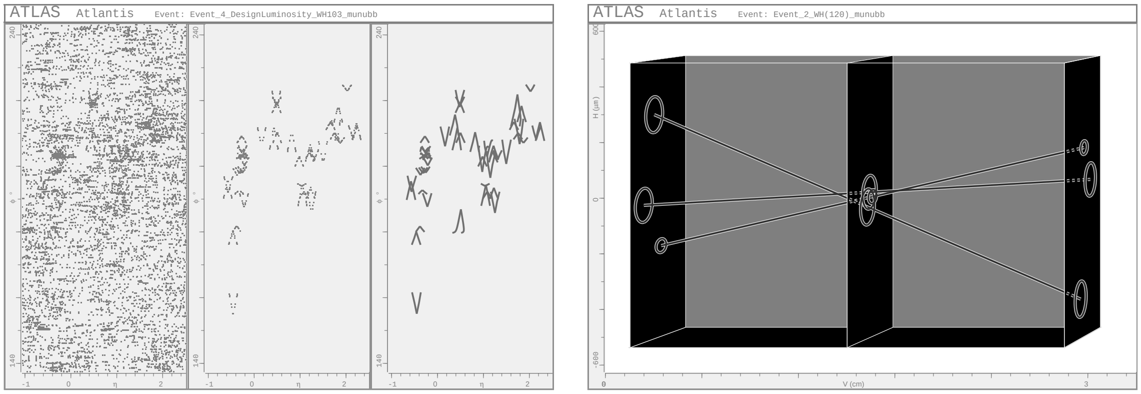

(a) (b)

Figure 4.4: (a) V-Plot projection of a high luminosity event before (left) and after (middle) filtering. Reconstructed tracks for comparison (right). (b) The 3D Box projection.

in a (ϕ,η) bin then they are accepted by the filter. This algorithm is extremely efficient and is now the basis of a fast tracking algorithm for the ATLAS Second Level Trigger [35]. Atlantis also provides the ability to investigate a small 3D region around a newly formed secondary vertex (figure 4.4b). The user can zoom and rotate the area contained by the box to check the validity of the vertex.

4.3 Design and Implementation

Atlantis has six main components: the event manager; the detector system; the Graphical User Interface (GUI); the projection manager; the canvas and the parameter store. Figure 4.5 is a simplified class diagram depicting these components.

Event manager The role of the event manager is to control the process of reading in event data and to provide access to the current event. An event is a collection of data entities. Each entity represents either the information from a single ATLAS sub-detector or a reconstructed data type, such as a particle track.

Detector system The detector system controls all aspects of rendering the idealised detector geometry to the screen.

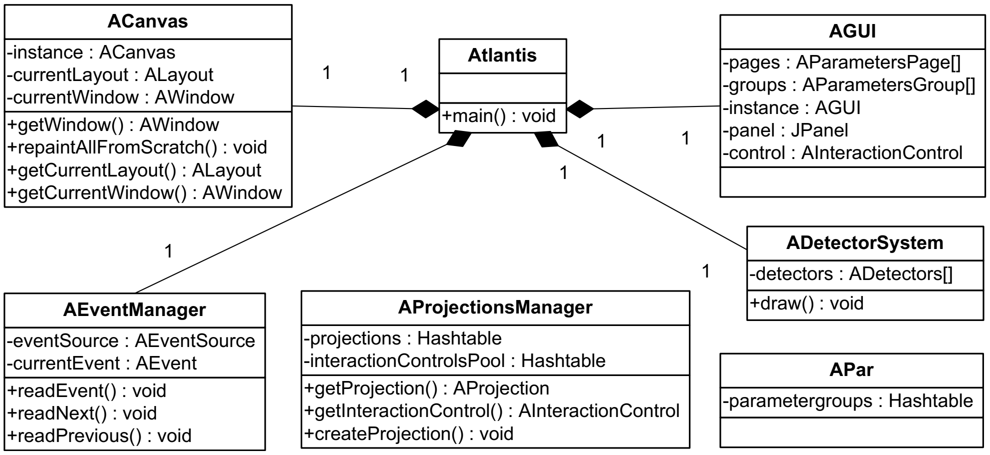

Figure 4.5: A UML diagram showing the six main components of Atlantis.

Parameter store The parameter store holds all variables that can be altered in the creation of a display. These include, amongst others, the status of data types, cuts applied to data as well as the colour of hits, particles and detector components.

Projection manager The projection manager controls the collections of projections and interactions that can be selected by the user.

Canvas The canvas is the screen area where images are drawn. It manages the placement and size of displays within its boundaries.

Graphical User Interface The GUI provides the user with the ability to interact with Atlantis. It provides the mechanisms to: alter parameters in the parameter store, select the current projection and interaction in a certain window, choose the windows that are displayed and where to display them, and control the reading in of events and writing out of images.

Each of these components will be explained in more detail in the following sections.

4.3.1 XML

Atlantis uses XML to obtain event data, detector geometry information, the content of the GUI and information about the various projections, interactions and window layouts. XML is a text based markup language where data are identified using tags. Atlantis uses two Application Programming Interfaces (APIs) for accessing XML documents, SAX and DOM. Atlantis event XML files are read in using the Simple API for XML (SAX). This is an event driven API that reports parsing events to the application through callbacks whenever it sees a tag. The application implements handlers to process different parsing events, which create an event object model in memory. The other type of XML API is the Document Object Model (DOM). This is a tree based model that maps an XML document into an internal structure, thus enabling an application to navigate the document hierarchy. Using this mechanism it is possible to access any part of the data in any order. DOM is used by Atlantis to load the configuration file at initialisation and to read the detector geometry information. Although DOM is an easier API to use, it requires the entire XML structure to be parsed and the object tree to be held in memory, so is a lot more CPU and memory intensive than SAX.

Atlantis uses the Java API for XML Processing (JAXP), a common interface to various SAX and DOM parsers. The Xerces parser [36] is used in the current implementation.

4.3.2 Event Package

The event package contains many different data entities. These provide an object representation for each different type of reconstructed data from the ATLAS detector. Instances of these entities are accessed though the event manager and are stored in a collection that represents a full ATLAS event. Figure 4.6 depicts the data management classes and figure 4.7 the data type hierarchy.

AEventManager

The `AEventManager` is created when the program is started and is implemented as a singleton. This class controls the reading in of events and access to the event data.

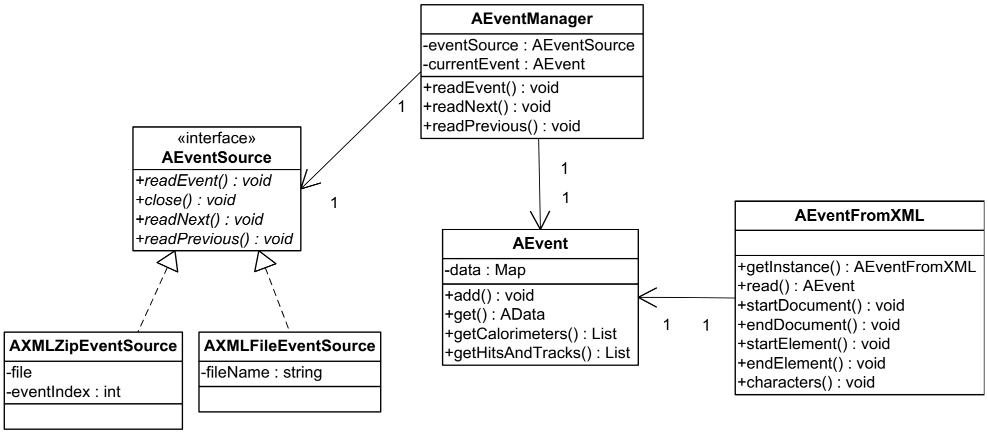

Figure 4.6: A class diagram showing the main components of the Event package.

When a new data file is loaded, the `readEvent(String sourceName)` method of this class is called. When event data are required by another part of the application, it is obtained using the `getCurrentEvent()` method, which returns an object of type `AEvent`.

AEventSource

When an event is requested the `AEventManager` creates an `AEventSource` object depending on the input type. The input type can be, for example, a local XML/zip file or one at a remote location. `AEventSource` is an interface with three methods: `readEvent()`, `readNext()` and `readPrevious()`. The latter two methods can be used to navigate between events from the same source, such as the next zip entry in a specified zip file. `AEventSource` obtains a `FileInputStream` reference to the data file and passes this to an instance of `AEventFromXML`. The data are parsed and the created `AEvent` returned to the `AEventManager`.

AEventFromXML

`AEventFromXML` is a singleton class that extends the `DefaultHandler` from the SAX API, overriding certain methods. When the event file is being read, the SAX parser calls methods implemented in the `DefaultHandler` in response to encountering certain tags. An example of the format of an event XML file is given below:

```
<?xml version "1.0"?>                                          1
<?ATLAS Release:  "6.0.3"?>                                    2
<!DOCTYPE Event SYSTEM "event.dtd">                            3
<Event version = "6.0.3">                                      4
   <TRT Count = "3">                                           5
      <barcode> 100607 100607 100607 </barcode>                6
      <driftR> 0.171858 0.109730 0.074016 </driftR>            7
      <id> 268468704 268468736 268468768 </id>                 8
      <phi> 0.323159 0.331340 0.339521 </phi>                  9
      <rhoz> -84.425011 -84.425011 -84.425011 </rhoz>         10
      <threshold> 0 0 0 <threshold>                           11
   </TRT>                                                     12
</Event>                                                      13
```

When reading the event from the XML file, the XML parser knows it is reading an element tag but does not know the role of that element within the document. Atlantis retains internal state information whilst processing callbacks.

The methods implemented by `AEventFromXML` include:

startElement This method is called when an opening tag is encountered. It is supplied with the name and any attributes of the tag by the parser. The action performed by this method depends on the current state. When `<Event>` in line 4 of the example is encountered, the state is simply changed to WAITING_DATA. On reaching the `<TRT>` tag in line 5, this method sets the state to WAITING_ARRAY and stores the name of the element and the count value in a map held by the class. At the beginning of line 6 `startElement` is called again, this time the type is requested (obtained from the Document Type

Definition (DTD) file) and an `AArrayParser` of this type is created and set to be the current `AArrayParser`. There are three types of `AArrayParser`: `AStringArrayParser`, `AFloatArrayParser` and `AIntArrayParser`. The size of the array is set from the count obtained in line 5.

endElement This method is called when a closing element is encountered. If the state is WAITING_ARRAY, the data contained in the `AArrayParser` are placed into the map held by the class. If the state is WAITING_DATA, an `AData` object is created from the data currently in the map and added to the `AEvent` being created.

characters This method is called for each chunk of character data the parser reads. The data between the element open and close tags ares split by the XML parser as it chooses. This method simply proxies the provided character array to the current array parser.

AEvent

`AEvent` is a container class for objects of type `AData`. The data objects are stored internally in a map. Methods are provided to return different subsets of the data, including data visible in the current projection and data objects of the same type, for example hadronic calorimeter data or hit and track data.

AData

Figure 4.7 shows the inheritance structure of the data entities. Each type encapsulates the information necessary to draw itself in each projection. They provide methods that return an `ACoord` object, containing the horizontal and vertical positions of the points to be drawn and the type of shape it should be. This is then passed to a 2D graphics object along with the `AWindow` to be rendered.

Several data types have been recently added to Atlantis. These include: First Level Trigger (LVL1) Regions of Interest (RoIs), silicon space points used by the

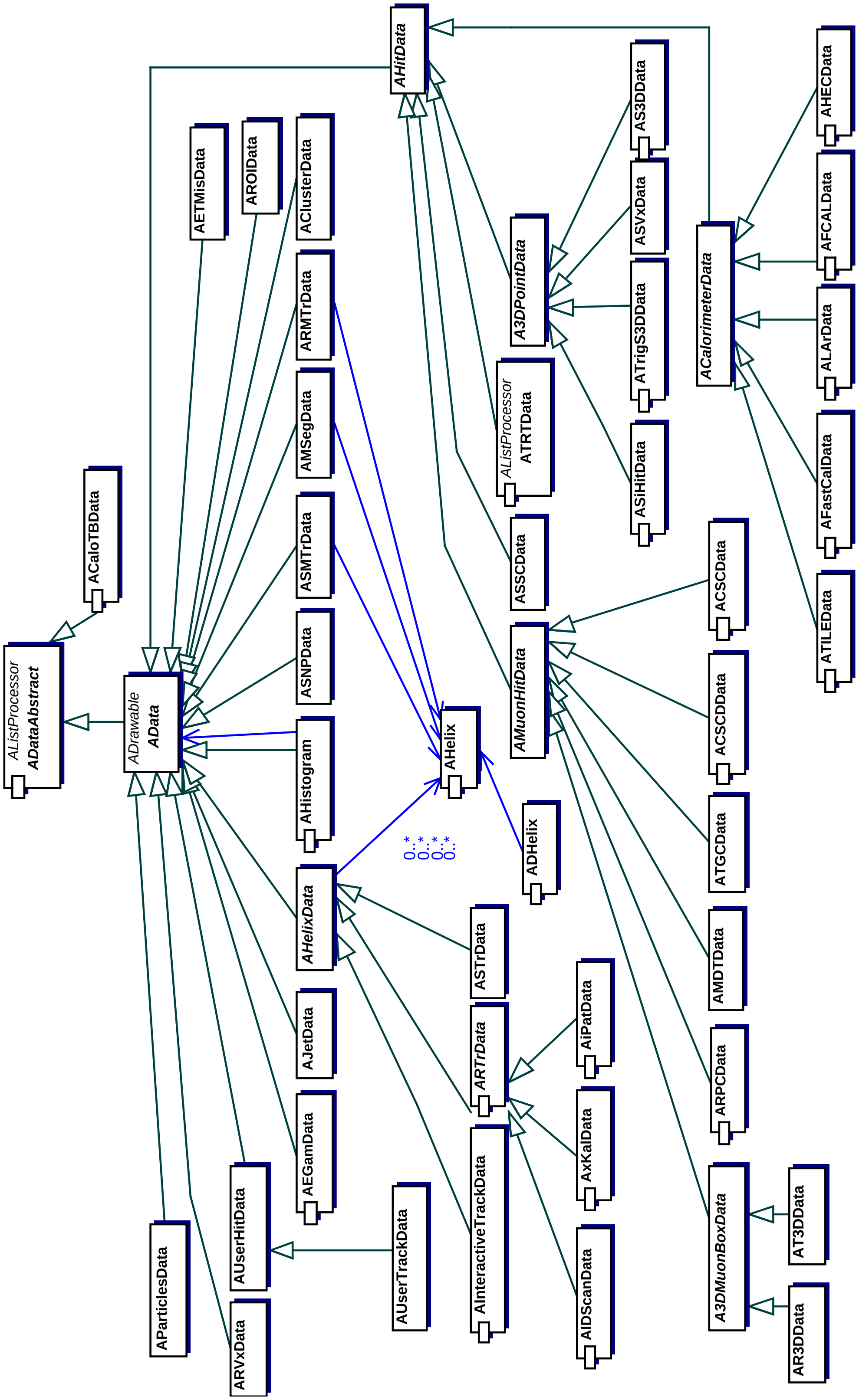

Figure 4.7: A class diagram showing the inheritance structure of the Atlantis data types.

trigger, LVL2 tracks from the algorithm IDSCAN, and pixel and SCT Geant hits. The first step of adding a new data type to Atlantis is to identify an existing data type with similar properties. The LVL1 Region of Interest (RoI) is a fairly simple data type, drawn only in the η/ϕ projection, where it takes the form of a rectangle. Therefore, the RoI data entity extends the `AData` class directly. The abstract `AData` class provides methods to cut and colour the data, but provides no implementation for drawing. The following methods have to be overridden if the data type is to be rendered in the corresponding projection: `protected ACoord getYXUser()`, where `YX` can be replaced by `RZ`, `YZ`, `XZ`, `3D`, `FR`, `FZ` or `VP`. A LVL1 RoI is only drawn in the η/ϕ projection (V-Plot) so implementation for the method `protected ACoord getVPUser()` is defined by `AROIData`. A LVL1 RoI is defined by the variables η, $\delta\eta$, ϕ and $\delta\phi$. For each RoI to be drawn the `getVPUser()` method calculates the horizontal and vertical positions in η and ϕ of the corners and returns them in an `ACoord` object.

After creating a new data entity, a couple more changes to Atlantis must be made before the data type can be displayed. Firstly, the properties of the data type must be included in the Document Type Definition (DTD) file. A DTD defines the legal building blocks of an XML document. The XML parser uses the DTD to make sure the file being read is valid and well formed. The second change is to the `AEvent` class, which defines the order in which data types are drawn. The calorimeters are drawn first, followed by tracks, then hits. The data type must be added to this sequence to be rendered. The third change is in the XML configuration file. This file defines parameters needed by the new entity to function (such as status, cut and colour parameters) and their visibility on the GUI.

Functionality must also be added to JiveXML (see section 4.4) to write the data required by Atlantis to the event XML file.

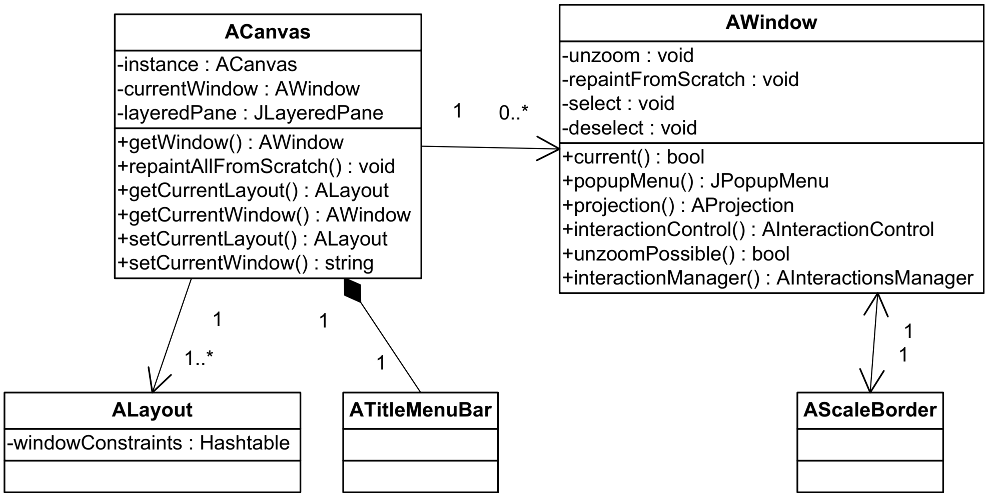

Figure 4.8: A class diagram showing the main components of the Canvas package.

4.3.3 Canvas Package

The canvas package contains classes that have the role of displaying representations of an event on the screen. The classes extend Java Swing components. Figure 4.8 depicts the relationship between the main classes of the canvas package.

The main canvas window displayed to the left of the GUI is an object of type `ACanvas`. `ACanvas` is a `JFrame` containing a `JLayeredPane` of `AWindows`. Windows are placed into the `JLayeredPane` depending on the current layout. The canvas class retains information about the possible windows and layouts available, using these to fill the `JLayeredPane` according to the size and order defined by the selected layout.

An `AWindow` is a `JPanel` into which the Atlantis graphics are drawn. Each window has an associated projection and also an interaction manager. The interaction manager is a mouse listener which deals with all mouse actions on the window. The window manages the drawing of the Atlantis picture and deals with the linear transformations from ATLAS to display co-ordinates. Non-linear transformations are dealt with by the projection.

The `JLayeredPane` is considered to be an $n \times m$ grid, where n and m depend on the selected shape of the canvas. For a square canvas this is a 3×3 grid. The

`ALayout` defines the size and position of the `AWindows` in this scheme. Possible window layouts are defined in the XML configuration file.

To render the display, the following sequence of events take place. All updates to the image originate from a call to the method `ACanvas.repaintAllFromScratch()`. This method iterates through the collection of windows held by the canvas object and asks them if they are currently visible on the screen. For the windows that are to be displayed the method `AWindow.repaintFromScratch()` is called. This obtains the current projection for that window and calls its paint method. The projection now starts the process of drawing the detector through the `ADetectorSystem`. After this, the current event is obtained from the `AEventManager` and, for each visible `AData` object, a representation is rendered to the canvas via a call to its `draw` method. If the current interaction has a presence on the display, such as a cursor, its `draw` method is called last.

4.3.4 Geometry Package

The geometry package contains classes to represent the detector. Atlantis displays an idealised detector geometry, where sub-detectors are drawn as simple blocks of colour. The co-ordinates of the outline of the blocks are read in from two XML files, AGeometry.xml and AMuonGeometry.xml.

The `AAtlasDetector` object represents the complete detector. This class contains an array of `ADetectors` objects, which can take the form `ABoxDetectors`, `ATrapezoidDetectors` or `AGeneralDetectors`. These classes manage single detector components of the same shape, holding an internal list of the respective `ADetector` objects. Each of these types of detector represents a single shape drawn to the screen, providing methods to calculate the co-ordinates of the shape in the current projection. When the detector is to be drawn, the container classes ensure that each individual `ADetector` draws itself.

4.3.5 Parameters Package

`APar` is the main parameter store for Atlantis. Users can manipulate the contents of the parameter store, using the GUI, to customise views of the event for a specific purpose. For example, by choosing whether or not to show certain data, and if so in what colour, the user can obtain a more personalised and useful display. Almost every object interacts with the `APar`. For example, `AData` objects and the `AAtlasDetector` obtain status, cut and colour parameters when requested to paint themselves on the screen. Changes to the individual parameters are made directly to the store and are followed by a call to `ACanvas.repaintAllFromScratch()`.

Parameters in the store are grouped into the following categories: projections, data status, data cuts, hit and particle colours, detector component parameters and reconstructed data types. The parameters available and their initial values are obtained from an XML file during initialisation of the program. `APar` holds a map of `AParametersGroup` objects, one for each of the categories of parameters listed above, which in turn contain maps of `AParameter` objects. The `AParameter` interface has two implementing classes, `AAbstractParameter` and `ALinkParameter`.

AAbstractParameter `AAbstractParameter` manages the value of a parameter for each window, as well as whether it is enabled in that window and its range. The `AAbstractParameter`s attributes also include Swing components that are present on the GUI, an `ACheckBox` and a `JLabel`. Six further parameter classes inherit from `AAbstractParameter`. These have additional Swing components such as `ATextField` and `AComboBox`.

ALinkParameter `ALinkParameter` is a link to a parameter contained in another `AParameterGroup`. The `ALinkParameter` contains a duplicate of the parameter and provides methods to manipulate the copied parameter as a normal parameter.

Almost all the actions on the GUI, including the Swing components of `AbstractParameter` objects, generate a command (a text string) that gets passed to the `ACommandProcessor`. When a command is received, the `ACommandProcessor` calls the `APar.processParameterChangeCommand(String)` method. This trims the provided string to a parameter name, operator and value and then calls the `processCommand(operator, value)` method for the required `AParameter`. This is followed by a call to `ACanvas.repaintAllFromScratch()`, which causes the parameter changes to be enforced.

4.3.6 Projections and Interactions Packages

The projection package contains classes representing each projection provided by Atlantis. Similarly, the interactions package contains classes representing possible user interactions with Atlantis and also classes which represent such an interaction on the GUI. There are a number of classes in the two packages that are easiest to explain along side each other. These are the main classes that facilitate the selection of interactions and projections, and provide a connection between the two. These classes are explained in turn below and a class diagram representing their static structure is shown in figure 4.9.

AProjection

Each window has a projection. The projection manages the drawing of the image to the screen, informing the `AData` objects and `ADetectorSystem` of its type. The projection deals with non-linear transformations of the image such as the fish-eye transformation.

AInteractionsManager

Each window also has an interactions manager which connects to the window in order to provide basic functionality for a given interaction. The interactions manager keeps a list of all possible interactions for the window and connects the selected interaction

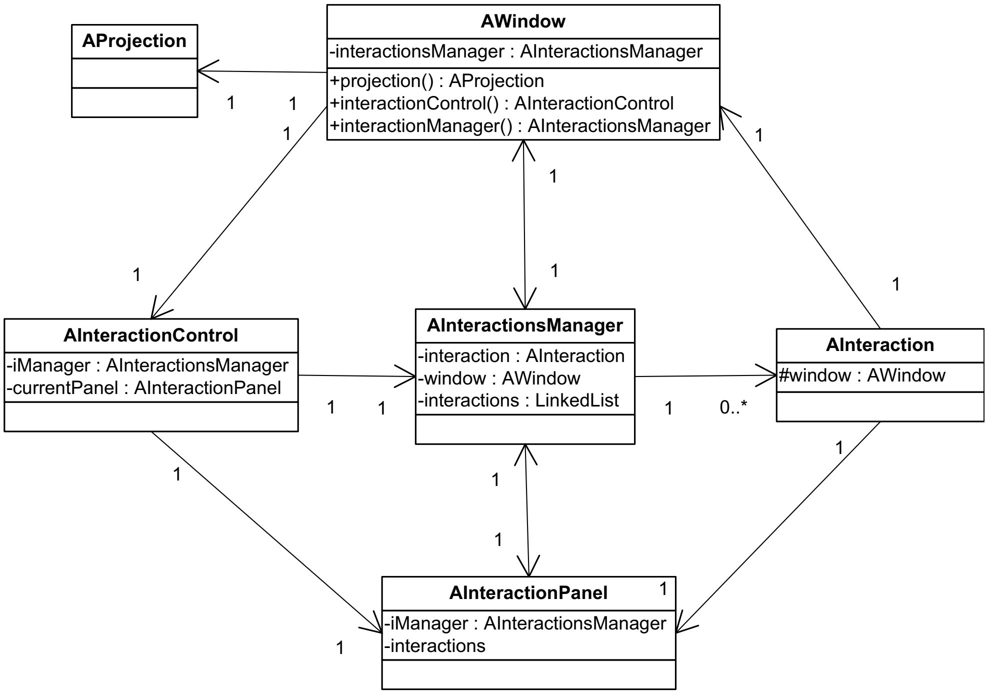

Figure 4.9: A class diagram showing the relationships between the main projection and interaction classes.

to the window to listen for events. `AInteraction` objects implement a number of `ActionListeners`, controlling changes to the display through the parameter store.

The interaction manager implements `MouseListener` and `MouseMotionListener` and defines actions carried out for right and left mouse clicks on the window, with and without three different modifier keys pressed.

The current interaction is set by selecting the appropriate tab on the GUI. This notifies the interaction manager for the current window of the change, which then connects a new interaction to the window.

AInteractionControl

This object is a `JPanel` that appears on the GUI below the window control panel. It shows the set of interactions possible for the current window in the form of a tabbed panel. Each tab displays an `AInteractionPanel` object. These panels have input Swing components, such as `JCheckBox` or `JFormattedTextField`, that alter the state of the interaction in the `APar`, causing the change to be applied when the display is re-drawn. When a new tab (interaction) is selected, the interaction manager for that window is notified about the change and the new interaction is connected to the current window.

AProjectionsManager

The projection manager holds a collection of `AInteractionControl` objects. Entries in the collection correspond to a window-projection combination. When a new projection or window is selected, the appropriate interaction control is requested by the GUI from the projection manager and displayed. Construction of the `AInteractionControl` objects is delayed until they are requested.

The projection manager holds a map of `AProjection` objects. When the projection in a window is changed, the appropriate projection object is retrieved from the projection manager and passed to the `AWindow`.

4.3.7 GUI Package

The Graphical User Interface (GUI) enables the user to interact with Atlantis. It can be used to view and modify parameters, select the projection in any given window, select the current mouse interaction for a window, read input files and save images to disk. The GUI is fully customisable, its content can be altered by editing the XML configuration file.

The GUI can be seen in figure 4.1. From top to bottom the components of the GUI are as follows:

Menu This provides functionality for input and output of files, program customisation and access to the help system.

Canvas control This can be used to select a canvas pad and to copy pictures between different canvas pads (sub-windows of the main canvas) using drag and drop. There are five different shapes of canvas available and the possible layouts for the current shape are represented on the canvas control.

Interaction control This section of the GUI provides the ability to select different user interactions with the program, such as pick and zoom. Interactions are represented in the control window as a set of tabs. Clicking on a tab makes the corresponding interaction available in the current canvas pad and displays control options in the panel just below the set of tabs.

Parameter control The parameter control is divided into seven sections. These are:

1. **Proj** - Select the projection in the current window and change parameters associated with it.
2. **Data** - Select the data types displayed and the order in which they are drawn to the screen.
3. **Cuts** - Apply cuts to the selected data, such as by $\mathrm{p_T}$ or association between hits and tracks.
4. **InDet** - Control the appearance of the data types from the inner detector.
5. **Calo** - Control the appearance of the data types from the calorimeters.
6. **Muons** - Control the appearance of the data types from the muon spectrometer.
7. **Det** - Control the colouring and display of each sub-detector.

Each of these sections contains a tabbed panel, with each tab displaying a table of `AParameter`s.

Output display This is an area where Atlantis writes out information such as a summary of the latest event read, information about selected objects or the results of the filtering or vertexing algorithm.

The AGUI constructor sets up the user interface and displays it on the screen. The AGUI is a `JFrame` containing the components listed above. The window control takes the form of an `AWindowControl` object. This displays a representation of the layouts possible and implements drag and drop capabilities between them. If a window is copied between two canvas pads the method `ACanvas.copy(String,String)` is called. The parameter control panel on the GUI is created from the `APar`, displaying the Swing components for each parameter in a table. The final component is of type `AOutput`.

4.4 JiveXML

JiveXML is a C++ algorithm that runs in the ATLAS software framework, ATHENA. When an algorithm is run in ATHENA, it places the results of its execution (reconstructed objects) in the Transient Data Store (TDS). Subsequent algorithms can then access the TDS to retrieve these data. JiveXML is scheduled to run last in the sequence of reconstruction algorithms, accessing corresponding data objects in the TDS for the requested data types and writing out their properties to an XML file.

4.5 ATLAS 2004 Combined Test Beam

4.5.1 Overview

The Combined Test Beam (CTB) was carried out between May and November in 2004. The setup [37] resembled a wedge of the final ATLAS detector, incorporating small sections of each sub-detector. The final ATLAS readout electronics were used, enabling the trigger and data acquisition system to be integrated. The following detector components were installed in the H8 beam line at CERN:

Inner Detector Six barrel modules from the pixel detector, two from each layer positioned at an angle of $\approx 20°$, as well as two modules from each of the four SCT barrel layers. The pixel and SCT layers were placed within a 1.4T bending magnet. Two barrel wedges from the TRT detector were present. Each barrel wedge is equivalent to one-sixteenth of the circumference of the TRT cylinder.

Calorimeters Two barrel modules from the LAr calorimeter and six modules of the hadronic TILE calorimeter, three from the barrel and three extended barrel modules.

Muon Spectrometer In the muon system six barrel MDT chambers were present, installed on three rails, reproducing one barrel alignment tower. Six end-cap MDT chambers, installed on three large structures, were used to reproduce the end-cap octant geometry.

Two periods of combined running took place in June and October with a 25ns bunched beam provided by the CERN 400-450 GeV Super Proton Synchrotron (SPS). The H8 beam can consist of pions, electrons, protons, muons or photons at different energies and polarities, ranging from 1 GeV up to 350 GeV. The combined test beam provided a detailed test of the particle identification and measurement capabilities of the ATLAS detector [38].

Although the CTB was designed to be as consistent as possible with the final ATLAS layout, the setup had a number of notable differences. Firstly, the distances between detector components were much larger and secondly, the calorimeter was placed on a rotating table such that different η values could be simulated. Several changes to Atlantis were necessary for it to be a useful tool at the CTB. These are described in the following sections.

4.5.2 Test Beam Geometry

Within Atlantis, the individual data types contain all the information necessary to render themselves in the coordinates of the ATLAS system. Since the same data types were available from the CTB, it should not have been necessary to make changes before Atlantis could render the event data in a useful form. When Atlantis displays the detector, it does so only in a way to convey context to the user so they can interpret the event data. For example, the hadronic calorimeter is normally drawn in red, so when the user sees a yellow block of colour drawn on top of a red background this is quickly interpreted as an energy deposit in the hadronic calorimeter. To alter the background picture of the detector drawn by Atlantis, the geometry XML file read at initialisation has to be changed. Since the CTB geometry is not static like the final ATLAS geometry, it was decided to develop an algorithm within the ATHENA framework to generate these files automatically. This enables the geometry files to be regenerated easily when a change to the setup occurs.

Inner Detector

The pixel and SCT geometry are obtained using the same method. Firstly, a collection of all active elements is retrieved from the geometry service within ATHENA. Each pixel module is an individual active element, whereas the SCT modules are two active elements positioned back-to-back with a small stereo angle between them. The collection of elements is iterated through and, for each element, an object is created for each of its corners. These can then be used to write out the co-ordinates of the shape to be drawn in both the Y/X and ρ/Z projections to the XML file.

For the TRT, each active element is an individual straw. Since each module contains many straws, it is necessary to calculate the bounds of the module from the straw positions. Figure 4.10 shows the final inner detector CTB layout.

Calorimeters

Calorimeter data read in by Atlantis are in the following form for each cell in the calorimeter: energy, η, ϕ, sub-detector and layer identification number. Atlantis then uses fixed r and z values for each sub-detector layer to draw the data to the screen. This presented a problem for the test beam setup as the r and z values of the cells differ greatly from the final ATLAS geometry. JiveXML was adapted to write out the extra data: r, δr (the extent of the cell in r), z, and δz (the extent of the cell in z) for LAr and r, δr for TILE test beam data. Two new Atlantis

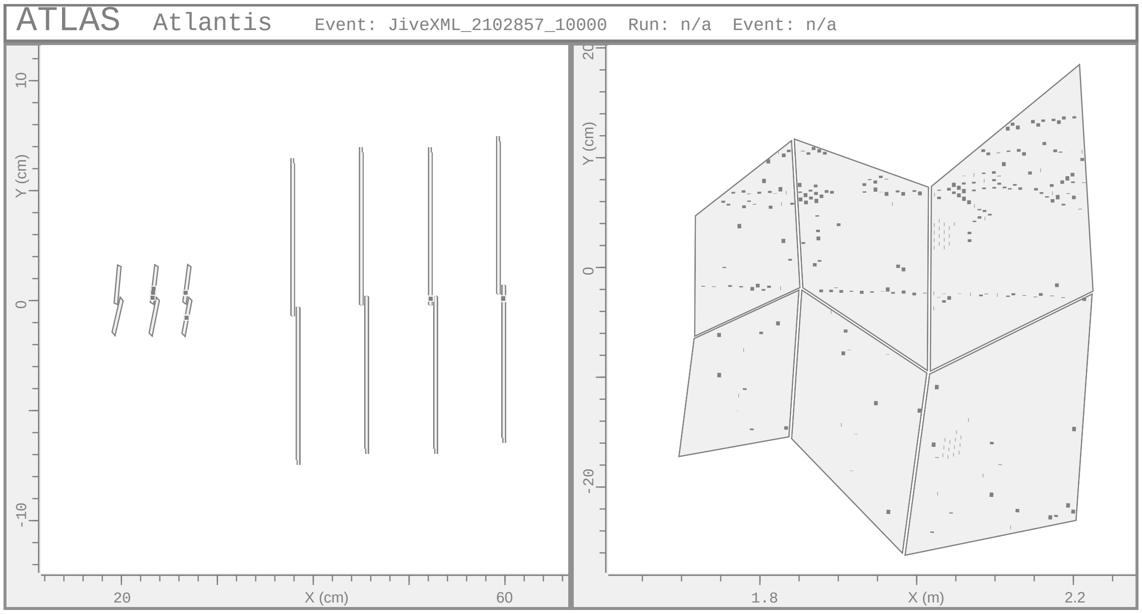

Figure 4.10: A view of the inner detector test beam layout in the Y/X projection. On the left are the three layers of pixel modules and the four layers of SCT strips. The right hand plot shows the two barrel wedges from the TRT.

classes `ALArTBData` and `ATILETBData` were developed to render the calorimeter cell independently of the hard-coded r and z values. The final solution involved applying a translation in x and rotation in ϕ to the calorimeter data before they are rendered, thus using the existing `ALArData` and `ATILEData` classes.

The detector geometry for the calorimeters is produced in a similar way to the inner detector geometry. The corresponding ϕ rotation and x translation are applied to the geometry file prior to it being read by Atlantis.

Muon Spectrometer

The muon spectrometer geometry, like the inner detector geometry, required only the creation of a new XML file detailing the shapes to be drawn. This was done by accessing the muon geometry service within ATHENA for the position and extent of the individual detector elements. Figure 4.12 shows the muon system setup in the ρ/Z projection.

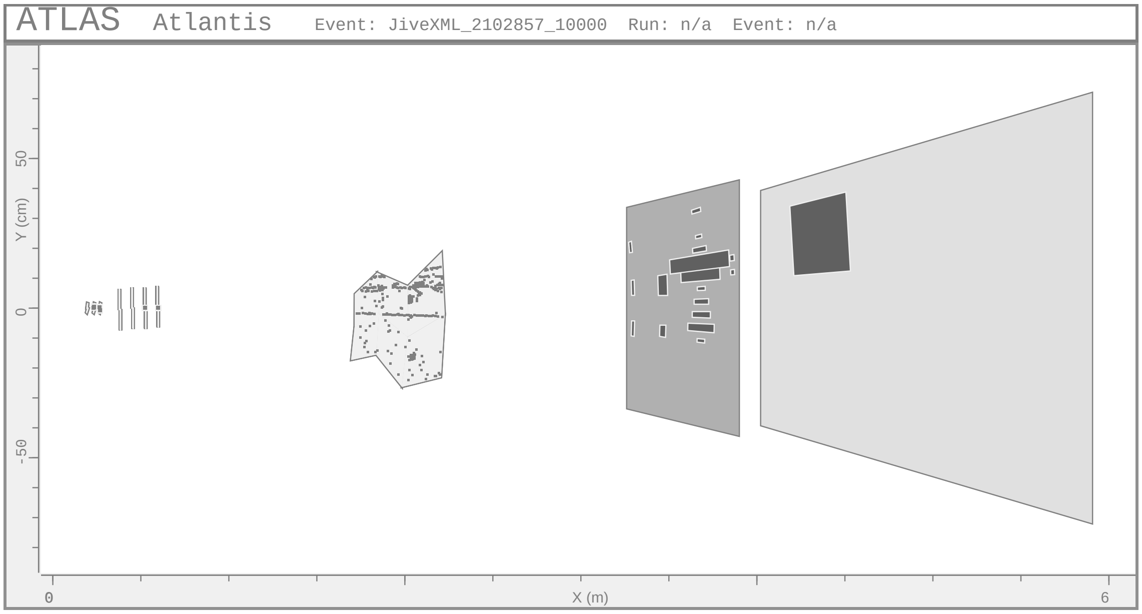

Figure 4.11: A view of the inner detector and calorimeter test beam layout in the Y/X projection.

4.5.3 Event Access Mechanism

For the test beam it was envisaged that the Atlantis display would be used in the control room to monitor events as they were read out and reconstructed. To do this, Atlantis would need to communicate with a version of JiveXML running as part of the event reconstruction software.

The simplest way to achieve this is to open a socket between the two programs, through which the data can be sent. It was unclear at the time which program would act as the server (listening for connections on a given port) and which would act as the client (connecting to the server to send or receive information). Both of these approaches were implemented in Atlantis as part of the investigation to find the best method to obtain test beam data.

The first approach is where Atlantis is a server. A separate thread is started within Atlantis to listen for connections to a given port. When the JiveXML algorithm is executed for the current event, it would create the XML data and attempt to send them to Atlantis on a known IP address and port number. Once the data are sent, or if JiveXML fails to get a response from Atlantis, the event processing

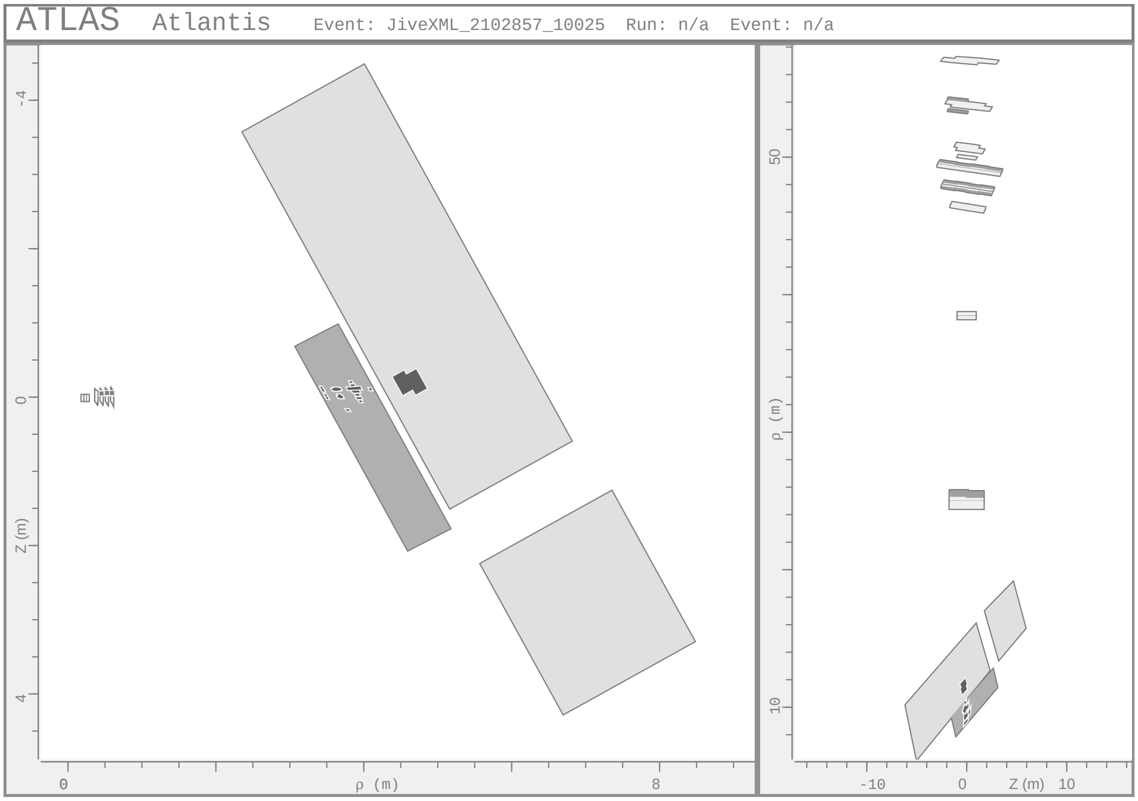

Figure 4.12: A view of the inner detector and calorimeter test beam layout (left) and Muon Spectrometer Test Beam layout (right) in the ρ/Z projection. The TRT is not shown in this projection.

would move onto the next event. In this case only one instance of Atlantis could obtain the event data from the test beam and this would have to be configured in JiveXML.

The second approach is where JiveXML acts as a server, running in a separate thread to the reconstruction chain. JiveXML would store the current event in memory, to be sent to Atlantis when requested. In this mode of operation, many users at different locations could monitor the test beam output.

In the first case, the user selects the option “Obtain event from client” from the file menu. This brings up a separate panel with options to start and stop the server. As it is possible for the user to carry out actions on the current event whilst the server is reading a new event, the methods `getCurrentEvent()` and `setCurrentEvent()` in `AEventManager` are synchronised to ensure mutually exclusive event data access.

In the second case, the “Obtain event from server” option requires the server IP address and port to be provided. Atlantis then connects to the server to obtain event data. In this case, JiveXML creates an area of shared memory when initialising. New event data are written to this area for each reconstructed event. The server thread reads event data from this area when a request from Atlantis is received.

The ability to read an Atlantis event from a network location was also developed. This included reading XML files from within a zip archive over a network, and provided the ability to navigate events within the zip file.

4.5.4 Summary

Atlantis proved itself a useful debugging tool during the CTB. For example, it helped to identify a problem with the cable mapping used in the geometry service within ATHENA for the TRT detector. This resulted in the modules being mis-identified, producing the problem visible in figure 4.13a, where the track of hits recorded in the TRT modules are not consistent with a particle travelling along the beam-line. Figure 4.13b shows the same event with this problem corrected.

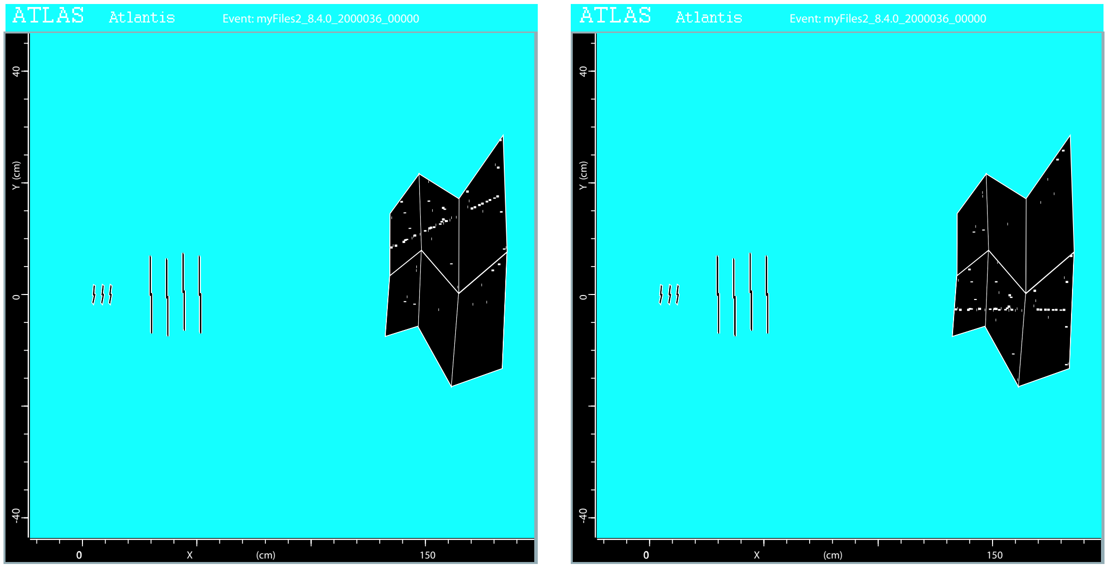

(a) (b)

Figure 4.13: TRT test beam data (a) with and (b) without the cable mapping problem.

In summary, this chapter provided an overview of the Atlantis event display.

The modifications necessary for the use of Atlantis at the 2004 combined test beam were presented, including its adaption to function in an ’online’ mode.

Chapter 5

Event Generation and Simulation

Event simulation is an essential part of high energy physics and is used in a variety of different situations. Important applications include: to aid the design and planning of a new detector, as a tool to devise and optimise strategies to analyse real data, to estimate detector acceptance corrections and to help interpret observed phenomena in terms of a more fundamental underlying theory.

The simulation of physics events at ATLAS is carried out in two main steps. Firstly, an event generator is used to simulate physics processes occurring in the pp collisions at the LHC, producing an output with the same average behaviour and the same fluctuations as is expected from real data. This is followed by a detailed or parameterised simulation of the detector response to the particles produced by the event generator. This chapter provides an overview of the event generators used in this analysis and a short description of Atlfast, the fast simulation program of the ATLAS detector.

5.1 Event Generation

The objective of an event generator is to generate events as detailed as could be observed by a perfect detector. The following, roughly time-ordered description, taken from the Pythia manual [39] gives an outline of the processes that must be simulated in a typical high-energy event:

- Initially, two beams of particles are coming toward each other. Each particle is characterised by a set of distributions that define its partonic sub-structure in terms of flavour composition and energy sharing.

- One shower initiator parton from each beam starts off a sequence of branchings, such as $q \to qg$, which build up an initial-state shower.

- One incoming parton from each of the two showers enters the hard process, where then a number of outgoing partons are produced, usually two. It is the nature of this process that determines the main characteristics of the event.

- The outgoing partons may branch, just like the incoming did, to build up final-state showers.

- When a shower initiator is taken out of the beam particle, a beam remnant is left behind. This remnant may have internal structure and a net colour charge that relates it to the rest of the final state.

- The QCD confinement mechanism ensures that the outgoing quarks and gluons are not observable but instead fragment into colour neutral hadrons.

- Many of the produced hadrons are unstable and decay further.

5.1.1 PYTHIA

PYTHIA is a general purpose Monte Carlo generator for multiparticle production at e^+e^-, pp and ep colliders. It provides around three hundred different partonic processes, all at leading order. After the generation of the basic hard process through the calculation of matrix elements, a more realistic multipartonic configuration is obtained by the addition of initial and final state showers.

In events that contain charged or coloured objects in the initial or final states, gluon or photon radiation can have large effects on the overall topology of the event.

In Pythia, these corrections are approximated by allowing partons to shower though the branching processes $q \to qg$, $g \to gg$ and $g \to q\bar{q}$, described by the evolution equations, until all partons are (essentially) on-shell. This approach provides a good description of the sub-structure of jets but has limited predictive power for the overall rate of well separated jets.

In Pythia, partons are hadronised using the Lund symmetric string fragmentation model [40]. In the Lund model, partons are connected by "strings" with a strength of 1GeV/fm. As two partons move apart the potential energy stored in the string connecting them increases until it is possible for the string to break, producing a $q\bar{q}$ pair. The system now consists of two colour-singlet $q\bar{q}$ pairs and, if the energy stored in their strings is large enough, further breaks will occur until only on-mass-shell hadrons remain.

5.1.2 AcerMC

AcerMC [41] is a dedicated event generator for key background processes at the LHC. The processes involved are characterised by heavy flavour jets and/or multiple isolated leptons in the final state. Such processes have large matrix element expressions, and to achieve a reasonable generation efficiency, it is necessary to tailor the phase-space selection procedure to the dynamics of the process. AcerMC provides a library of matrix elements and phase space modules to produce the hard process which can be passed to Pythia (or to an alternative generator such as Herwig [42]) for initial and final state radiation, hadronisation and decays to be simulated.

AcerMC includes the processes $gg, q\bar{q} \to t\bar{t}b\bar{b}$ and $gg, q\bar{q} \to (Z/W/\gamma^* \to)\ t\bar{t}b\bar{b}$, which are important backgrounds for the Higgs production and decay channel that is the focus of this thesis.

5.2 Fast Event Simulation

The Atlfast [43] package is designed to simulate the passage of generated particles through the ATLAS detector. It provides an intermediate level between a simple parton-level analysis of the event topology and a very sophisticated and CPU-intensive full detector simulation. It is a very practical tool for high-statistics studies, providing the most crucial aspects of the detector response: jet reconstruction in the calorimeters, momentum/energy smearing for leptons and photons, magnetic field effects and missing transverse energy. Atlfast is based on parameterised resolutions obtained from full simulation studies.

Calorimeter Clusters

Starting from the four-vectors of final state particles produced by the event generator, Atlfast first sums up the transverse energies of all the stable particles, except neutrinos and muons, within calorimeter cells. The cells have a granularity in η and ϕ of 0.1×0.1 for $|\eta|<3$ and 0.2×0.2 for $|\eta|>3$. The effect of the 2T magnetic field on the ϕ-position of charged particles with $\mathrm{p_T}$ above 0.5GeV is applied from a parameterisation. Clusters of calorimeter cells are then formed using a jet reconstruction algorithm, for example the default method is to group cells within a cone of $\Delta\mathrm{R}(=\sqrt{\Delta\eta^2 + \Delta\phi^2})<0.4$. Each cluster should contain at least one individual cell with E_T^{cell} >1.5GeV and have a total transverse energy greater than 10GeV. Further discussion of jet algorithms is provided in section 6.3.

Isolated Leptons and Photons

Next, Atlfast searches the particle list from the event generator for leptons and photons. The four momenta of the particles (plus the polar angle for photons) are smeared according to a parameterisation directly derived from full simulation. The parameterisation for the muon smearing is a function of $\mathrm{p_T}$, $|\eta|$, ϕ and also depends on the sub-detectors which are used for the muon measurement. The particle four-vectors obtained after smearing are then checked against particle dependant selection criteria to determine if the particle is to be retained in the simulation. For photons the requirements are $\mathrm{p_T}$>10GeV and $|\eta|$<2.5, for electrons $\mathrm{p_T}$>5GeV and $|\eta|$<2.5 and for muons $\mathrm{p_T}$>6GeV and $|\eta|$<3. To be classed as an isolated particle, the minimum ΔR to another cluster in the calorimeter must be greater than 0.4 and the total transverse energy within ΔR=0.2-0.4 of the particle must be less than 10GeV. For particles which pass the selection and isolation criteria, the associated reconstructed calorimeter cluster is identified and removed from the cluster list.

Jets

The remaining calorimeter clusters are then identified as jets if, after energy smearing, the total transverse cluster energy is greater than 15GeV. The energy of non-isolated muons that fall inside the cluster cone within $|\eta|$<2.5 are added to the smeared cluster energy. Once the jet energy is determined, the particle list is searched for a b-quark with $\mathrm{p_T}$>5GeV within a cone of radius 0.2 around the jet direction. If such a quark is found then the jet is labelled as a true b-jet. A similar search for c-quarks is also carried out.

b-tagging

The b-tagging performance of the Inner Detector is simulated by randomly tagging b-labelled jets with an efficiency ϵ_b and mis-tagging c-jets and light-jets with efficiencies ϵ_c=1/R_c and ϵ_j=1/R_j. Usually, a fixed efficiency ϵ_b is chosen and the associated rejection factors R_c and R_j obtained from full simulation studies. The most widely used values for these efficiencies are given in Table 5.1.

Atlfast provides a $\mathrm{p_T}$ dependant b-tagging parameterisation. Table 5.2 contains the correction factors applied to the efficiencies in various $\mathrm{p_T}$ ranges. Jets with $\mathrm{p_T}\simeq$ 50GeV have the highest correction factors and hence the best b-tagging performance.

Efficiency	**Low luminosity**	**High Luminosity**
ϵ_b	60%	50%
ϵ_c	10%	10%
ϵ_j	1%	1%

Table 5.1: Assumed nominal performance for b-tagging of b-labelled jets at low and high luminosity.

	***c*-jets**			**u-jets**		
Jet p_T(GeV)	ϵ_b=0.5	ϵ_b=0.6	ϵ_b=0.7	ϵ_b=0.5	ϵ_b=0.6	ϵ_b=0.7
<30	0.72	0.76	0.79	0.53	0.48	0.56
30-45	0.91	0.90	0.93	1.04	1.23	1.09
45-60	1.28	1.25	1.30	3.10	2.30	2.08
60-100	1.28	1.18	1.21	2.27	1.70	1.67
>100	1.21	1.15	1.02	0.72	1.08	1.17

Table 5.2: Correction factors for mis-tagging rates of charm- and light-jets at low luminosity.

This is due to a combination of two factors. At low p_T the impact parameter resolution of individual tracks gets worse, leading to poor b-tagging performance. At high p_T the track density increases, degrading track finding and track parameter resolutions in the jet.

Finally, the jet energy is rescaled according to the jet p_T and outcome of the flavour-tagging. The scaling factors are determined from the full simulation of $W^{\pm}H^0$ decays, with the $W^{\pm}$ decaying leptonically and H^0 decaying to $b\bar{b}$, $c\bar{c}$ and $u\bar{u}$.

Missing Transverse Energy

The missing transverse energy $\not{E}_T$ is calculated by summing the transverse momenta of identified isolated photons, electrons and muons as well as jets, clusters not accepted as jets and non-isolated muons not added to any jet cluster. Transverse energies deposited in unused cells are also included after being smeared using the same resolution function for jets.

5.3 Signal and Background Processes

Typical Feynman diagrams for the signal and background processes are shown in figure 5.1. At the LHC, $t\bar{t}H^0$ is produced 90% of the time via a gluon-gluon interaction and by a quark-quark interaction in the remaining 10%. Once produced, the top-quarks decay almost exclusively to a W boson and b-quark. W bosons decay hadronically about two thirds of the time, producing two jets in the final state. In the remaining one third of cases the W decays to a lepton and a neutrino. The branching ratios for these processes are shown in Table 5.3.

$\mathrm{t} \to \mathrm{Wb}$	0.998
$\mathrm{W} \to l\nu$	0.108 ($l = e$ or μ)
$\mathrm{W} \to$ hadrons	0.676
$\mathrm{t}\bar{t} \to l\nu bjjb$	0.291

Table 5.3: Branching ratios for top-quarks and W bosons.

The final state with the highest branching fraction is where both top-quarks decay hadronically, producing four light-jets and two b-jets. When the decay of the Higgs boson to two b-quarks is taken into account this produces a purely hadronic final state for which there is currently no trigger. Requiring one of the W bosons to

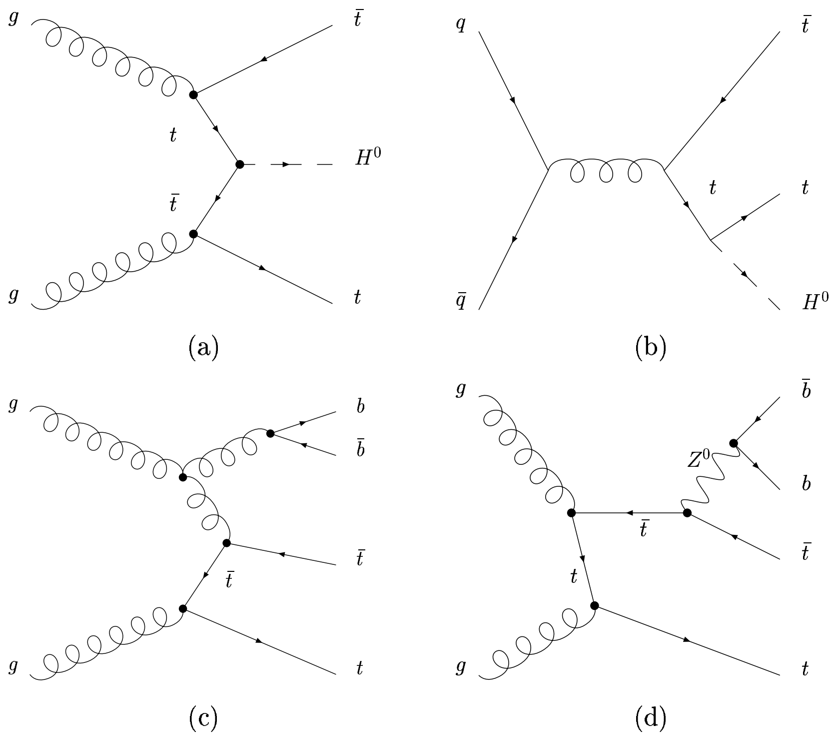

Figure 5.1: Example Feynman diagrams for the processes (a) $gg \to t\bar{t}H^0$ (b) $q\bar{q} \to t\bar{t}H^0$ (c) $gg \to t\bar{t}b\bar{b}$ and (d) $gg \to Z/W/\gamma^* \to t\bar{t}b\bar{b}$.

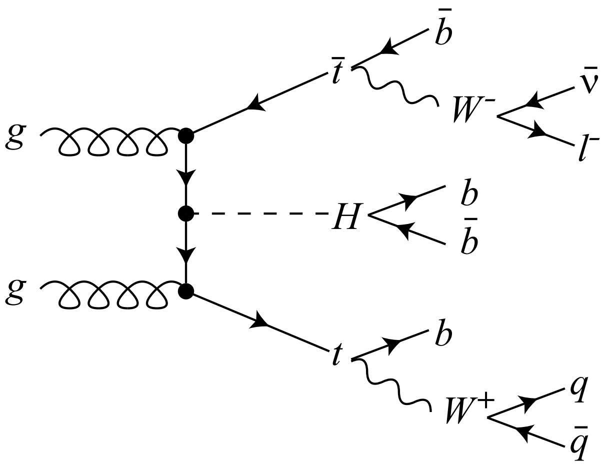

Figure 5.2: Example Feynman diagram for the process $gg \rightarrow t\bar{t}H^0$ showing the decay of the top-quarks and Higgs boson required by this analysis.

decay leptonically produces a final state with four b-jets, two light-jets, one lepton and missing momentum (figure 5.2). Only electrons and muons are considered in this analysis.

A representation of a signal event in the detector created using the Atlantis event display [44] is shown in Figure 5.3. The Y/X view of the event, shown in the top plot, is looking along the beam pipe at the barrel section of the detector. The display has a fish-eye transformation applied, magnifying the inner parts of the detector and compressing the outer systems. The trigger lepton, in this case a muon, can be seen as hits in the muon system in the right hand side of the image. Five jets are visible in this projection and can clearly be seen by the calorimeter deposits, represented by both squares proportional to the energy deposited in a particular cell and also a histogram which represents the total energy deposited in all layers of the particular calorimeter. The large arrow in the display represents the missing transverse energy in the event, which can be considered to be the direction of travel of the neutrino. The lower plot is a display of the same event in the ρ/Z projection, again with a fish-eye transformation applied. In this projection, all the main detector components can be displayed without overlapping. The sixth jet can be seen in the calorimeter end-caps.

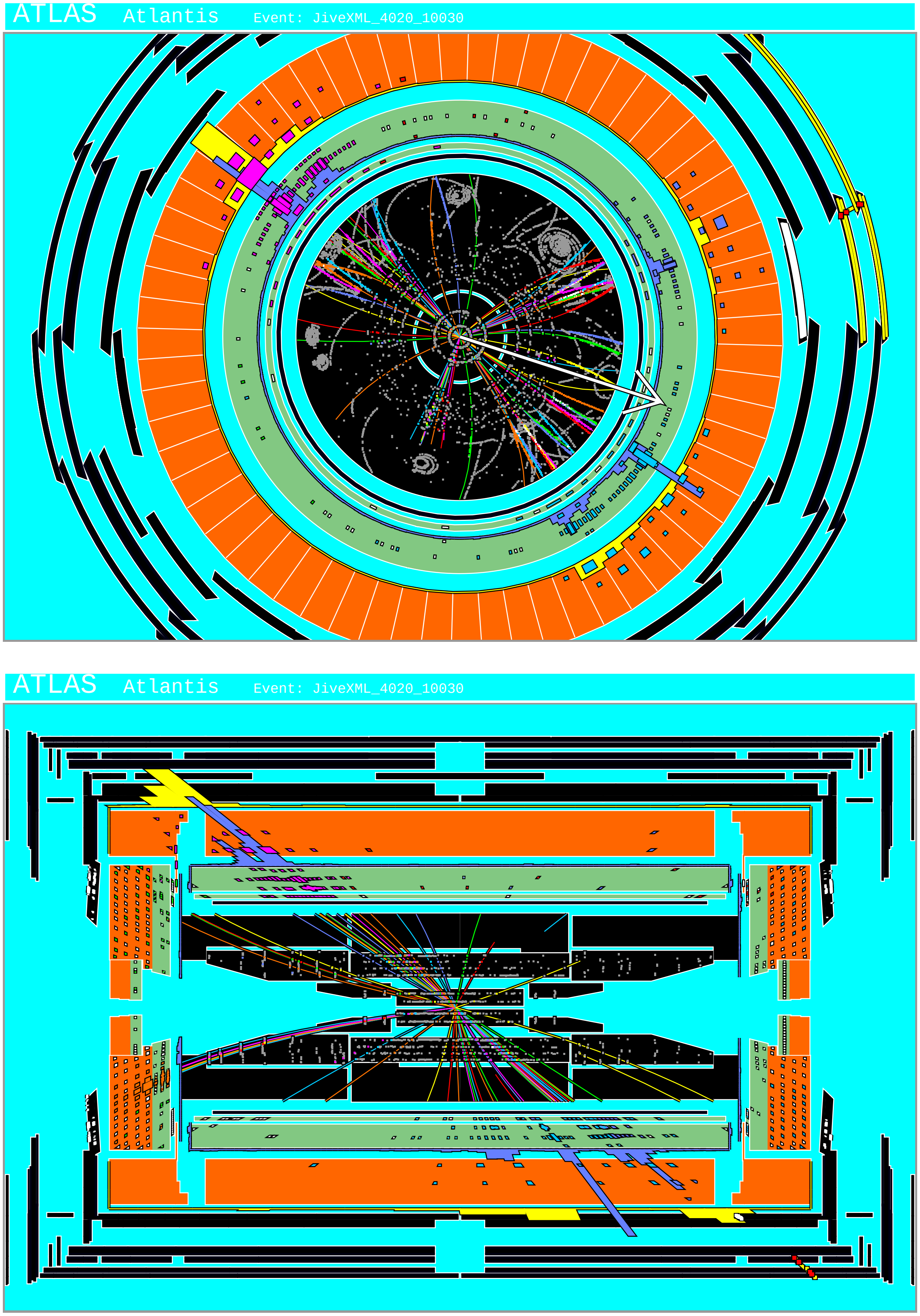

Figure 5.3: An Atlantis display showing a $t\bar{t}H^0, H^0 \rightarrow b\bar{b}$ event in the XY projection (top) and the ρZ projection (bottom).

Process	Generator	σ_{incl} (pb)	Generated events
$t\bar{t}H^0$	Pythia	see Table 5.5	1M
$gg \to t\bar{t}b\bar{b}$	AcerMC	8.1	2M
$q\bar{q} \to t\bar{t}b\bar{b}$	AcerMC	0.5	2M
$gg \to Z/W/\gamma^* \to t\bar{t}b\bar{b}$	AcerMC	0.9	1M
$t\bar{t}jj$	Pythia	474	19.2M

Table 5.4: Signal and background samples used in this analysis.

m_H (GeV)	σ_{incl} (pb)	BR($H^0 \to b\bar{b}$)
115	0.582	0.737
120	0.519	0.684
125	0.463	0.616
130	0.416	0.533
135	0.374	0.442
140	0.337	0.349

Table 5.5: Inclusive signal cross-sections and branching ratios [45].

The main background to this signal process is from top-quark pair production, with additional jets from initial or final state radiation. This background is approximately nine hundred times larger than the signal, but the additional jets are dominantly light flavour jets and a large proportion of this background can be effectively suppressed by requiring four b-jets. There is also a less severe $gg, q\bar{q} \to t\bar{t}b\bar{b}$ background which is mediated by electroweak gauge bosons (see figure 5.1d), $gg, q\bar{q} \to (Z/W/\gamma^* \to)\ t\bar{t}b\bar{b}$. The cross-section for this process is about nine times smaller than the QCD $gg, q\bar{q} \to t\bar{t}b\bar{b}$ production.

Table 5.4 details the Monte Carlo samples used in this analysis. Signal events were generated with Pythia 6.226 [39] for Higgs boson masses from 115 to 140GeV in increments of 5GeV. The $gg, q\bar{q} \to t\bar{t}b\bar{b}$ backgrounds have been produced using AcerMC 2.3 [41]. Since no matrix element based generator exists for $t\bar{t}$+jets, Pythia has been used to create the $t\bar{t}jj$ background with a veto for the case when the additional jets created from the parton shower are true b-jets.

The cross-sections for the signal process were calculated with the HQQ program [46] and the branching ratios of $H^0 \to b\bar{b}$ were calculated with the HDECAY program [47]. Cross-sections for the background processes were taken from the event generators. The renormalisation and factorisation scales $Q^2_{QCD} = (m_t + m_{H^0}/2)^2$ were used for the signal and $gg, q\bar{q} \rightarrow t\bar{t}b\bar{b}$ backgrounds. A value of $\mathrm{m_H}$=120GeV was used in the generation of the $gg, q\bar{q} \rightarrow t\bar{t}b\bar{b}$ backgrounds. For the $t\bar{t}jj$ background the PYTHIA default scale $Q^2_{QCD} = (m_t^2 + p_T^2)$ was used, where p_T is the transverse momentum of the scattering process. In all cases the CTEQ5L structure functions [48] have been used.

CHAPTER 6

Standard Model Higgs Production with Associated Top-quarks

This chapter presents the analysis carried out on the $t\bar{t}H^0, H^0 \rightarrow b\bar{b}$ channel. A short introduction is given discussing previous studies of the channel, followed by an outline of the current analysis technique used and updated results for the data samples created for this study. Areas of possible improvement which were looked into include techniques to improve the hadronic W reconstruction, the top quark selection and use of an Artificial Neural Network (ANN) for signal and background separation. Although b-tagging and the effect of the triggering system both have a large impact on this channel, their effect is not studied here. The parameterised b-tagging from ATLFAST and an overall trigger efficency of 90% were used in this analysis.

6.1 Introduction

The discovery potential of the channel $t\bar{t}H^0, H^0 \rightarrow b\bar{b}$ at the LHC was first investigated in reference [49] in preparation for the ATLAS technical proposal in 1994. Events with an isolated lepton and either three or four b-tagged jets were selected using simple p_T and η cuts. Several scenarios were then used to select the b-jets from the Higgs boson. These included using all three combinations of jets and weighting each one by a factor of 1/3, as well as using the combination of jets with the lowest p_T. The paper demonstrated the strengths of the channel: it does not have to compete with the Z-resonance which causes a difficult background to other channels in the mass range of its initial study and also demonstrated the need to reduce the combinatorial background caused by the large number of b-quarks present in the final state.

Partial and full event reconstruction was first implemented in reference [50] and the results of the analysis have been presented in the Physics Technical Design Report (TDR)[20]. Reconstruction of both top-quark decays has been shown to be useful in suppressing the combinatorial background as well as keeping the $t\bar{t} + jets$ background under control. In the next section an overview of the TDR analysis is given with updated plots and figures for the current Monte Carlo generators and parameters. Following this are sections investigating possible improvements for each stage of the analysis. The event numbers and significance values presented in this chapter correspond to those expected from three years of initial/low luminosity LHC running. This is equivalent to an integrated luminosity of 30fb^{-1}.

6.2 TDR Analysis

The TDR analysis consists of four steps. These are the application of simple pre-selection cuts, creation of hadronic W ($W \to jj$) then leptonic W ($W \to l\nu$) candidates, followed by the reconstruction of a top-quark pair from the W candidates and b-jets in the event using a minimisation procedure. The remaining b-jets are then assigned to the Higgs decay.

6.2.1 Pre-selection

The first step of the analysis is to select events with a topology compatible with that of the signal. The selection of an isolated lepton is based on the cuts employed in the trigger system.

- **One trigger lepton**

  With $\mathrm{p_T}^e > 25$GeV or $\mathrm{p_T}^\mu > 20$GeV within $|\eta| < 2.5$ (this corresponds to the region in η occupied by the inner detector). A reconstruction efficiency of 90% is applied to the lepton, this is the expected efficiency from the trigger.

- **At least six jets**

  With $\mathrm{p_T} > 20$GeV and $|\eta| < 5$ (the extent of the calorimeter system in η).

- **At least four jets tagged as *b*-jets**

Figure 6.1 shows the lepton and jet multiplicities in signal and background events. The average number of b-jets in a signal event is 2.0 compared to 1.6 for $t\bar{t}b\bar{b}$ and 1.0 for $t\bar{t}jj$ events. Plots of the lepton and jet $\mathrm{p_T}$ values are also presented. The $t\bar{t}jj$ background has a softer $\mathrm{p_T}$ spectrum for both b- and light-jets than the signal and $t\bar{t}b\bar{b}$ background.

6.2.2 Reconstruction of W→ jj

Hadronic W candidates are created from pairs of light-jets in the event. All pairs that have an invariant mass, m_{jj}, within ±25GeV of the nominal W mass are kept as candidates and their energies rescaled such that $m_{jj} = m_W$. The rescaling is carried out so that the error on the jet energy measurement does not have an impact again when the top-quarks are reconstructed. Figure 6.2 shows the distribution of m_{jj} for all possible jet-pair combinations in signal events. The dashed histogram in this plot shows m_{jj} for combinations of jets where both light-jets have been matched to the decay products of the true W using the Monte Carlo event record.

6.2.3 Reconstruction of W→ $l\nu$

Reconstruction of the leptonic W is limited as it is impossible to fully reconstruct the neutrino four-momentum. While p_x and p_y can be estimated from the missing transverse momentum in the event, this is not possible for p_z due to the incomplete

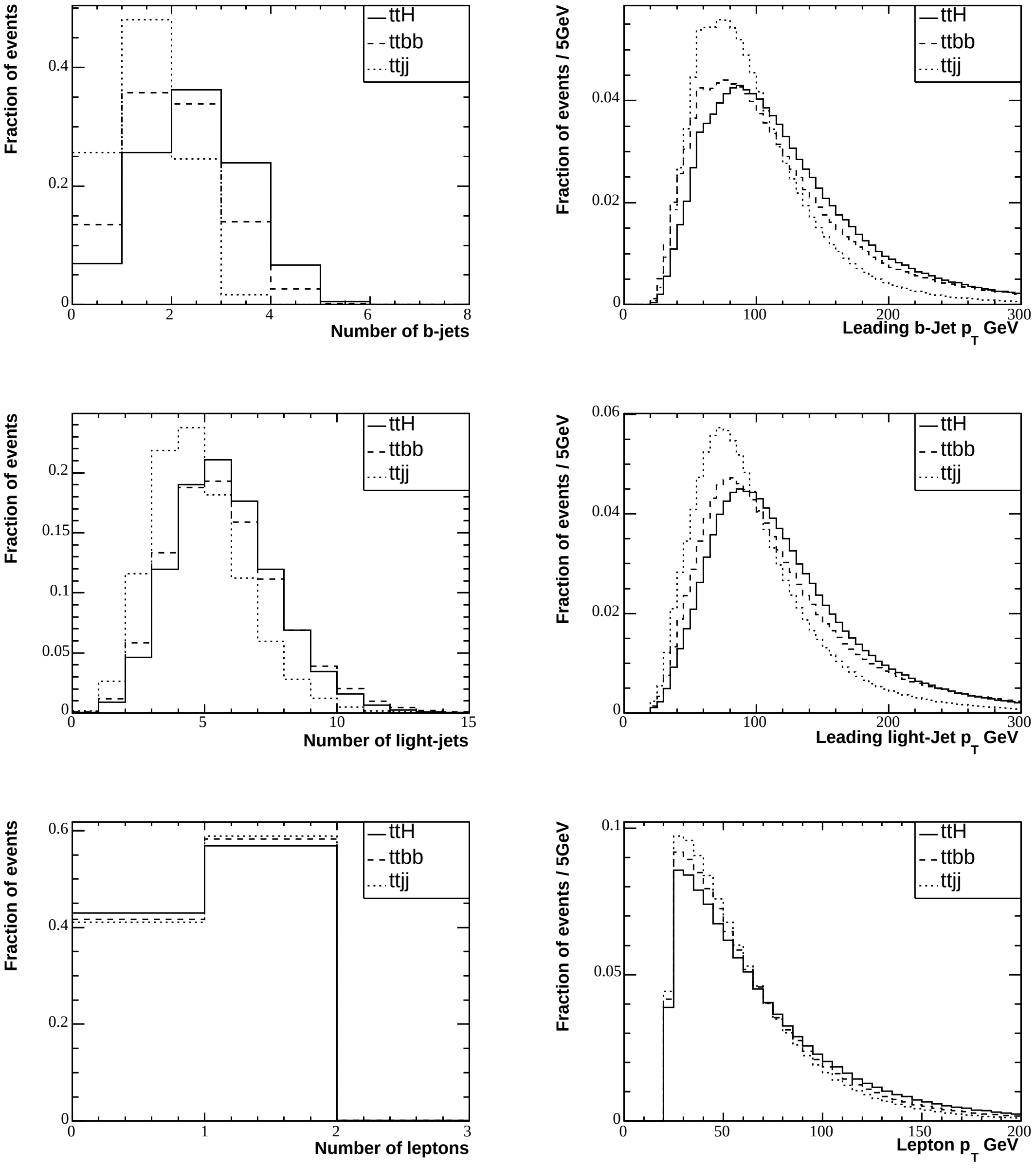

Figure 6.1: Lepton, light-jet and b-jet multiplicities and p_T distributions for signal and background events. Histograms are normalised to unit area.

coverage of the detector around the beam pipe. Assuming the transverse components of the neutrino momentum are equal to the corresponding components of the missing energy in the event, it is possible to attempt to recover some information about p_z^ν by solving equation 6.1 for the mass of the W boson (using $p_x^\nu = p_x^{miss}$, $p_y^\nu = p_y^{miss}$

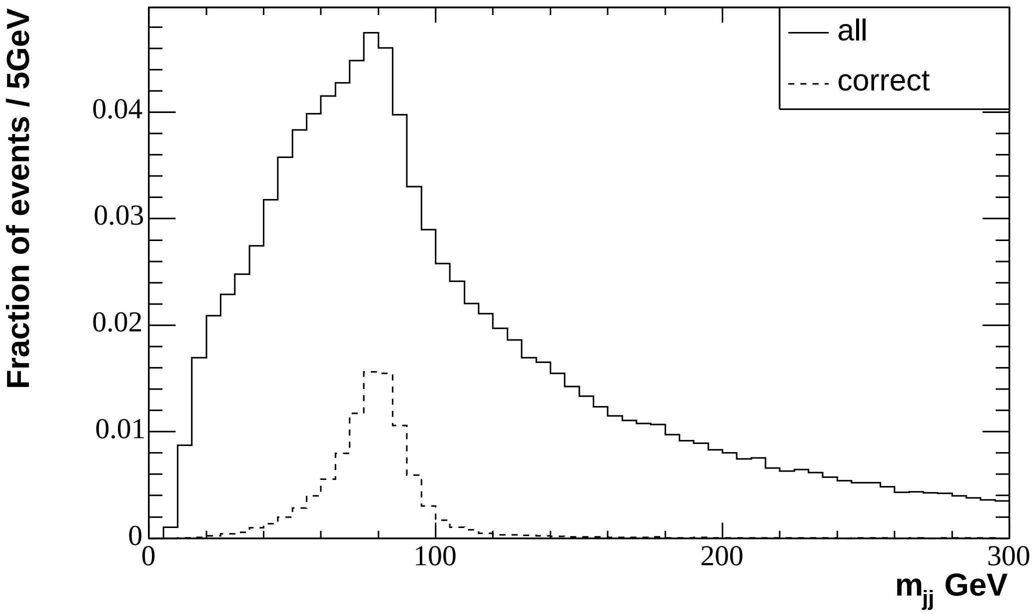

Figure 6.2: Invariant mass of light-jets pairs in signal events. The dashed histogram is the invariant mass distribution for jet-pairs where the jets are known to be from the hadronically decaying W. The histogram for all jet pairs is normalised to unit area.

and assuming the neutrino is massless).

$$m_W^2 = (E^\nu + E^l)^2 - (p_x^\nu + p_x^l)^2 - (p_y^\nu + p_y^l)^2 - (p_z^\nu + p_z^l)^2 \tag{6.1}$$

In 75% of signal events, solutions to this equation can be found. For all other cases there has been a significant mis-measurement of $\not{p}_{\mathrm{T}}$ and the event is rejected. Figure 6.3 shows the resolution for p_x^ν and p_z^ν for events that reached the final stage of the reconstruction procedure. A Gaussian fit to the centre of the distributions gives σ=15GeV for p_x^ν and σ=20.5GeV for p_z^ν. The large tails in the p_z^ν distribution are due to the wrong neutrino solution being chosen in the reconstruction of the top-quark pair (section 6.2.4). The resolution for p_z^ν is worse than that of p_x^ν, as it incorporates errors from each of the variables used in its calculation.

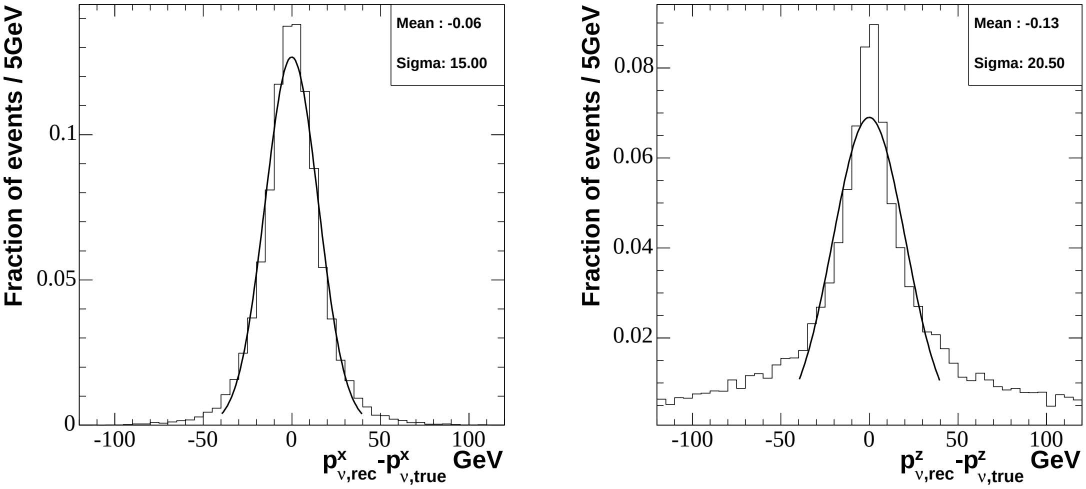

Figure 6.3: Resolution of the reconstructed neutrino (a) p_x component and (b) p_z component. Distributions are normalised to unit area.

6.2.4 Reconstruction of Top-quarks

Both top-quarks are reconstructed simultaneously finding the combination of b-jets and W candidates that minimises equation 6.2.

$$\Delta^2 = (m_{l\nu b} - m_t)^2 + (m_{jjb} - m_t)^2 \tag{6.2}$$

Figure 6.4 shows the mass distributions for the reconstructed top-quarks. A Gaussian fit was performed over the range 160-190GeV, giving values of σ=7.1GeV for the mass of the hadronically decaying top-quark, m_{jjb}, and σ=8.7GeV for the mass of the semi-leptonically decaying top-quark, $m_{l\nu b}$. A cut is applied to keep events where both reconstructed top masses lie within ±20GeV of the nominal top mass. 80% of events pass this cut.

Finally, the remaining b-jets are assigned to the Higgs boson decay. In the rare case (6%) of more than two b-jets remaining, the two with the highest $\mathrm{p_T}$ are chosen. Figure 6.5 shows the mass distribution of the reconstructed Higgs boson. The dashed histogram represents events where the correct b-jets were assigned to the Higgs decay.

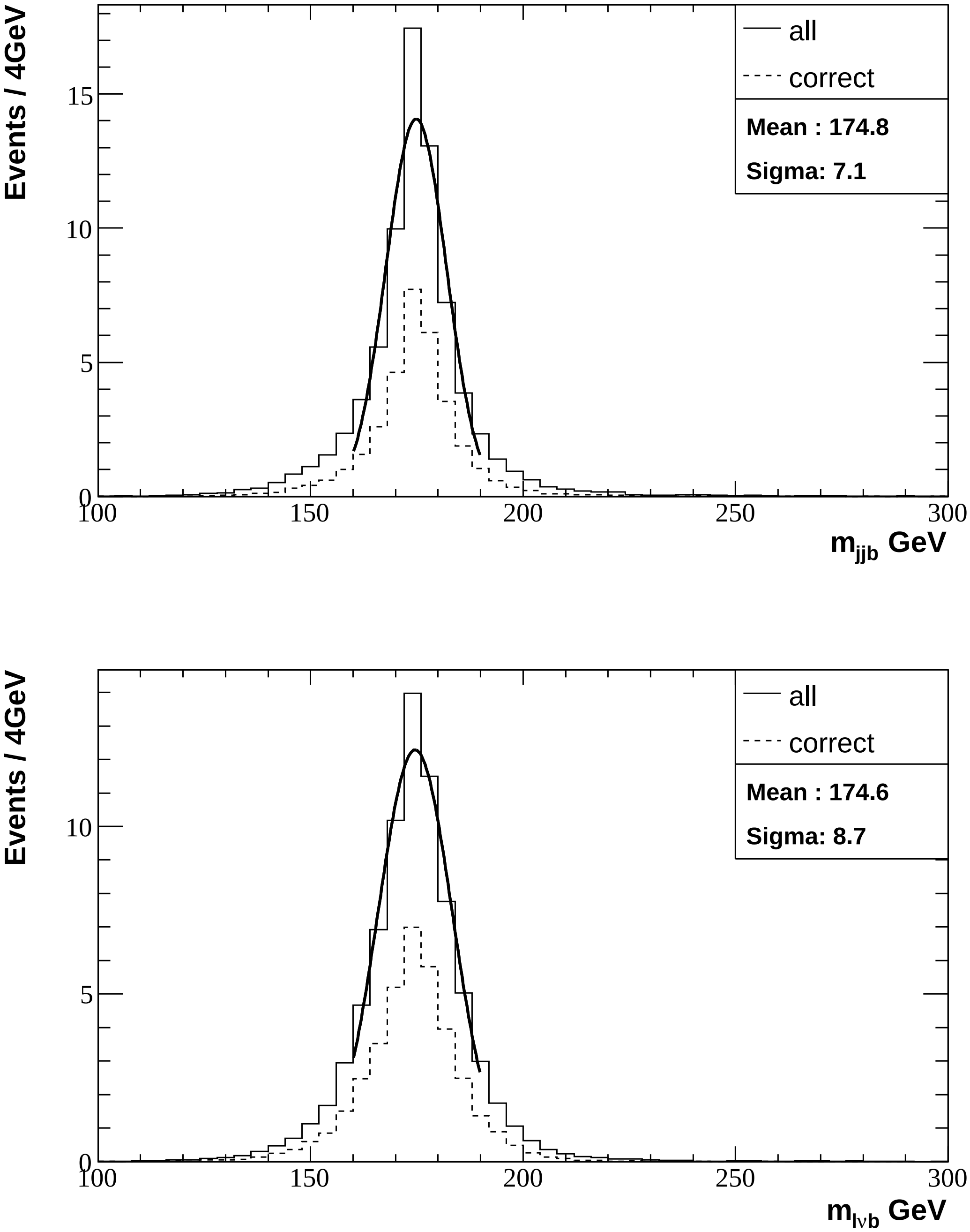

Figure 6.4: Distribution of m_{jjb} (top) and $m_{l\nu b}$ (bottom) for reconstructed top-quarks. The dashed histogram represents correctly reconstructed top-quarks. The histograms are normalised to the rate of expected events for L=30fb^{-1}.

Events within a ±30GeV window of the nominal Higgs boson mass are retained at the end of the analysis. This defines the region that the significance of a Higgs signal is evaluated within. The window also has the effect of reducing the incorrectly reconstructed signal events and reducing the number of background events.

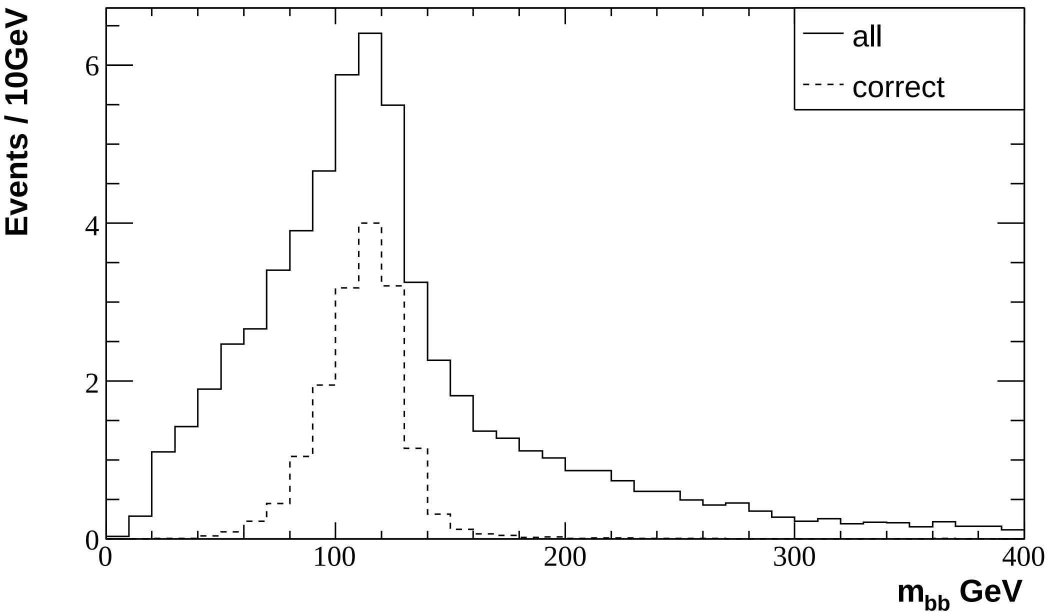

Figure 6.5: Mass distribution for the reconstructed Higgs boson (m_H=120GeV). The histogram is normalised to the expected number of events for L=30fb^{-1}. The dashed histogram represents events where the Higgs boson decay was correctly reconstructed.

6.2.5 Results

The efficiencies for each stage of the analysis are shown in Table 6.1. The overall reconstruction efficiency for signal events is 0.9%. The requirement of four b-jets has the greatest impact on the number of signal events, reducing it by 92%, however this cut has a much larger effect on the main backgrounds. In the case of the $t\bar{t}jj$ background, where the extra two jets are not true b-jets but a product of mis-tagging, the number of events after this cut is 0.09% of the level it was before.

The requirement of reconstruction of the top-quarks has a similar effect on the $t\bar{t}b\bar{b}$ backgrounds and $t\bar{t}H^0$ signal. It has a greater effect on the $t\bar{t}jj$ background

Cut	$t\bar{t}H^0$ (120) (%)	$t\bar{t}b\bar{b}$ (QCD) (%)	$t\bar{t}jj$ (%)	$t\bar{t}b\bar{b}$ (EW) (%)
1l and 6 jets	47.7	39.9	21.7	37.8
4 b-jets	3.8 (8.0)	1.5 (3.8)	0.019 (0.09)	1.6 (4.2)
2 tops reconstructed	2.4 (63.6)	0.97 (63.2)	0.010 (53.3)	1.0 (62.9)
m_t inside mass window	1.95 (80.2)	0.75 (77.6)	0.007 (69.1)	0.77 (77.4)
m_{bb} inside mass window	0.90 (46.1)	0.18 (24.5)	0.002 (31.6)	0.22 (28.7)

Table 6.1: Efficiencies for each step of the analysis. The relative efficiencies with respect to the previous step are given in parenthesis. The '2 tops reconstructed' efficiency includes the cuts on the reconstructed W Boson masses.

where the W jets are more likely to be mis-tagged as b-jets for the event to pass the b-tagging cut. In this case incorrect jets would be used to reconstruct the W boson, making the event more likely to fail the W mass cut which is part of the top reconstruction efficiency.

Cut	$t\bar{t}H^0$ (120)	$t\bar{t}b\bar{b}$ (QCD)	$t\bar{t}jj$	$t\bar{t}b\bar{b}$ (EW)	ΣBkg
1l and 6 jets	1480	30036	895855	2936	928827
4 b-jets	119	1152	771	123	2046
2 tops reconstructed	75.6	727.6	411.8	77.1	1216.5
m_t inside mass window	60.6	564.7	284.2	60.8	910.0
m_{bb} inside mass window	27.9	138.6	90.0	17.5	246.0

Table 6.2: Expected signal and background events after each stage of the analysis for L=30fb^{-1}.

For an integrated luminosity of 30fb^{-1}, equivalent to three years of initial LHC running, the number of events expected after each stage of the analysis are given in Table 6.2. Figure 6.6 shows the combined signal and background mass distribution for the reconstructed Higgs boson for this integrated luminosity. For Higgs boson masses from 115 to 140GeV, the expected number of signal and background events are listed in Table 6.3. The significance for a 115GeV Higgs boson is 2.08 dropping to 0.62 for a 140GeV Higgs.

These results for the signal and $t\bar{t}b\bar{b}$ backgrounds agree with an updated analysis performed in 2003 [51]. However, in this analysis the $t\bar{t}jj$ background after reconstruction is larger by approximately a factor of two. The first requirement of one lepton and six jets has a 40% higher efficiency relative to the results reported in

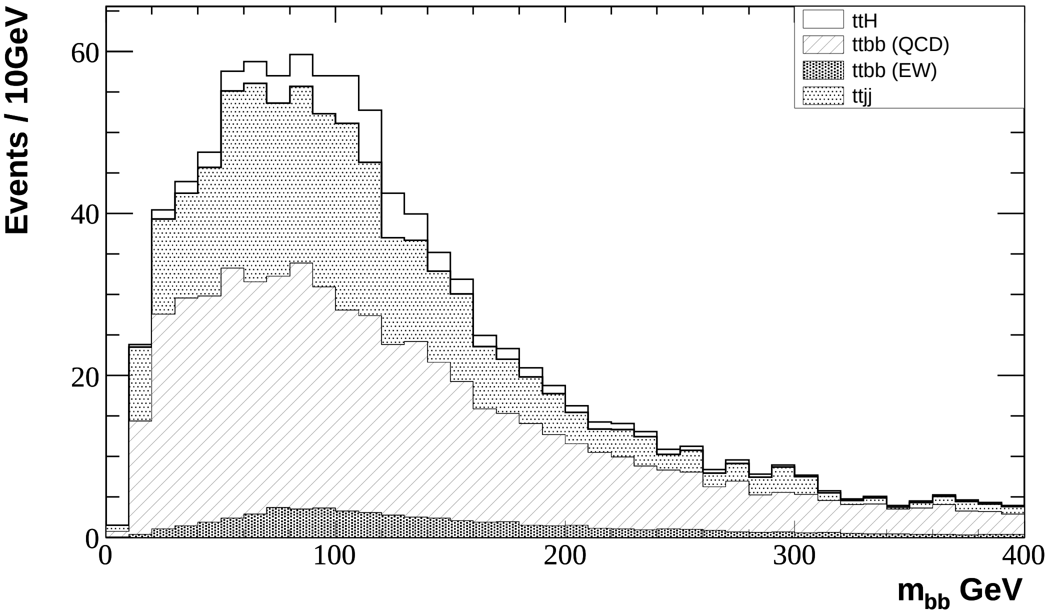

Figure 6.6: The combined reconstructed Higgs mass distribution (signal m$_H$=120GeV and background) for L=30fb^{-1}.

[51]. The $t\bar{t}b\bar{b}$ background also sees a small increase of 8%, but this is compensated for by a slightly lower efficiency for the requirement of four b-jets. The discrepancy is most likely to be due to the differing PYTHIA versions used (6.226 in this analysis and 6.203 in [51]). Changes between the two versions include a different tuning for the underlying event. A previous version, 6.224, without the new tuning was run to gauge the effect of this particular change on this background. The results are shown in table 6.4.

m$_{H^0}$ (GeV)	**115**	**120**	**125**	**130**	**135**	**140**
$\epsilon_{t\bar{t}H^0}$ (%)	0.89	0.90	0.88	0.87	0.84	0.84
$t\bar{t}H^0$	33.3	27.9	22.0	16.9	12.1	8.7
$t\bar{t}b\bar{b}$(QCD)	143.6	138.6	133.0	128.4	123.8	117.6
$t\bar{t}jj$	95.1	89.9	85.0	80.5	74.0	66.7
$t\bar{t}b\bar{b}$(EW)	18.1	17.5	16.7	15.9	15.1	14.5
ΣBkg.	256.7	246.0	234.7	224.8	213.0	199.0
S/$\sqrt{B}$	2.08	1.78	1.44	1.13	0.83	0.62

Table 6.3: Expected signal and background events (L=30fb^{-1}) for Higgs masses from 115 to 140GeV in increments of 5GeV.

	PYTHIA 6.226	PYTHIA 6.224	Results from [51]
1l and 6 jets	21.7	21.5	15.4
4 b-jets	0.019 (0.09)	0.017 (0.08)	0.01 (0.1)
2 tops reconstructed	0.010 (53.3)	0.008 (47.8)	0.005 (45.6)
m$_t$ inside mass window	0.007 (69.1)	0.006 (71.3)	0.003 (65.3)
m$_{bb}$ inside mass window	0.0022 (31.6)	0.0017 (28.4)	0.001 (34.1)

Table 6.4: Comparison of cut efficiencies on the $t\bar{t}jj$ background for each stage of the analysis between PYTHIA 6.226 and 6.224. The efficiencies found in [51] using PYTHIA 6.203 are also shown.

The number of events passing the true b-jet veto for this background is inline with the 19.3M events from a total of 20M that [51] reports. For the $t\bar{t}jj$ sample created with version 6.226 this figure is 19.2M. While the efficiency of the one lepton and six jets requirement remains high in the PYTHIA 6.224 sample, the discrepancies between this and both other samples indicates that the PYTHIA version used has a large effect on this background.

The results of using an η cut of 2.5 for all jets in the event is shown in table 6.5. The main effect of this change is on the $t\bar{t}jj$ background, experiencing a 14% reduction in final event numbers compared to a 7% drop for all other samples. The drop in signal events however has a larger impact on the significance, reducing it to 1.75 making this cut unfavourable.

Cut	$t\bar{t}H^0$ (120)	$t\bar{t}b\bar{b}$ (QCD)	$t\bar{t}jj$	$t\bar{t}b\bar{b}$ (EW)	ΣBkg
1l and 6 jets	1275	23493	561257	2185	586934
4 b-jets	113	1094	670	116	1880
2 tops reconstructed	70.8	676.4	353.6	71.0	1101.0
m$_t$ inside mass window	56.8	524.5	250.4	55.9	830.8
m$_{bb}$ inside mass window	26.1	129.2	77.1	16.0	222.3

Table 6.5: Expected signal and background events after each stage of the analysis for L=30fb^{-1} with the additional constraint of the light jets being within $|\eta|$<2.5.

Parton-jet Matching

In order to obtain more information about the performance of the reconstruction method, each of the six initial quarks from the Monte Carlo generator (two light quarks from the W decay and four b-quarks from the top and Higgs decays) are matched to the reconstructed jets. This is done by calculating $\Delta\text{R}(=\sqrt{\Delta\phi^2+\Delta\eta^2})$ for all combinations of jets and initial quarks and creating associations starting from the minimum ΔR value up to a cut-off of ΔR=1.0. Only one jet is associated with each of the quarks.

For events that pass the pre-selection it is possible to assign jets to each of the six initial quarks in 70% of cases. After top reconstruction this increases to 77.2% of cases. Of these matched events after top reconstruction, figure 6.7 shows the contributions to the reconstructed Higgs mass distribution from events falling into the following categories:

- Events where one or more of the jets have been b-tagged incorrectly, this accounts for 36.3% of events that can be matched to the truth data.
- Events that have correctly b-tagged jets and from these the correct b-jets have been used to reconstruct the Higgs boson.
- Events that have correctly b-tagged jets but where one or both jets used to reconstruct the Higgs boson are incorrect.

Out of the correctly tagged events, 40% fall into the second of the three categories. With the added requirement of the correct jets also being used to reconstruct the top-quarks, the correct assignment of all jets is made in 37% of correctly tagged events (3% less than just requiring the correct jets for the Higgs boson). When the Higgs mass window is applied, these values increase to 64% and 59% respectively.

Removing the requirement of the events being matched and correctly tagged gives an overall value of 26% for the correct jets being assigned to the Higgs boson. With the Higgs mass window applied this value is 50%.

Conclusions

Of the events passing the pre-selection cuts, 30% have significant Final State Radiation (FSR) such that the reconstructed jets cannot be matched to the initial quarks

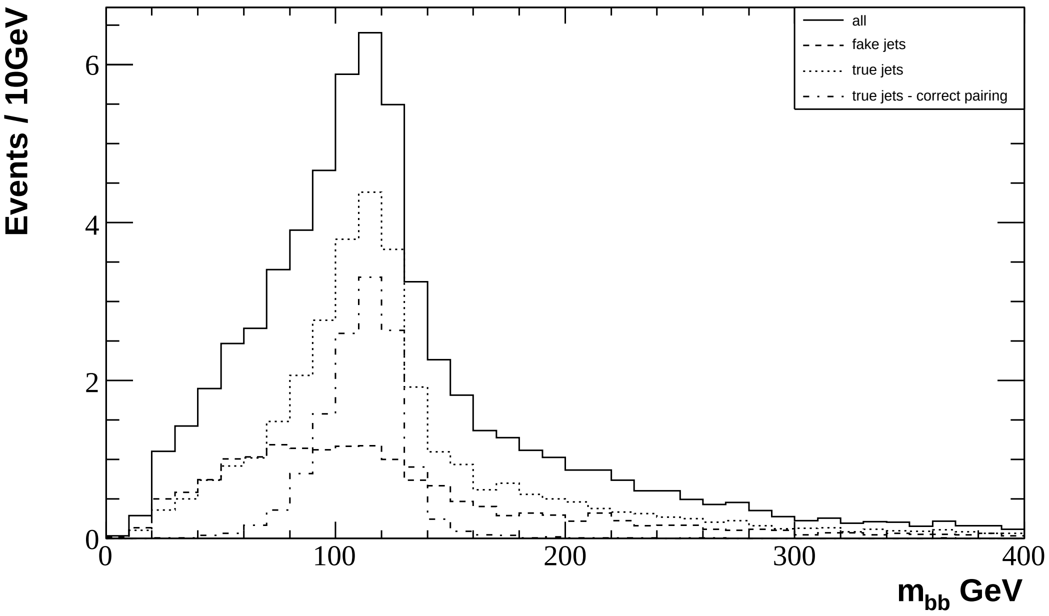

Figure 6.7: Distribution of the reconstructed Higgs boson mass, showing the individual contributions from events with one or more mis-tagged jets (fake jets), correctly tagged (and identified from the truth) jets (true jets) and those from the latter category where the correct jets are assigned to the Higgs boson decay (true jets - correct pairing).

from the truth record. For these events it is not possible to determine the correct assignment of jets to determine if the event was correctly reconstructed or not. 36.3% of the events left have incorrect flavour-tagging for one or more jets. More effective *b*-tagging is the only improvement that can be made here. Of the remaining events it is clear from figure 6.7 that improving the reconstruction procedure would result in a sharper mass peak and improved significance of the signal in this channel.

For the TDR analysis the combination of jets and W candidates that produced the second lowest Δ^2 value was also considered. It was found that in addition to the 26% of cases where the lowest Δ^2 resulted in the Higgs being reconstructed correctly, the second best combination also chose the correct jets for the Higgs 23% of the time. Half of this 23% however corresponds to the same jets for the Higgs as the best solution. Figure 6.8 shows the mass distributions for the cases where the combinations with the lowest or the second lowest Δ^2 values are the correct combinations. The right hand plot shows that the Higgs mass distribution could be improved if the second best combination could be chosen over the first. A more effective χ^2 quantity for use in the selection may be able to distinguish the correct pairing for events such as these.

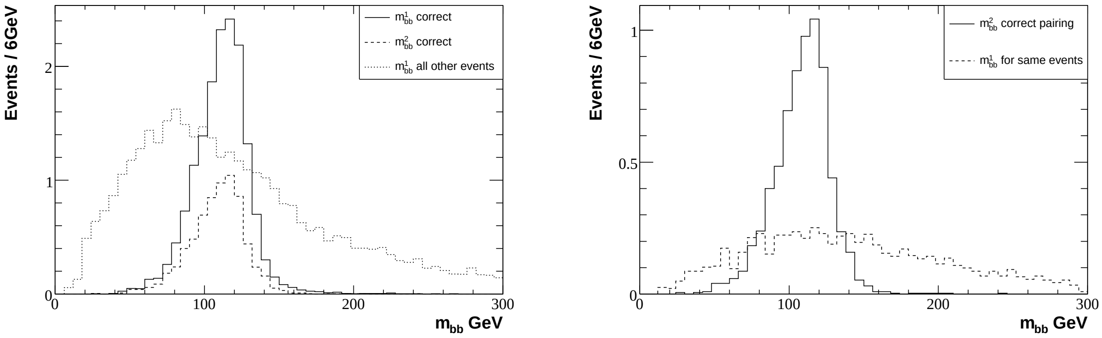

Figure 6.8: The histogram on the left shows the reconstructed Higgs boson mass distribution for the cases where (a) the correct jets were used in the reconstruction, (b) where the second lowest Δ^2 value produced the correct reconstruction and (c) the contribution to the distribution from all other events. The right hand plot shows the m_{bb} distributions from jet combinations with the lowest and second lowest Δ^2 values for events where the second was correct.

In the following sections possible improvements to all stages of the reconstruction process will be investigated, starting with the reconstruction of hadronic W candidates.

6.3 Hadronic W

To investigate the optimal way to reconstruct the hadronic W candidates, the decay products of the W were isolated and reconstructed separately from the rest of the event. This involves altering the output of the Monte Carlo generator before it is processed by Atlfast. The event record consists of a collection of interaction vertexes, with the associated incoming and outgoing particles connected to them. It is possible to navigate through the event to locate the W boson that decays hadronically, then copy all the daughter particles from this and all subsequent interactions to a new event record which can then be passed to Atlfast.

Two different algorithms were used to reconstruct jets in the events: the cone algorithm [43] and the $\mathrm{k_T}$ algorithm [52]. The cone algorithm starts from an initiator cell passing a certain $\mathrm{p_T}$ threshold, then combines all energy deposits within a cone of radius R to form a cluster. If the total $\mathrm{E_T}$ of the cluster exceeds a specified value it is accepted as a jet and the cells used are not considered for further clusters. The initiator cells are used in order of decreasing $\mathrm{p_T}$. The centre of the jet is the cluster barycentre calculated from the individual cells rather than the centre of the original cone. The $\mathrm{k_T}$ algorithm has a different approach, assigning cells to clusters based on energy-angle resolution variables. In this analysis the variables used are:

$$
\begin{aligned}
d_k &= p_{Tk}^2 R^2 \\
d_{kl} &= \min(p_{Tk}^2, p_{Tl}^2) R_{kl}^2 \\
\text{with } R_{kl}^2 &= (\eta_k - \eta_l)^2 + (\phi_k - \phi l)^2,
\end{aligned}
$$

where k is the cell in question, l represents other cells or clusters in the event and R is a dimensionless parameter that takes on a radius-like role in defining the extent of jets. The algorithm proceeds by finding the smallest value amongst the d_k and d_{kl} values. If d_{kl} is smaller than d_k the objects k and l are combined into a single cluster. Otherwise the object k is defined to be a jet and removed from the list of

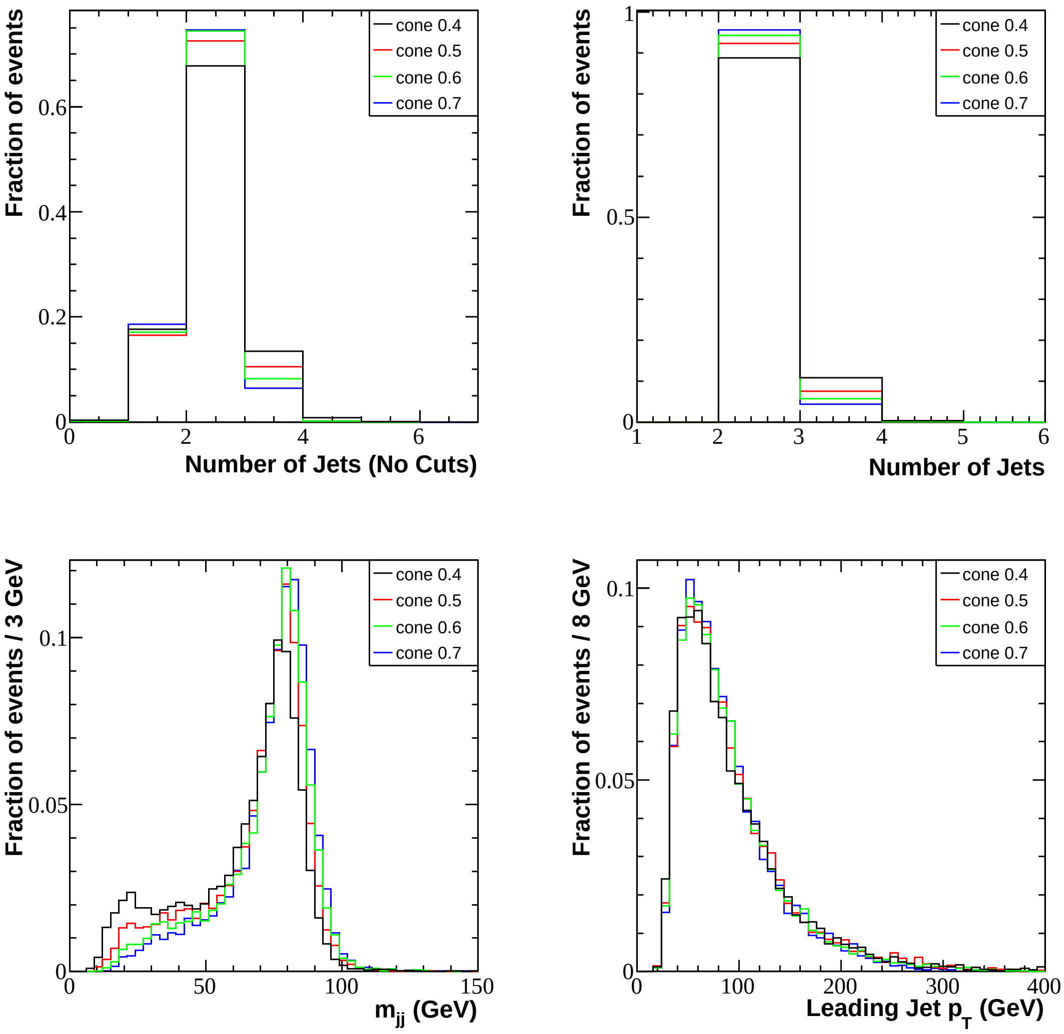

Figure 6.9: Comparison of the jets reconstructed from the W decay using the cone algorithm with four different R parameter settings. The top left hand plot shows the number of jets with $|\eta|<5$, the top right hand plot shows the number of jets with $p_T>20$GeV and $|\eta|<5$. The invariant mass distribution for all jet-pairs in the event is shown bottom left and the leading jet p_T bottom right.

objects to be merged. The algorithm continues until all energy deposits have been included in jets.

Figure 6.9 shows the output of the cone algorithm for R parameter values of 0.4, 0.5, 0.6 and 0.7. The pre-selection cuts (two jets from the W with $p_T>20$GeV) are applied in all of the plots except the bottom right. This plot shows the total number of jets reconstructed in the event; the minimum energy for a jet to be reconstructed

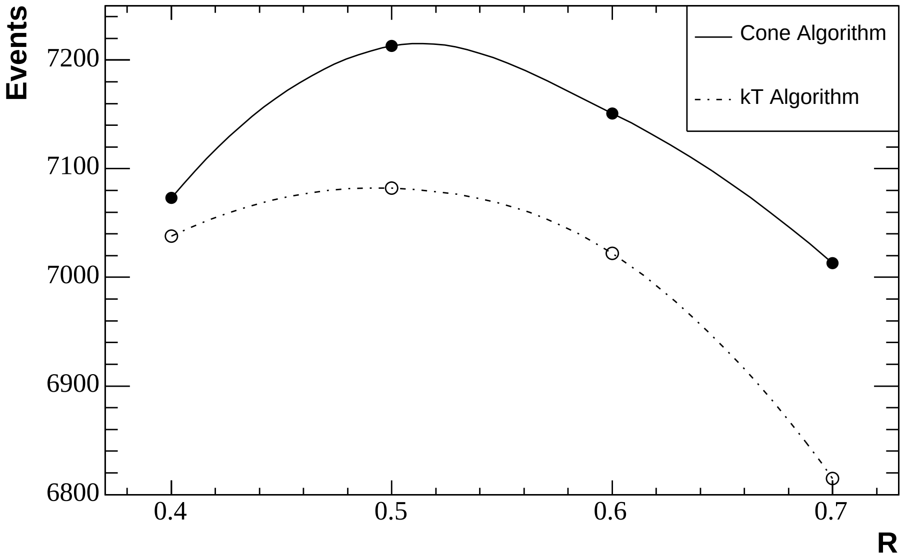

Figure 6.10: Comparison of the number of events with two or more jets (p_T>20GeV, $|\eta|$<5) reconstructed from the hadronically decaying W, for R parameters of 0.4, 0.5, 0.6 and 0.7 using the cone and k_T jet reconstruction algorithms.

by Atlfast is 15GeV within $|\eta|$<5. For all R values the fraction of events with only one jet reconstructed remains around the same level. For R=0.4 there is a noticeable increase in the number of events with three jets reconstructed, seen clearly as a peak at low masses in the top left plot. This plot shows the reconstructed invariant masses of all jet-pairs in the event.

Figure 6.10 shows the total number of events out of 100,000 passing the pre-selection cuts. The four data points from the cone algorithm and the distributions in figure 6.9 suggest that a cone size of R=0.5 would be more appropriate for reconstructing the W than a size of R=0.4. Similarly this indicates that a k_T R-parameter value of 0.5 would also be a good starting point for a comparison.

Table 6.6 shows the efficiencies of each stage of the full event analysis for the different jet algorithm configurations. In contrast to the findings above, these favour a cone size of 0.4. Both the cone with R=0.5 and the k_T algorithm have a lower number of events passing the requirement of four *b*-jets. The same is true of the other efficiencies: they are either similar or lower than for a cone of 0.4.

Cut	Cone R=0.4 (%)	Cone R=0.5 (%)	k_T R=0.5 (%)
$1l$ and 6 jets	47.7	46.6	46.5
4 b-jets	3.80 (8.0)	3.30 (7.08)	3.27 (7.02)
2 tops reconstructed	2.40 (63.6)	2.09 (63.3)	2.05 (62.8)
m_t inside mass window	1.95 (80.2)	1.65 (78.8)	1.64 (80.1)
m_{bb} inside mass window	0.90 (46.1)	0.76 (45.9)	0.77 (46.8)

Table 6.6: Efficiencies for each step of the analysis for signal events reconstructed using the cone algorithm with R parameters 0.4, 0.5 and the k_T algorithm with R parameter 0.5. The relative efficiencies with respect to the previous step are given in parenthesis.

The jet energy resolutions also favour a cone size of 0.4. This is due to the fact that the calibration used within Atlfast was produced for a cone of this size. Figure 6.11 shows the light- and b-jet resolutions for each of the above jet algorithm configurations. For light jets the default cone of 0.4 gives the optimal energy resolution (from the mean and RMS divided by the mean), whereas the 0.5 cone and k_T algorithm produce wider distributions peaked further above 1. For b-jets the 0.5 cone results in an energy distribution peaked closest to one. The 0.4 cone here underestimates the jet energy, but the width of the distribution is marginally narrower.

One possibility is to choose a cone size of 0.5 and recalibrate the jet energies. Another, which was studied here, is to look into combining three jets to make the hadronic W.

6.3.1 Three Jet Combinations

Using the sample of events where only the decay products of the W are present, it is possible to define two categories:

- Events where only two jets are reconstructed, both with p_T>20GeV.
- Events with greater than two jets reconstructed, two having p_T>20GeV.

Figure 6.12 shows the invariant mass of the two jet system. The solid line represents events that fall into the first category and the dashed line the second. In

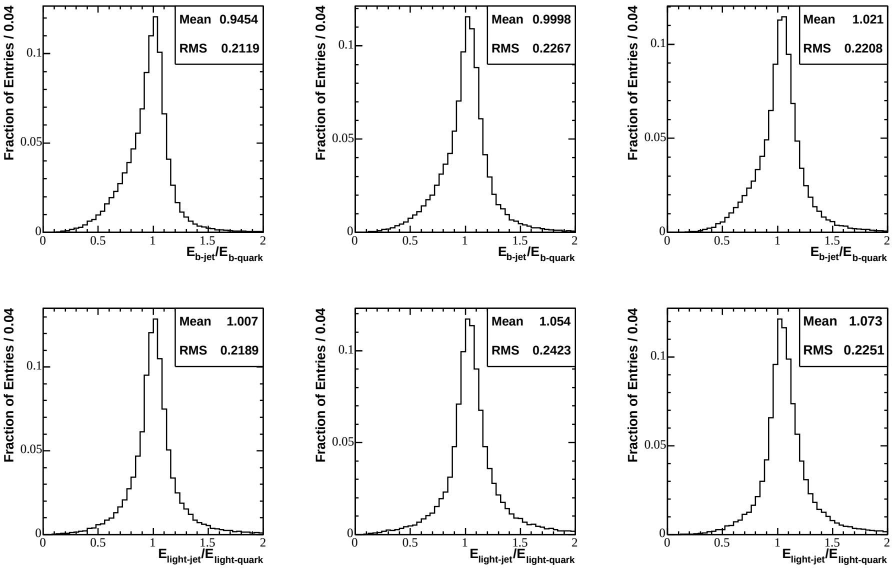

Figure 6.11: Jet energy divided by the Monte Carlo quark energy for b-tagged (top) and light jets (bottom). The plots on the left are for jets reconstructed using the cone algorithm with R=0.4 and the middle plots using a cone with R=0.5. The plots on the right were reconstructed using the $\mathrm{k_T}$ jet algorithm with an R parameter equal to 0.5.

the case of three jets, the invariant mass of the two jets that is closest to the W mass is displayed. The solid histogram is roughly Gaussian about the W mass of 80.4GeV but has a long tail to low masses.

The peak in the dashed distribution is around 65GeV. If we could incorporate the third jet into the reconstructed W, it may improve the W energy and direction, possibly improving the efficiency of the minimisation procedure to choose the correct jets for the top-quarks. Figure 6.13a shows the distance between the closest two jets of the three in terms of ΔR. The distribution peaks at 0.5, and in 88% of cases is less than 1. A two dimensional plot of this quantity versus the mass of the two jet invariant mass can be seen in Figure 6.13b. This plot shows that for the majority of cases where an extra jet is reconstructed, the extra jet is within a small ΔR of one of the jets and the effect on the invariant mass of the pair of more energetic jets in the event is of the order of 10-15GeV. At lower m_{jj} values, the spread in ΔR is a lot larger, indicating a much harder gluon emission and hence a larger angle between the outgoing quark and radiated gluon which go on to form the two jets.

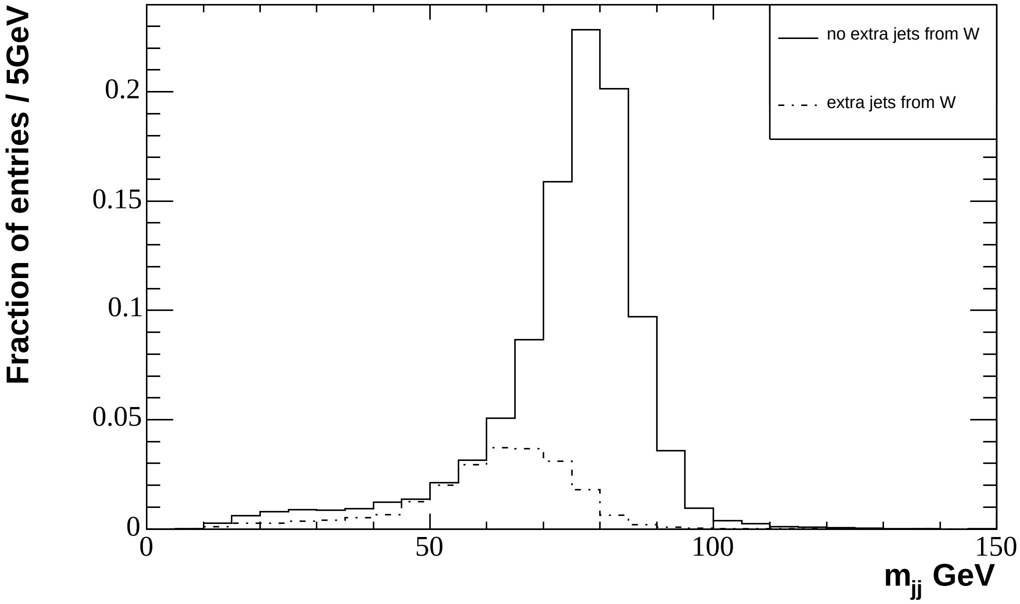

Figure 6.12: Distribution of the reconstructed jet-pair masses for events with only two jets from the W decay (solid line) and events with more than two jets (dashed line). Only the jet pair with m_{jj} closest to the W mass is included per event.

Three jet combinations are made in the case of an extra jet being within $\Delta R < 1$ of either of the two jets in the jet pair. Figure 6.14a shows the difference in ΔR between the W reconstructed with two jets and the true W, minus the ΔR value between the W reconstructed with three jets and the true W. From this plot it is clear that the jet direction obtained from incorporating three jets is closer to the true W in the majority of cases. Figure 6.14b shows the resolution of the reconstructed W energy. The distribution is a lot narrower when three jets are incorporated into the W, however the mean of the distribution is shifted above one.

The ability to create W candidates from three jets is next introduced into the full event analysis. This is done as follows: for each pair of light-jets, the closest jet to either of the two jets is found from the collection of all light-jets (not just those passing the pre-selection cuts). If this jet is within a ΔR of 0.8 and the invariant mass of the two jet system is less than 75GeV, a W candidate from the three jets is considered. Out of the two W candidates (the initial two jet or the

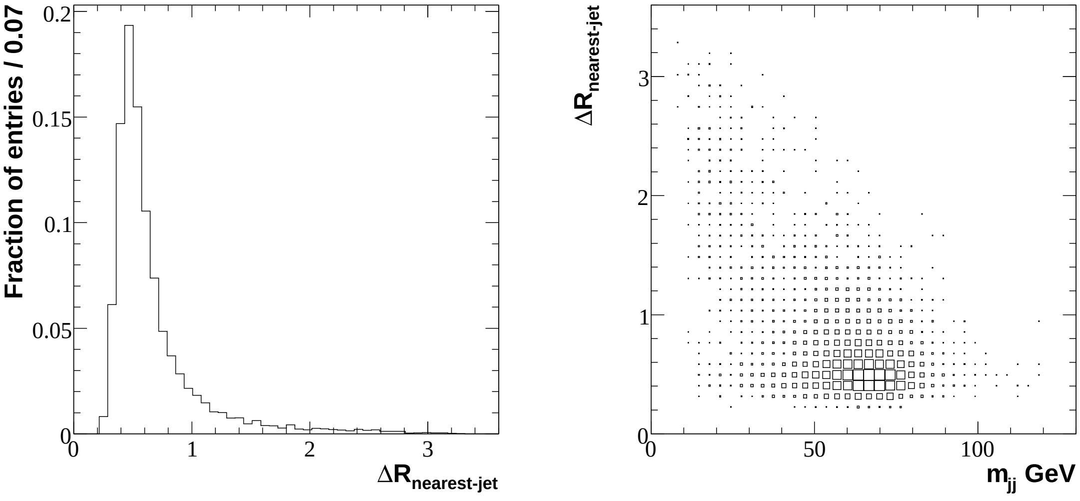

Figure 6.13: (a) The distance, ΔR, between the two closest jets for the case where three jets are reconstructed from the W decay. (b) A two dimensional plot of the distance, ΔR, to the nearest jet and the invariant mass of the jet-pair.

new three jet system), the candidate that is closest to the W mass is kept. This affects approximately 12% of events passing the preselection cuts for the W. The addition of this method into the full event analysis, results in only a slight increase in the number of events passing the cuts. The efficiency for the signal increases from 0.90 to 0.92, however the number of background events passing the cuts also increases resulting in only a small improvement in significance from 1.78 to 1.80. The statistical error on all the significances presented in this chapter are of the order of 0.02, however since the data sample used to study the effect of the changes remains the same, the resulting effects can be classified as improvements. The largest effect is on the $t\bar{t}jj$ background which sees an increase of 6% for events retained after the Higgs mass window cut. For signal events and the $t\bar{t}b\bar{b}$ backgrounds this value is around 3%. For events where the jets can be matched to the truth data, and where the jets are correctly tagged, the number of signal events with the Higgs correctly reconstructed increases slightly from 63.9 to 64.2%.

Figure 6.15 shows the reconstructed top-quark distributions. With the three jet reconstruction the width of the hadronic top distribution decreases from $\sigma = 7.1$ to

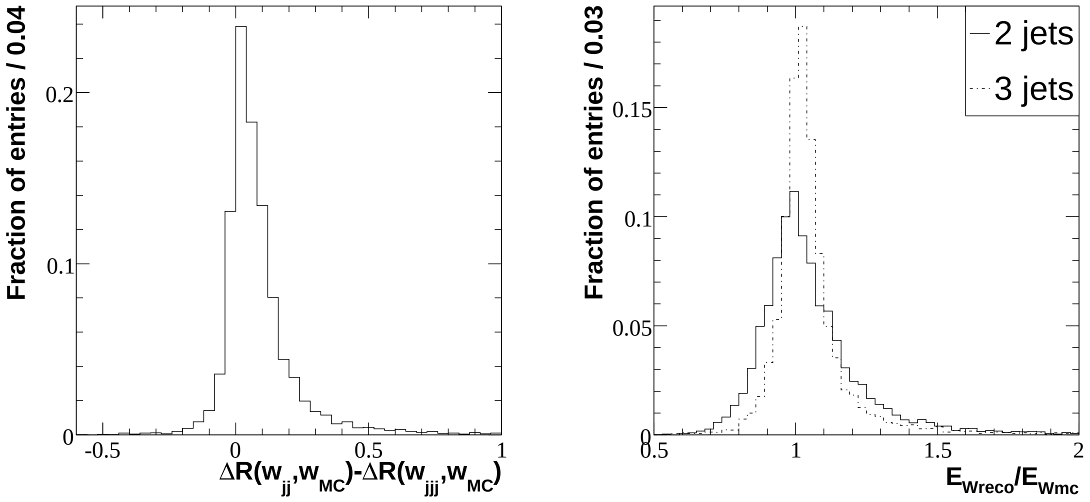

Figure 6.14: (a) The difference between the ΔR values between the true W and the W candidate reconstructed from two and three jets. (b) Reconstructed W energy divided by the true W energy, shown for candidates produced using 2 jets (solid line) and three jets (dashed line).

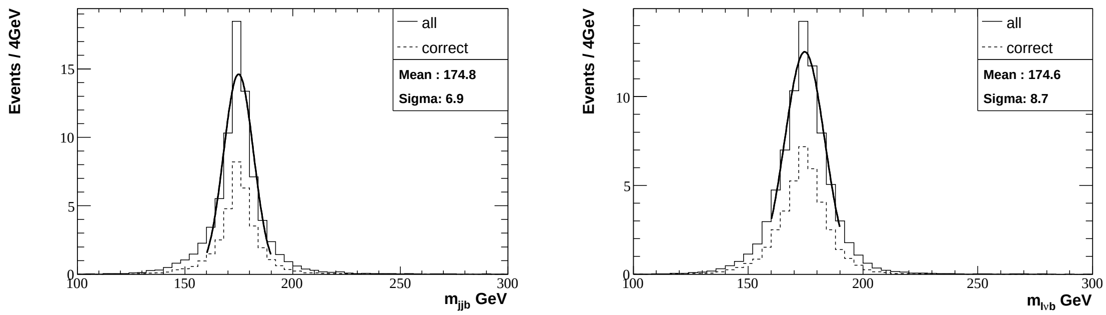

Figure 6.15: Distribution of m_{jjb} (left) and $m_{l\nu b}$ (right) for reconstructed top-quarks. The dashed histogram represents correctly reconstructed top-quarks. The histograms are normalised to the rate of expected events for L=30fb^{-1}.

$\sigma = 6.9$.

6.3.2 W Rescaling

In the TDR analysis the energy rescaling is carried out such that the rescaled W candidate mass, m$_{jj}$, equals m$_W$, using a single rescaling factor. Figure 6.16 shows the energy resolution of the reconstructed W before and after rescaling, for the case where the jets are known to be from the true W. The energy distribution after rescaling is peaked closer to one than before, however a tail to higher energies has been created.

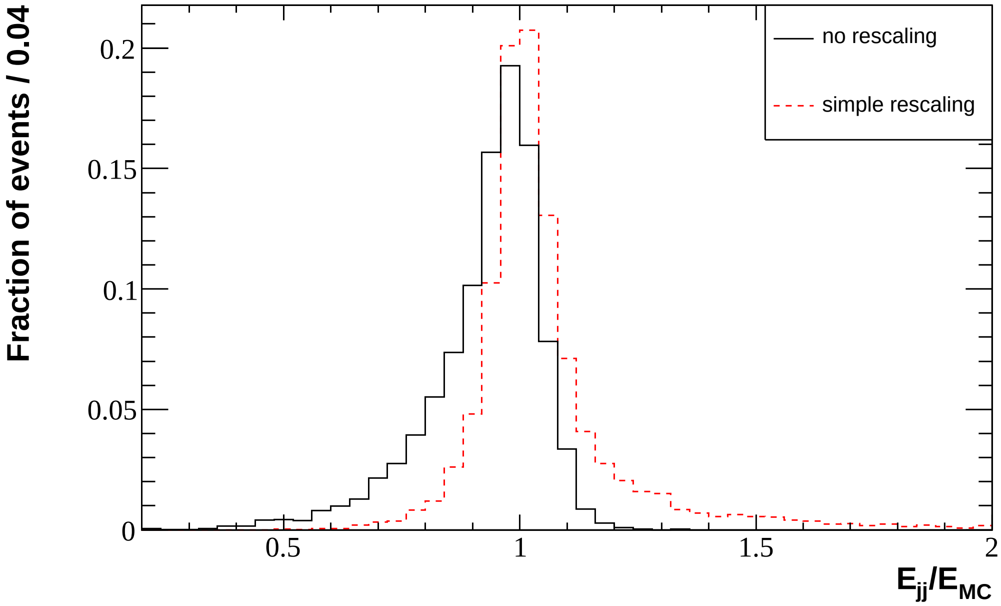

Figure 6.16: Reconstructed W energy divided by the true W energy, before (black line) and after (red line) rescaling to the W mass.

Uncertainties on the energy of the jets can be calculated from the calorimeter resolution, using the formulae given in equation 6.3.

$$\begin{aligned} \frac{\sigma_E}{E} &= \frac{0.5}{\sqrt{E(\mathrm{GeV})}} \oplus 0.03 \quad |\eta| < 3.2 \\ \frac{\sigma_E}{E} &= \frac{1.0}{\sqrt{E(\mathrm{GeV})}} \oplus 0.07 \quad |\eta| > 3.2 \end{aligned} \tag{6.3}$$

Since the relative uncertainty on the energy decreases as the energy of the jet increases, it could be useful to use this in the jet rescaling. More energetic jets with a lower relative uncertainty should be rescaled less than lower energy jets. Two alternative methods of rescaling were implemented: the first, equation 6.4, is a simple rescaling method using the jet energy uncertainties to calculate a separate rescaling factor for each jet; and the second is a method based on a minimisation of equation 6.5 using Minuit [53]. This method is used in the ATLAS top analysis [54].

$$\begin{aligned} E_{jet1} &\rightarrow E'_{jet1} = E_{jet1} + \alpha\sigma_{jet1} \\ E_{jet2} &\rightarrow E'_{jet2} = E_{jet2} + \alpha\sigma_{jet2} \end{aligned} \tag{6.4}$$

$$\chi^2 = \frac{(m_{jj} - m_W)^2}{\Gamma_W^2} + \left(\frac{E_{jet1}(1-\alpha_1)}{\sigma_{jet1}}\right)^2 + \left(\frac{E_{jet2}(1-\alpha_2)}{\sigma_{jet2}}\right)^2 \tag{6.5}$$

The result of the three rescaling methods on the reconstructed W energy is shown in Figure 6.17. The proportional rescaling method results in only a very small improvement over the simple rescaling method: the mean and width of the Gaussian distribution are reduced, however overall the distribution remains the same shape with a large tail to high energies. The χ^2 based Minuit rescaling eliminates these tails and also improves the mean and width of the Gaussian even further.

The effect of the Minuit rescaling on the TDR analysis is a slight drop in the number of events passing the cuts. This is around a 1% decrease for signal and $t\bar{t}b\bar{b}$ events, but is significantly larger for $t\bar{t}jj$ events resulting in a 9% decrease. As seen previously, this background has the greatest sensitivity to the hadronic W mass cut, indicating a larger number of events with only fake W candidates present. These events are effected by the rescaling such that the reconstructed tops no longer pass the mass cuts. The efficiency of the top mass cut for the $t\bar{t}jj$ background is reduced from 69% to 66% by use of this method. Overall this results in a small significance increase from 1.78 to 1.79.

Correcting the $\not{E}_{\mathrm{T}}$ for the changes in the jet energy due to the rescaling resulted in the resolution degrading slightly. All calorimeter deposits are used in the calculation of $\not{E}_{\mathrm{T}}$, not just those used in jets. The rescaling is most likely to be correcting for energy not included in the reconstructed jet by the jet algorithm rather than, to any large extent, energy not recorded by the calorimeter.

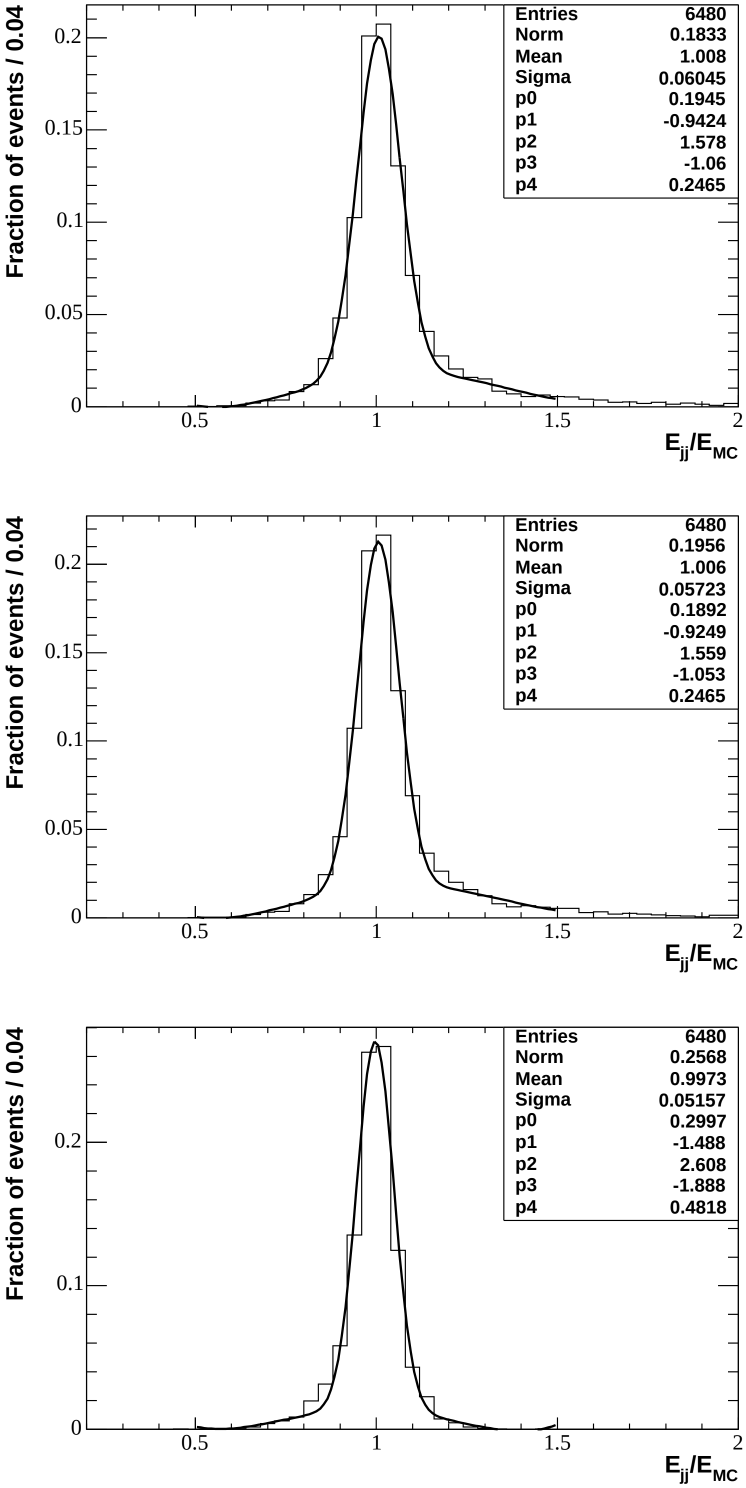

Figure 6.17: Reconstructed W energy divided by the true W energy for simple rescaling (top), the rescaling method shown in equation 6.4 (middle) and the Minuit based rescaling (bottom). Distributions have been fitted with a Gaussian plus fourth order polynomial. The fit results consist of the mean and sigma of the Gaussian part of the fitted function and p0 to p4 which are the polynomial coefficients in order from the lowest to the highest term.

6.4 Correcting for Semi-leptonic *b*-decays

In 21% of cases a *b*-hadron will decay to a lepton, an *e*- or μ-neutrino and a charm-quark. In these cases the *b*-jet recorded by the detector will be significantly lower in energy than the initial *b*-quark, due to the energy carried by the neutrino escaping the detector. For 14% of *b*-jets it is possible to locate an electron ($\mathrm{p_T} > 5\mathrm{GeV}$) or muon ($\mathrm{p_T} > 6\mathrm{GeV}$) within the jet cone. Figure 6.18a shows the energy resolution of *b*-jets where a lepton cannot be found within the jet cone. Figure 6.18b shows the energy resolution where a lepton is present within the cone.

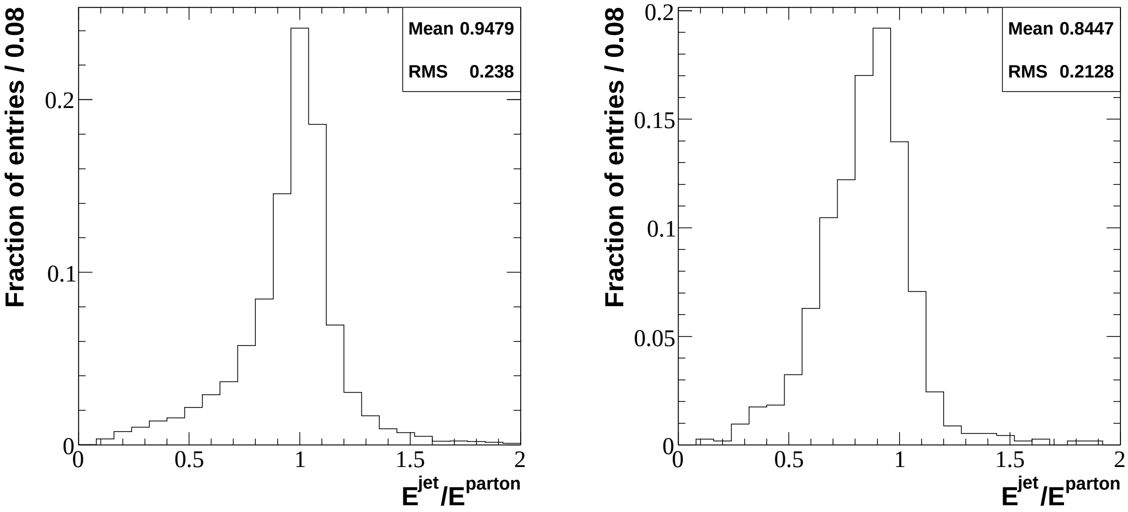

Figure 6.18: (a) Energy resolution for *b*-jets without a lepton located within the jet cone. (b) Energy resolution for *b*-jets with a lepton found within the jet cone.

Table 6.7 shows the correlations between the neutrino energy and the lepton and jet energies. While the lepton and neutrino have very little correlation between their energies, there is more correlation between the neutrino and reconstructed jet energy. An attempt to correct for the energy lost from the jet due to the neutrino was made using both a fixed correction factor and one with a small dependence on the $\mathrm{E_T}$ of the jet. A corresponding correction to the event $\not{E}_\mathrm{T}$ was also made.

Figure 6.19 shows the *b*-jet energy resolutions before and after correction. The constant correction factor performs the best out of the two increasing the mean of

Variables		Correlation
E_{ν_e}	E_{jet}	0.33
E_{ν_e}	E_e	0.09
E_{ν_μ}	E_{jet}	0.43
E_{ν_μ}	E_μ	0.11

Table 6.7: Correlations between energy variables for b-jets with a lepton found within the jet cone.

the distribution from 0.95 to 1.01, yet this is at the expense of a large number of jets where the jet energy is greatly overestimated, as can be seen by the larger RMS value.

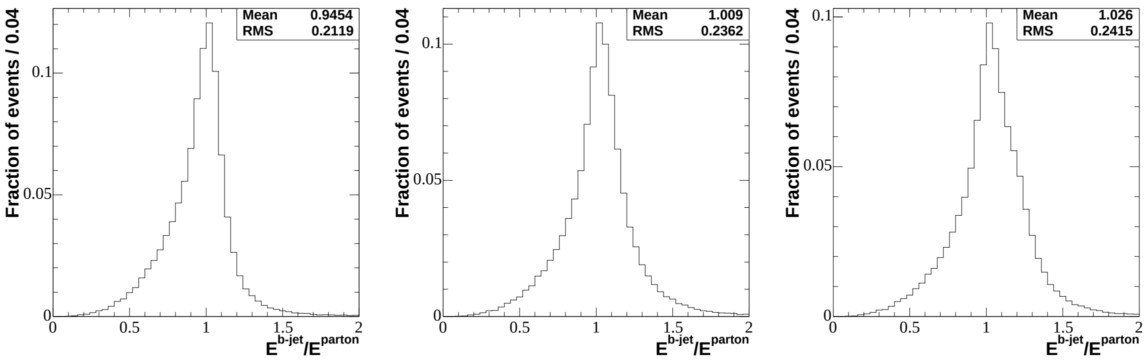

(a) (b) (c)

Figure 6.19: Comparison of the b-jet energy resolutions for (a) no correction, (b) constant correction and (c) p_T dependant correction.

Figure 6.20 shows the reconstructed Higgs mass distributions for signal events where $m_H = 120$GeV. The mean of the distribution has improved for both of the methods of correction, increasing from 111GeV to 119GeV when using the constant factor and 111GeV to 121GeV for the p_T dependant factor. This again is accompanied by an increase in the width of the distribution and a decrease in the number of events being reconstructed. The effect on the reconstructed hadronic top-quark mass distribution follows the same trend (shown in figure 6.21). One exception is the semi-leptonic top mass (figure 6.22), where the constant correction produces a distribution with a slightly narrower peak. Although there was little difference in the $\not{p}_T$ component distributions with and without the corrections, this suggests that the neutrino reconstruction could have been improved by this method.

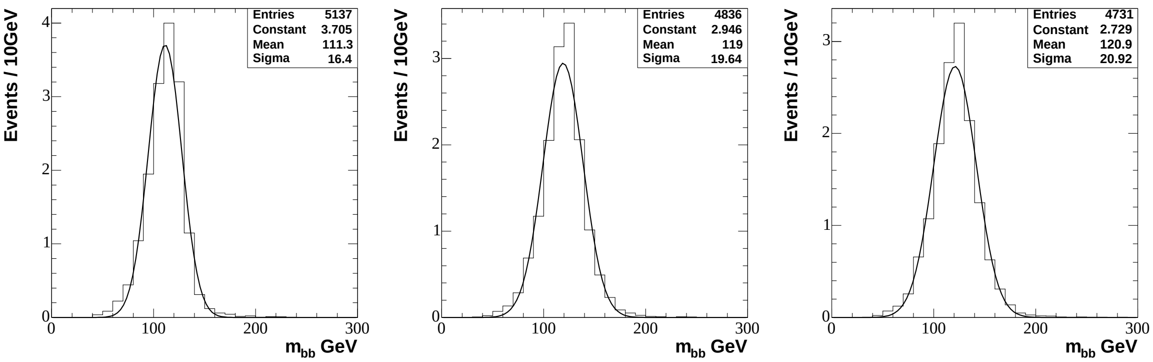

(a) (b) (c)

Figure 6.20: Comparison of the Higgs mass distributions for (a) no correction, (b) constant correction and (c) p_T dependant correction.

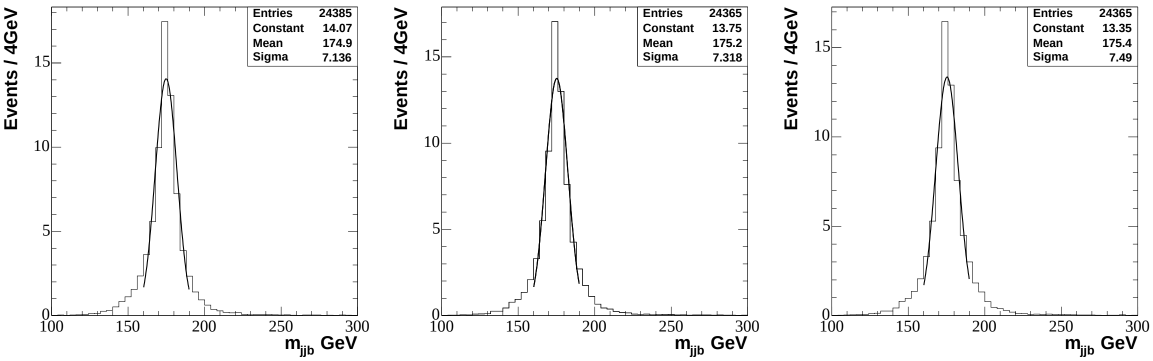

(a) (b) (c)

Figure 6.21: Comparison of the m_{jjb} distributions for (a) no correction, (b) constant correction and (c) p_T dependant correction.

An efficiency of 0.5 for non-isolated lepton reconstruction was added to the full event analysis and results obtained using a constant correction factor. The effect of this was a drop in the number of events from both the signal and background. The effect was most noticeable in the signal with a reduction of 5% compared to 2% in the $t\bar{t}b\bar{b}$ and 3% in the $t\bar{t}jj$ backgrounds. Although the mean of the Higgs mass distribution was improved, the effects on the analysis of this change are predominantly negative, seen as an overall reduction in the significance of the channel to 1.72.

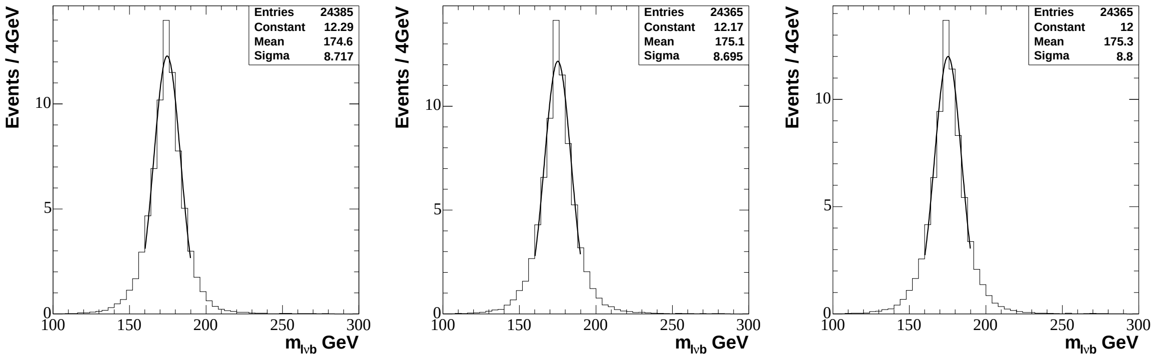

(a) (b) (c)

Figure 6.22: Comparison of the $m_{l\nu b}$ distributions for (a) no correction, (b) constant correction and (c) $\mathrm{p_T}$ dependant correction.

6.5 Top Reconstruction

Reconstruction of the two top-quarks is the main step in the analysis. In study [51] of the channel, the use of a likelihood function to choose the jet pairings for the top-quarks was investigated. In this section a χ^2 quantity is constructed to perform the minimisation. This is followed by an investigation of the benefits of the use of a likelihood function over this.

6.5.1 χ^2 Variable for Jet Pairings

To improve the top-quark reconstruction an alternative to the minimisation parameter Δ^2 (equation 6.2) was constructed.

$$\chi^2 = \frac{(m_{l\nu b} - m_t)^2}{\sigma^2_{l\nu b}} + \frac{(m_{jjb} - m_t)^2}{\sigma^2_{jjb}} + \frac{(m_{jj} - m_W)^2}{\sigma^2_{jj}} \tag{6.6}$$

The χ^2 quantity (equation 6.6) has three contributions. The first is from the reconstructed semi-leptonic top-quark, the second from the hadronic top-quark using the rescaled W boson as input and the final contribution is from the W before rescaling. The χ^2 incorporates uncertainties on the jet energies as calculated from equation 6.3. The lepton energy error in the case of an electron is given by equation 6.7. In the case of a muon the error is determined from a parametrisation, details of which are given in [55].

$$
\begin{aligned}
\frac{\sigma_E}{E} &= \frac{0.245}{p_T(\mathrm{GeV})} \oplus \frac{0.12}{\sqrt{E(\mathrm{GeV})}} \oplus 0.007 & |\eta| < 1.4 \\
\frac{\sigma_E}{E} &= \frac{0.306(2.4-|\eta|+0.228)}{E(\mathrm{GeV})} \oplus \frac{0.12}{\sqrt{E(\mathrm{GeV})}} \oplus 0.007 & |\eta| > 1.4
\end{aligned}
\tag{6.7}
$$

Residual plots for each of the three contributions can be seen in Figure 6.23. The RMS values for the hadronic and leptonic top-quarks suggest that the uncertainty on the masses have been underestimated, in contrast to the hadronic W where the uncertainties have been overestimated. For jets, the uncertainty on the energy used is based on the expected calorimeter resolution. This does not account for uncertainties introduced by the jet reconstruction, which will differ between light- and *b*-jets. *b*-jets tend to be wider, resulting in a worse energy resolution using a cone of 0.4 than that for light-jets. Regarding the difference in underestimation between the hadronic and leptonic top-quarks despite them both including uncertainties from one *b*-jet, this could be due to the rescaling of the jet energies from the hadronic W.

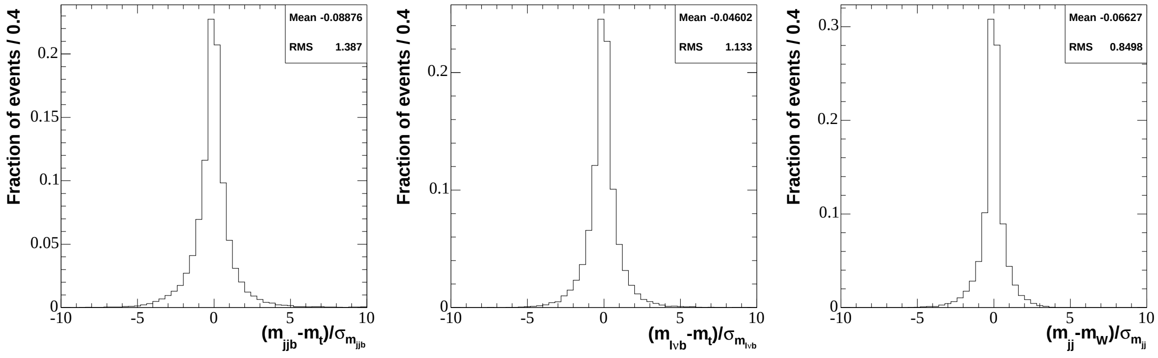

(a) (b) (c)

Figure 6.23: Residual plots for the three contributions to the χ^2 function.

Figure 6.24 shows the effect on the top mass of using the χ^2 for the minimisation. The mass distributions for the reconstructed tops are less biased toward the nominal top mass. The cut on the reconstructed top mass in this case has a lower efficiency, reducing the final number of events and significance of the channel from 1.78 in the TDR analysis to 1.73.

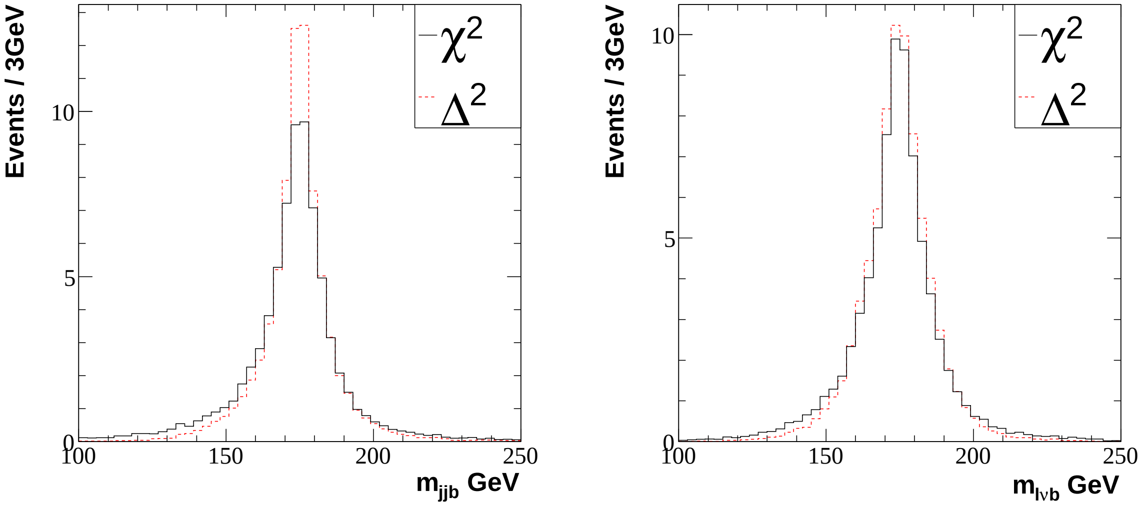

Figure 6.24: Distribution of m_{jjb} (left) and $m_{l\nu b}$ (right) for reconstructed top-quarks. The dashed histogram represents top-quarks reconstructed using the Δ^2 function and the solid line using the χ^2 function. Histograms are normalised to the rate of expected events for L=30fb^{-1}.

Instead of using a cut on the top mass, a cut on the χ^2 value will be used. Figure 6.25a displays the dependence of the overall significance of the channel on the χ^2 cut value. From this plot the optimal value of the cut is twenty. The percentage of correctly reconstructed signal events in the final mass window has little dependence on the choice of this cut, as can be seen in figure 6.25b.

Since the χ^2 quantity includes a contribution from the hadronically decaying W candidate, the mass cut on the W candidates was removed. Relaxing the cut completely whilst using a cut of fifteen on the top-quark χ^2 had the effect of slightly reducing the significance of the channel. The number of signal events being reconstructed within the Higgs mass window rose by 13%, however the effect of the number of background events was significantly larger, most notably the $t\bar{t}jj$ background which increased by 44%. Since the χ^2 contribution of the W is included in the top χ^2, the W mass cut was not replaced by a corresponding χ^2 cut.

The combined changes discussed so far (without the correction for semi-leptonic b-hadron decays) result in an increase in significance for the channel from 1.78 for the TDR method to 1.90, and an increase in the percentage of correctly reconstructed

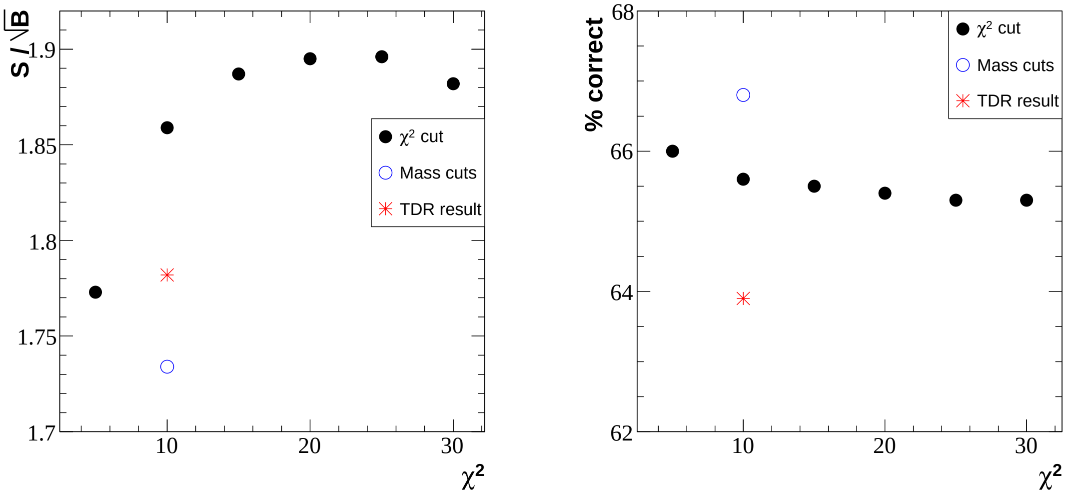

Figure 6.25: (a) A plot of significance versus the value of the χ^2 cut used. The significance when using the TDR Δ^2 method is shown, along with the significance obtained using the χ^2 minimisation with a cut on the mass of the reconstructed top-quarks. (b) Plot of the percentage of correctly reconstructed Higgs decays in the Higgs mass window versus the cut on χ^2 used for events that are correctly matched and tagged.

events within the Higgs mass window from 63.9% to 65.7%. Table 6.8 shows the efficiency of each stage of the analysis for the signal and backgrounds. The signal reconstruction efficiency has risen from 0.90% to 1.12%, an increase of 24%. The corresponding increase seen in the backgrounds is 36% for the $t\bar{t}b\bar{b}$ (EW), 38% for the $t\bar{t}b\bar{b}$ (QCD) and 50% for the $t\bar{t}jj$ background. Table 6.9 displays the total number of events from each background after each set of cuts. The number of signal events reconstructed for a 120GeV Higgs boson with an integrated luminosity of 30fb^{-1} has increased from 27.9 to 34.9. Plots of the reconstructed Higgs mass distributions for the signal, $t\bar{t}b\bar{b}$ and $t\bar{t}jj$ backgrounds are shown in figure 6.27. The shape of the distributions remain the same, with increased event numbers in the range $m_{bb} <$ 200GeV. The reconstructed top distributions are shown in figure 6.26. An increased number of events in the tails of the distribution can be seen for both top-quarks.

Looking again at the second best jet pairing in the event, the percentage of events where this is correct and the chosen pairing is not has reduced from 12% to 9%. This is accompanied by an increase in the number of events where the first

Cut	$t\bar{t}H^0$ (120) (%)	$t\bar{t}b\bar{b}$ (QCD) (%)	$t\bar{t}jj$ (%)	$t\bar{t}b\bar{b}$ (EW) (%)
1l and 6 jets	47.7	39.9	21.7	37.8
4 b-jets	3.8 (8.0)	1.5 (3.8)	0.019 (0.09)	1.6 (4.2)
2 tops reconstructed	2.5 (64.5)	0.98 (64.0)	0.010 (54.4)	1.1 (63.6)
$\chi^2 < 20$	2.36 (95.3)	0.93 (94.7)	0.009 (89.1)	0.96 (95.0)
m$_{bb}$ inside mass window	1.12 (47.6)	0.25 (26.5)	0.003 (33.4)	0.30 (31.6)

Table 6.8: Efficiencies for each step of the analysis. The relative efficiencies with respect to the previous step are given in parenthesis.

Cut	$t\bar{t}H^0$ (120)	$t\bar{t}b\bar{b}$ (QCD)	$t\bar{t}jj$	$t\bar{t}b\bar{b}$ (EW)	ΣBkg
1l and 6 jets	1480	30036	895855	2936	928827
4 b-jets	119	1152	771	123	2046
2 tops reconstructed	76.8	737.5	426.0	78.0	1241.6
$\chi^2 < 20$	73.2	698.3	379.8	74.2	1152.2
m$_{bb}$ inside mass window	34.9	185.3	127.2	23.4	335.9

Table 6.9: Expected signal and background events after each stage of the analysis for L=30fb^{-1}.

pairing is correct from 26% to 28%. The χ^2 method with the accompanying changes for the hadronic W reconstruction is able to better discriminate between incorrect and correct jet pairings but the majority of the improvement in significance is due to the replacement of the top mass cut with the χ^2 cut.

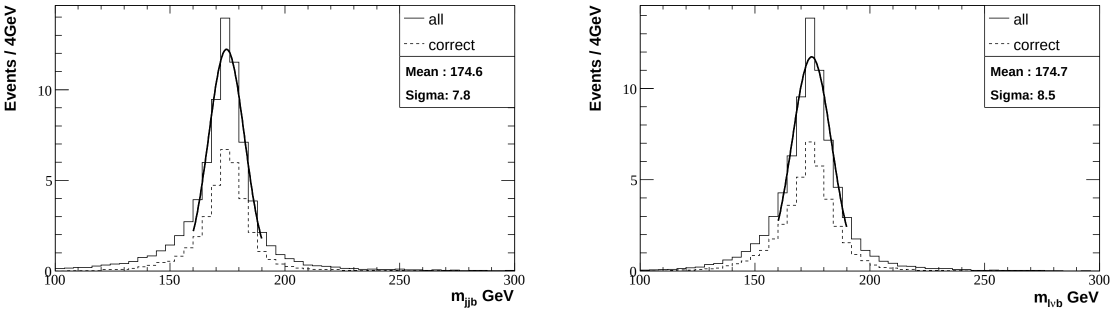

Figure 6.26: Distribution of m_{jjb} (left) and $m_{l\nu b}$ (right) for reconstructed top-quarks. The dashed histogram represents correctly reconstructed top-quarks. The histograms are normalised to the rate of expected events for L=30fb^{-1}.

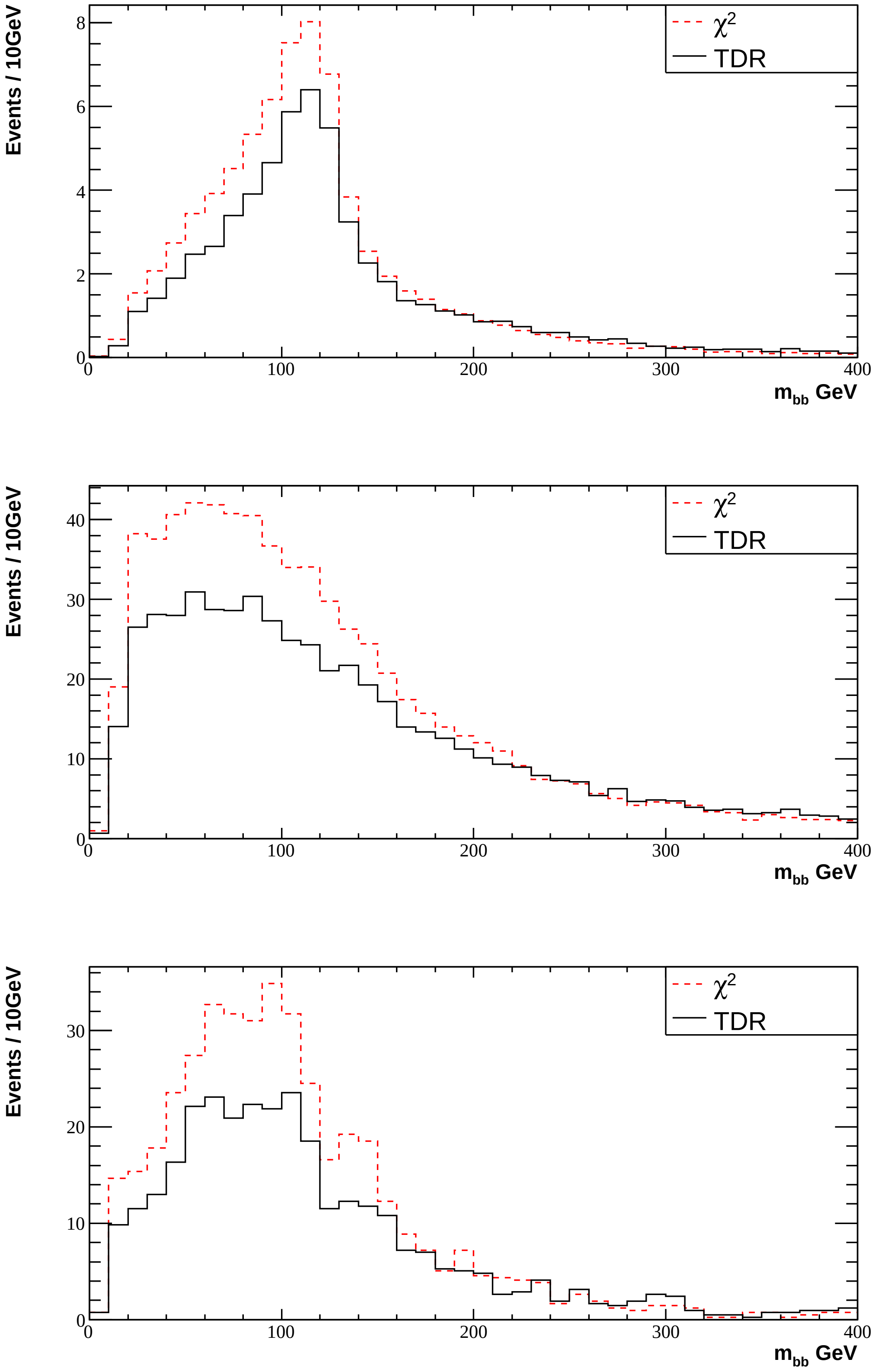

Figure 6.27: Reconstructed Higgs mass distributions for $t\bar{t}H^0$ events (top), $t\bar{t}b\bar{b}$ events (middle) and $t\bar{t}jj$ events (bottom). The red/dashed histogram displays the results from the updated χ^2 method. The black/solid histogram displays the results from the TDR method.

6.5.2 Neutrino Reconstruction with 'Collinear Approximation'

Before reconstructing the top-quarks, 25% of events passing the pre-selection cuts are lost at the stage of calculating solutions for the neutrino four-momentum. Use of a technique to retain these events was proposed in [51]. When no solution can be found there has been a significant mis-measurement of the $\not{p}_{\mathrm{T}}$ in the event. By assuming that the neutrino has the same p_z as the lepton ('collinear approximation'), a four-vector for the neutrino can be constructed using $\not{p}_{\mathrm{x}}$, $\not{p}_{\mathrm{y}}$, and p_z^l then rescaled to the W mass. It was shown in [51] that this assumption results in only a small degradation of the resolution of the semi-leptonic top-quark mass. Applying this to the results of the previous section leads to an increase in signal events of 30% and an increase in significance from 1.90 to 2.19.

6.5.3 Likelihood Method

Another improvement to the TDR method proposed in [51] is the use of a likelihood function for the top-quark reconstruction. An introduction to the likelihood technique is given in appendix A. Figure 6.28 displays the variables chosen in [51] to construct the likelihood function. These include the mass of the top-quarks and the hadronic W candidate, but also use the angles and distances between the jets in the W, and the W and jet in the reconstructed top-quarks. An explanation of these variables as well as additional variables which could also be useful in constructing a likelihood function are given below. Distributions for these variables are shown in figures 6.28 and 6.29.

m_{jj}: The invariant mass of the pair of light jets from the hadronic W decay.

m_{jjb}: The invariant mass of the two light jets and one b-jet from the hadronic top decay.

$m_{l\nu b}$: The invariant mass of the lepton, reconstructed neutrino and b-jet from the semi-leptonic top decay.

$\Delta R(b, jj)$: The distance in R between the reconstructed hadronic W and the b-jet from the same top-quark.

$\Delta R(b, l)$: The distance in R between the lepton and the b-jet from the same top-quark.

$< (j, j)$: The angle between the two light jets from the hadronic W decay.

$\Delta\phi(t, t)$: The difference in ϕ between the two reconstructed top-quarks.

$< (b, b)$: The angle between the two b-jets assumed to originate from the Higgs boson.

$p_T^{t1} + p_T^{t2}$: The sum of the p_T of the reconstructed top-quarks.

ln χ^2: The natural log of the variable χ^2 as defined in equation 6.6.

An interesting feature was observed in the incorrect mass distribution of the semi-leptonic top-quark. When creating these distributions and applying the likelihood technique a single neutrino solution is chosen. In study [51] the solution which minimises $|m_{l\nu b} - m_t|$ is chosen. When creating the reference distributions, a check on the jet incorporated into the semi-leptonic top-quark was made, but not a check on the neutrino solution. In figure 6.30 a peak can be seen at the top mass in the incorrect histogram. This could clearly represent a problem in a number of events, as the incorrect jet and incorrect neutrino solution combine to produce a mass closer to the top mass than the correct pairing. The second histogram in figure 6.30 and the corresponding one in figure 6.28 show the distribution for $m_{l\nu b}$ where the neutrino solution with the lowest p_z is chosen. Here the peak in the combinatorial background is no longer present but the width of the correct distribution in the peak is much

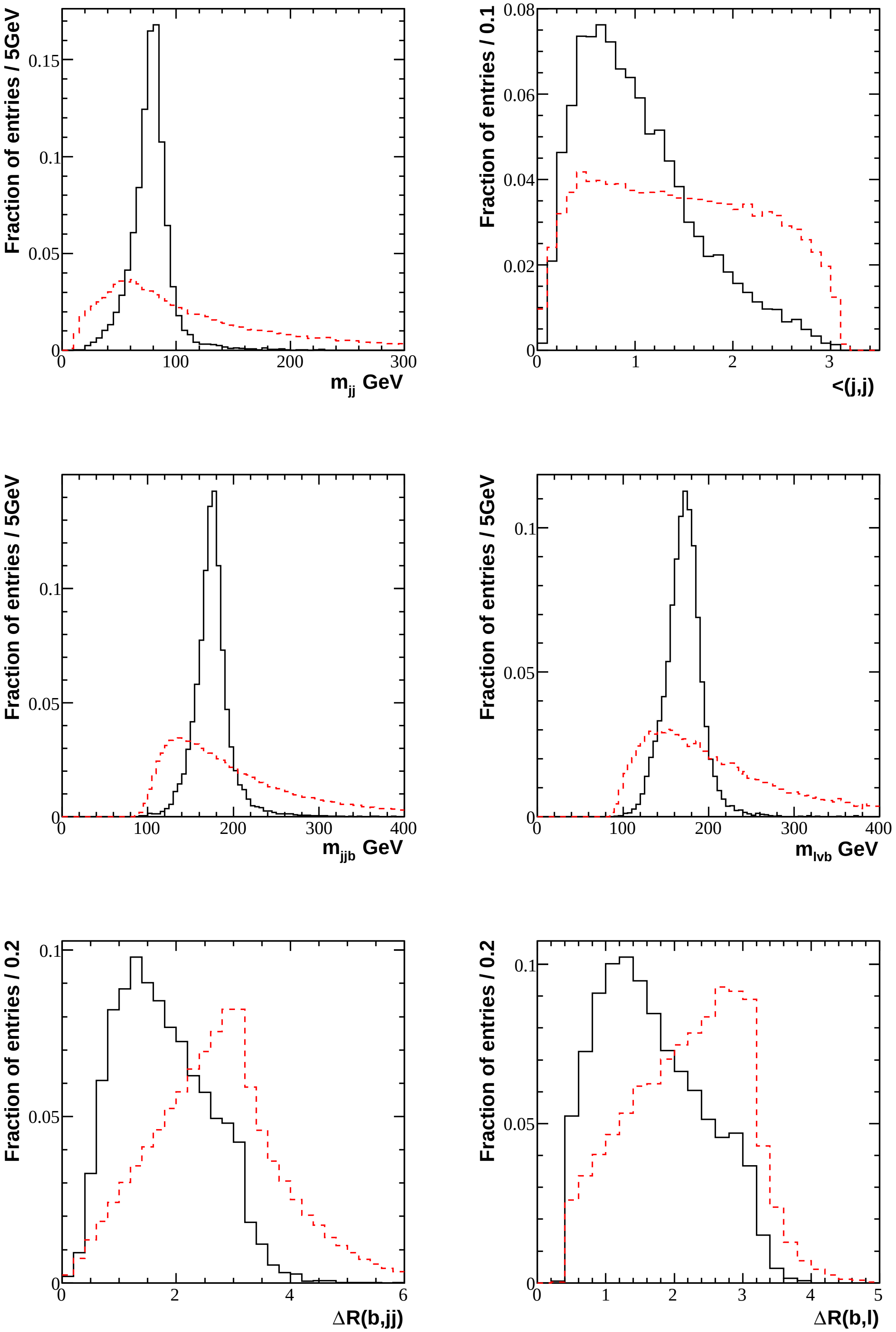

Figure 6.28: Histograms showing the likelihood variables used in the study [51] for correct (black/solid) and incorrect (red/dashed) jet combinations. All distributions are normalised to unit area.

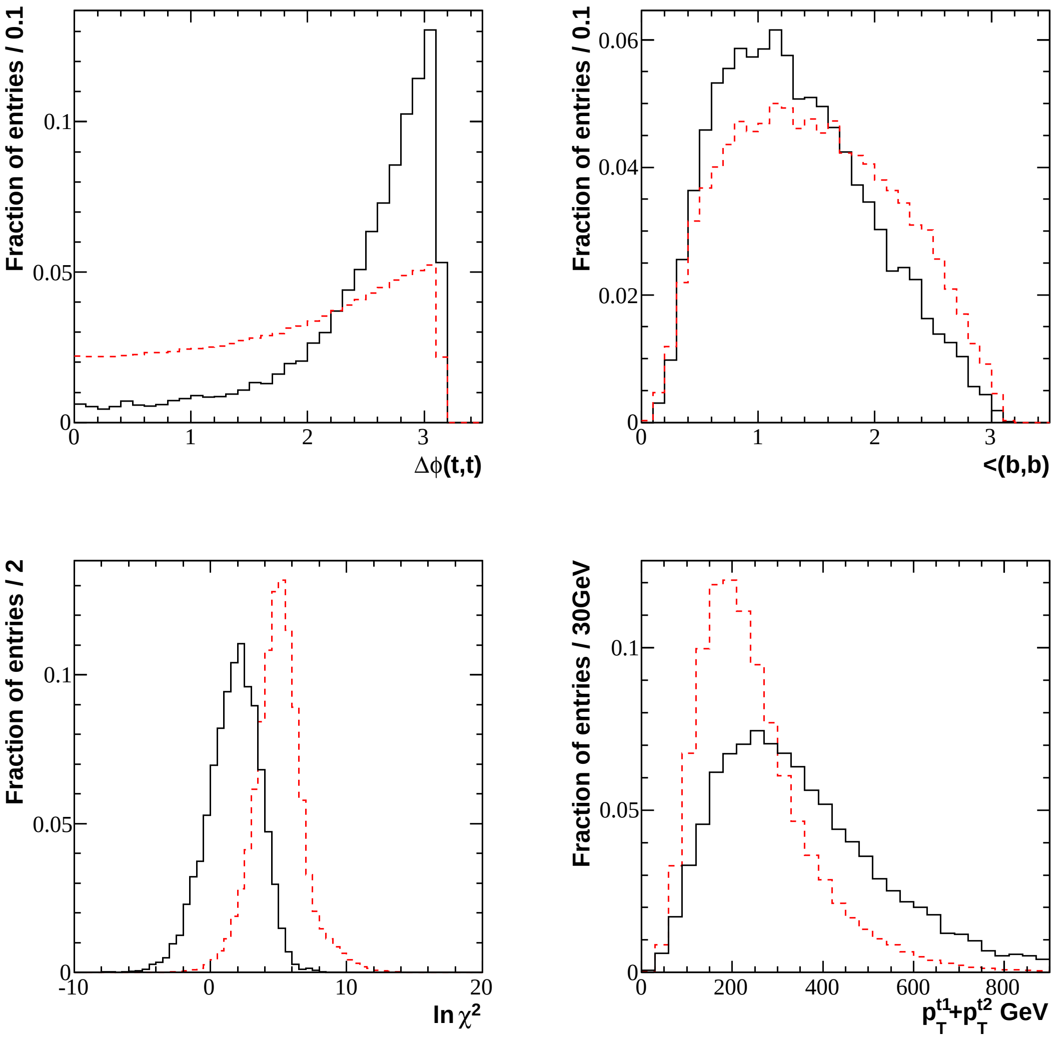

Figure 6.29: Histograms showing potential likelihood variables for correct (black/solid) and incorrect (red/dashed) jet combinations. All distributions are normalised to unit area.

larger. Figure 6.31a displays the correct histograms from figure 6.30 superimposed. Events in the very centre of the peak have been lost by choosing the neutrino using p_z and extra have been gained further from the top mass. The percentage of events where the correct neutrino is chosen in the case of minimising $|m_{l\nu b} - m_t|$ is 67% compared to 62% for p_z. By losing the potential problem in the background, a lot of events where the reconstructed top mass would be very close to the nominal top mass, have also been lost. It is interesting to note that a small peak at the top mass is present in the correct neutrino distribution in figure 6.31b.

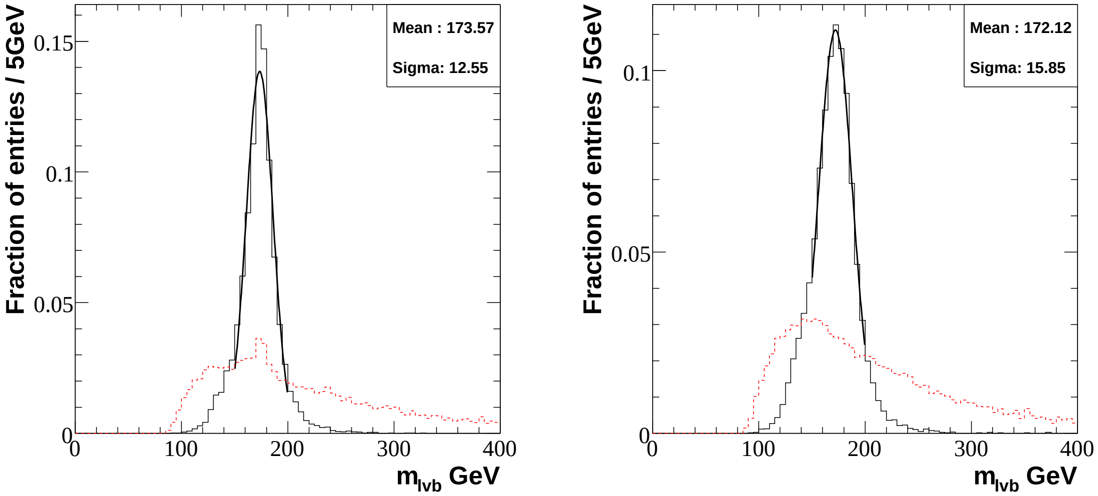

Figure 6.30: Histograms showing the invariant mass of the semi-leptonic top-quark for the correct jet pairing (black/solid) and the incorrect jet pairings (red/dashed). The neutrino solution used in the reconstruction is chosen by minimising $|m_{l\nu b} - m_t|$ in the left hand plot and by the lowest p$_z$ on the right.

Four likelihoods will be tested to compare to the χ^2 minimisation in the previous section. These are a combination of the variables:

1. m_{jj}, m_{jjb}, $m_{l\nu b}$, $\Delta R(b, jj)$, $\Delta R(b, l)$, $< (j, j)$
2. m_{jj}, m_{jjb}, $m_{l\nu b}$, $\Delta R(b, jj)$, $\Delta R(b, l)$, $< (j, j)$, $\Delta\phi(t, t)$, $p_T^{t1} + p_T^{t2}$
3. ln χ^2, $\Delta R(b, jj)$, $\Delta R(b, l)$, $< (j, j)$
4. ln χ^2, $\Delta R(b, jj)$, $\Delta R(b, l)$, $< (j, j)$, $\Delta\phi(t, t)$, $p_T^{t1} + p_T^{t2}$

Instead of requiring the hadronic W and reconstructed tops to be within a certain mass range, a cut will be made on the value of the likelihood output instead. For a baseline comparison amongst the above alternatives, this was chosen to be $\mathcal{L} > 0.7$ as in [51]. The likelihood output distributions for the correct and incorrect jet pairings of the first two likelihoods are shown in figure 6.32. The distributions have a peak for the signal at zero that is not present in the distribution in [51], however the increase in significance by the improvements proposed were found to be similar in this analysis. The 'collinear approximation' increased the significance by 13%

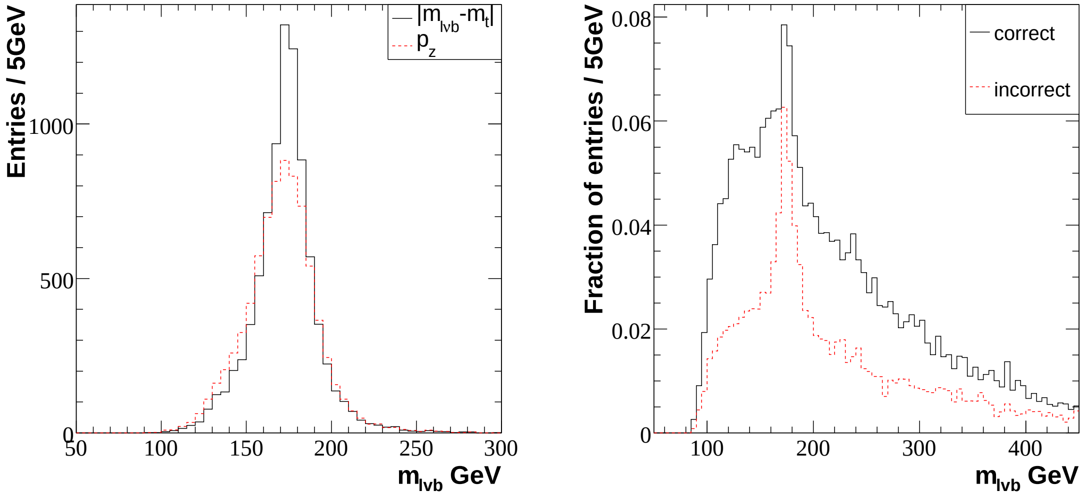

Figure 6.31: (a) Histogram showing the semi-leptonic top-quark mass for cases where the correct jet pairing and correct neutrino solution are used in the reconstruction. The solid line minimises $|m_{l\nu b} - m_t|$ to choose the neutrino solution and the dashed line is where the neutrino solution with the lowest p_z is selected. (b) The variable $\mathrm{m}_{l\nu b}$ for the wrong jet combinations using the correct (black) and incorrect (red) neutrino solution for the reconstruction.

over that in the TDR method compared to an increase in 15% reported in [51]. The likelihood function produced an extra increase of 16% exactly as found in [51].

The results for the four likelihoods are shown in table 6.10. The χ^2 results compare favourably with the likelihoods containing this variable (3 and 4). The final significances are similar, but the percentage of correctly reconstructed Higgs bosons within the mass window is higher for the χ^2 minimisation, especially considering the higher event numbers passing the final cut for this method. The likelihood proposed in [51] performs better with a final significance of 2.31 and 67.7% of signal events having a correctly reconstructed Higgs boson. The addition of the two extra variables into this likelihood manages to retain the number of signal events whilst decreasing the number of background events slightly at the expense of a small decrease in the reconstruction purity. The $\mathcal{L} > 0.7$ cut efficiency has a lower value than the 88% reported in [51] for all the likelihoods. This is due to the changes in the reconstruction of the hadronic W candidates, as without these an 88% efficiency and significance of 2.34 for the original likelihood is obtained. This efficiency could

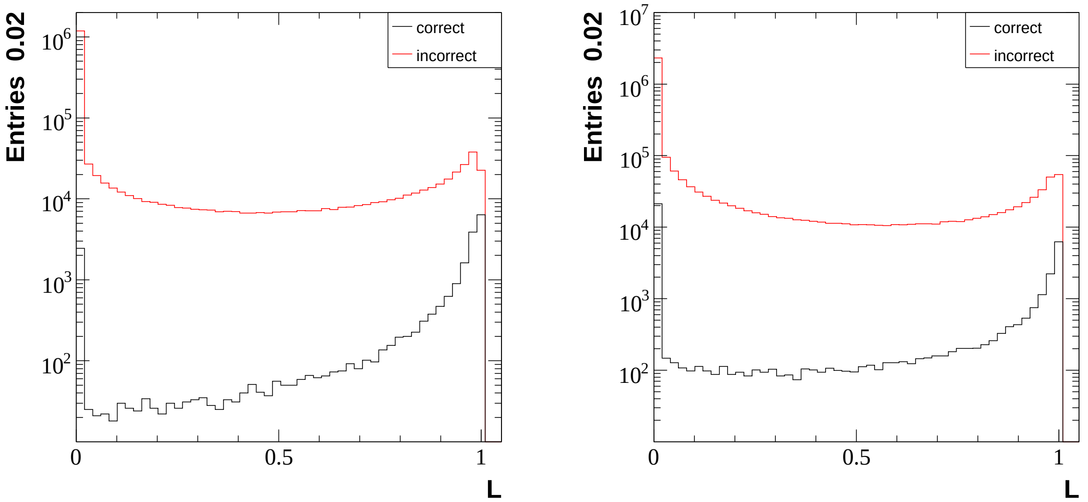

Figure 6.32: Distribution of the likelihood output for correct and incorrect jet pairings. The left hand plot corresponds to the first likelihood in the list and the right hand plot the second.

possibly be regained by recalculating the pdf distributions with the W candidate changes or by optimising the $\mathcal{L}$ cut.

		S	B	$s/\sqrt{B}$	% correct	$\mathcal{L}$ >0.7 efficiency (%)
χ^2		45.5	431.7	2.19	65.2	-
Likelihood	1	45.7	388.9	2.31	67.6	81.6
	2	45.7	384.5	2.33	65.2	80.9
	3	43.8	394.6	2.20	61.8	78.7
	4	44.3	408.4	2.19	64.7	79.4

Table 6.10: Number of signal events, number of background events, significance and the percentage of correctly reconstructed Higgs decays in the mass window for the four likelihood combinations and the χ^2 minimisation. The efficiency of the cut on the likelihood output is also given.

The effect of removing the restriction on the neutrino solution used for the reconstruction was gauged for the first likelihood. Here a slight increase in the number of background events was coupled with a small decrease in the number of signal events. The quality of the reconstruction in the signal was not effected. The effect of the hadronic W mass cut on this method was also gauged, the results of this are shown in table 6.11. This had little effect on the quality of the reconstruction, but a decrease in event numbers was observed. This was greater in the signal than in the background.

		S	B	s/$\sqrt{B}$	% correct
χ^2		45.5	431.7	2.19	65.2
Likelihood	1	44.9	388.6	2.28	67.9
	2	45.2	381.9	2.32	65.2
	3	43.2	386.4	2.19	61.7
	4	43.6	399.6	2.18	64.7

Table 6.11: Number of signal events, number of background events, significance and the percentage of correctly reconstructed Higgs decays in the mass window for the four likelihood combinations using a hadronic W mass cut and the χ^2 minimisation.

Overall the likelihood proposed in [51] performs better than the simpler χ^2 minimisation. The addition of the extra variables $\Delta\phi(t,t)$ and $p_T^{t1} + p_T^{t2}$ looks to be a promising improvement to the likelihood method.

6.6 Final Event Selection

For the final event selection, an Artificial Neural Network (ANN) was tested to select signal from background events. An overview of Artificial Neural Networks is given in appendix A. The ANN will be applied to events reconstructed using the χ^2 minimisation with the 'collinear approximation' applied as discussed in section 6.5.2. Variables investigated for inclusion in the ANN are shown in figure 6.33. These are:

$\boldsymbol{m_{bb}}$ The invariant mass of the pair of jets assigned to the Higgs boson decay.

$\boldsymbol{p_T^H}$ The $\mathrm{p_T}$ of the reconstructed Higgs boson.

$\boldsymbol{\cos\theta^*(b,b)}$ The cosine of the angle between the reconstructed Higgs boson in the lab frame and one of the b-jets assigned to its decay in the rest frame of the Higgs.

$\boldsymbol{\Delta\eta(t_{near},bb)}$ The difference in η between the reconstructed Higgs boson and the nearest top-quark in ΔR.

$\boldsymbol{\Delta\eta(b,b)}$ The difference in η between the two jets assigned to the Higgs boson decay.

$\boldsymbol{m_{bb}^1}$ The combination of two b-jets with the smallest invariant mass out of all the possible b-jet combinations in the event.

$\boldsymbol{m_{bb}^2}$ The combination of two b-jets with the second smallest invariant mass out of all the possible b-jet combinations in the event.

$\boldsymbol{\phi_{t1}-\phi_{t2}}$ The difference in ϕ between the two top-quarks.

$\boldsymbol{p_T^{t1}+p_T^{t2}}$ The sum of the $\mathrm{p_T}$ of the two top-quarks.

The variable $\cos\theta^*(b,b)$ should have a flat distribution when the two b-jets are produced from the decay of a spin-0 particle such as the Higgs boson. In the case of

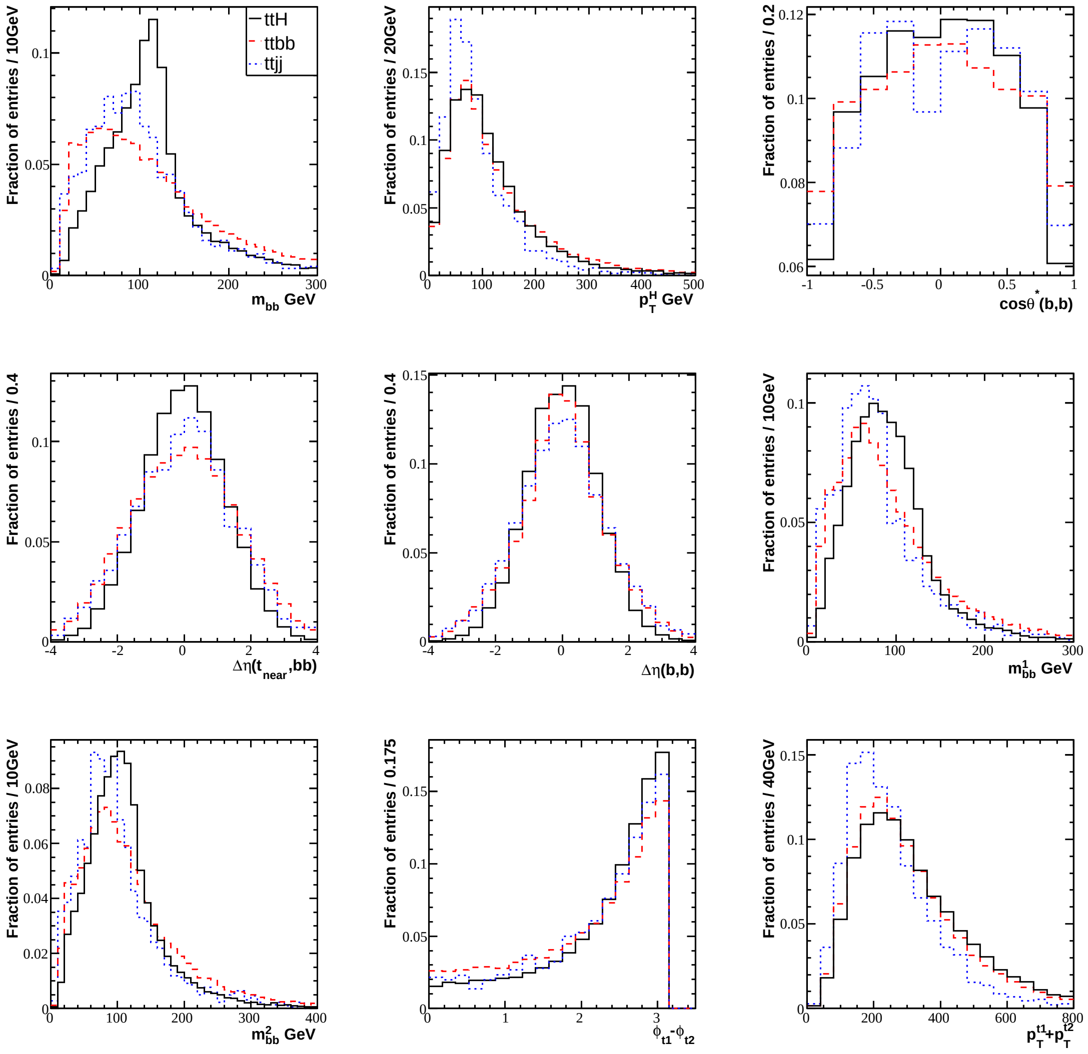

Figure 6.33: Variables investigated for inclusion in the ANN. Distributions are normalised to unit area. The signal (m$_H$=120GeV), $gg \to t\bar{t}b\bar{b}$ and $t\bar{t}jj$ distributions are shown for each variable.

jets produced from the decay of a spin-1 particle, such as gluons, this distribution should be peaked at -1 and 1. In this case the distributions do not display this behaviour, due to incorrect assignment of jets in a large number of events during the reconstruction. Since the background distributions still differ from the signal, it was decided to include this variable in the ANN.

The training and validation samples consist of five thousand events each. Events within the sample alternate between signal (m$_H$=120GeV) and background. The background events comprise $gg \to t\bar{t}b\bar{b}$, $t\bar{t}jj$, and $gg \to Z/W/\gamma^* \to t\bar{t}b\bar{b}$ events in the ratio 14:9:2 evenly mixed within the sample.

The network is trained using the first sample and its performance tested using the validation sample. The output of the error function that is being minimised is monitored after every ten iterations of the training cycle. The total number of training iterations is selected to be greater than the point where the error function reaches a minimum, but before the ANN beings to memorise the training set and the error function, calculated from the validation sample, begins to increase.

Initial training of a network, incorporating all the variables listed above demonstrated that $\cos\theta^*(b,b)$ and $\phi_{t1} - \phi_{t2}$ had little effect on the ANN performance. It was decided to remove these inputs from the network. The final network configuration is shown in figure 6.34. It has five input variables: m_{bb}, p_T^H, $\Delta\eta(t_{near}, bb)$, $\Delta\eta(b,b)$, $p_T^{t1} + p_T^{t2}$ and two hidden layers; the first with eight nodes and the second with six.

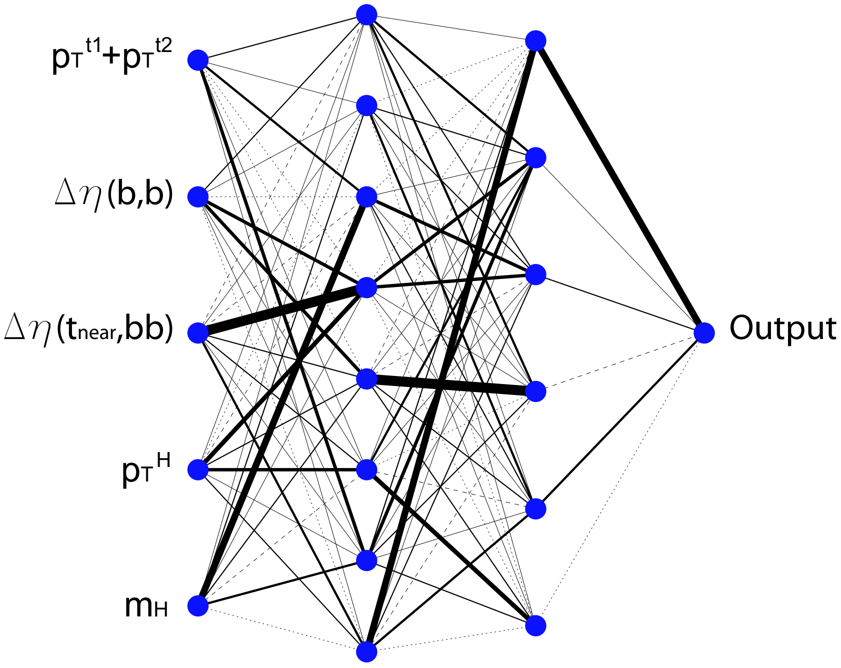

Figure 6.34: A diagram showing the final ANN layout.

The output of the trained ANN for signal and background events is shown in figure 6.35a. Figure 6.35b shows the corresponding signal and background efficiencies obtained by scanning over the range of possible cuts on the neural network output.

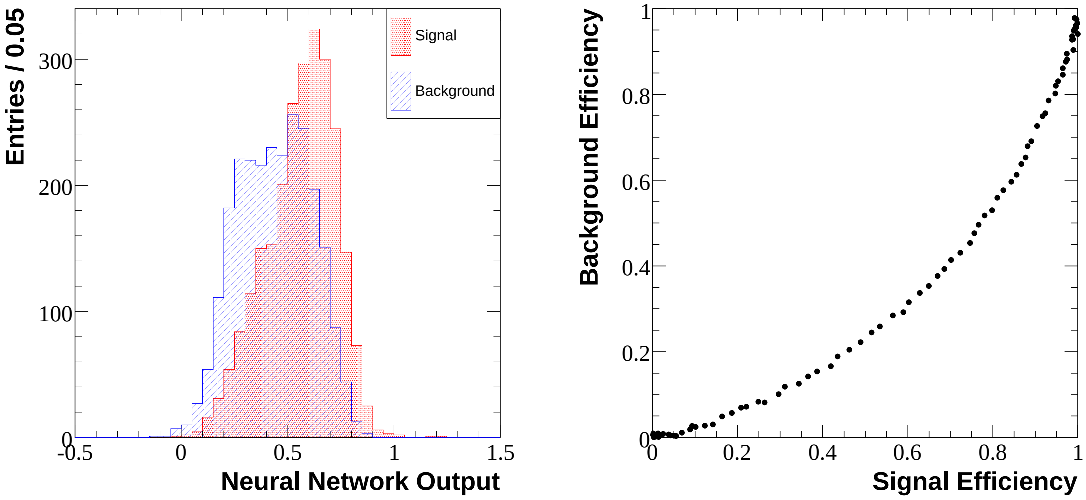

Figure 6.35: (a) The ANN output for signal (red-dotted histogram) and background (blue-striped histogram) events. (b) Signal efficiency versus background efficiency for the trained ANN.

Figure 6.36 displays the Higgs mass distribution obtained using cuts of 0.4, 0.5, 0.6 and 0.7 on the neural network output. As the cut is tightened a peak in the signal rejected at the Higgs mass starts to appear. The layout of the neural network and the inputs used were chosen to minimise this feature. The variables m^1_{bb} and m^2_{bb} in particular made this feature worse as can be seen in figure 6.37.

To obtain the final results, each signal and background sample was run through the trained network separately. The efficiencies obtained (see table 6.12) for cut values ranging from 0.3 to 0.7 in increments of 0.05 were scaled to the expected number of events for an integrated luminosity of 30fb^{-1}. The resulting significance for each value of the ANN output cut used is shown in figure 6.38. The optimal cut on the neural network output is 0.4, increasing the significance from 2.19 to 2.65.

The TDR analysis employs a mass window cut at the final stage of ±30GeV around the nominal Higgs boson mass. This cut defines the region in which the Higgs

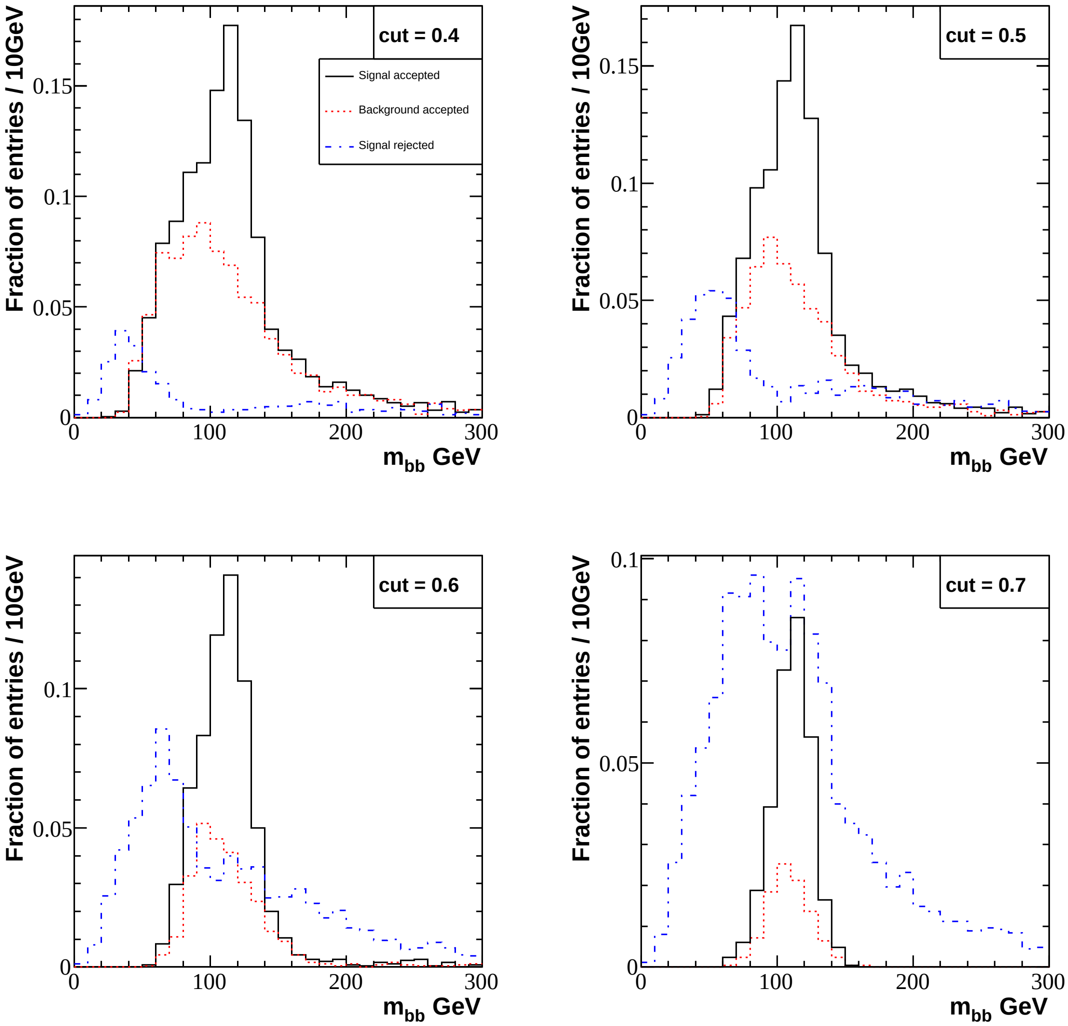

Figure 6.36: Signal events selected (solid line), background events selected (dashed line) and signal events rejected (dot-dash line) for events with ANN output above 0.4, 0.5, 0.6 and 0.7. The histograms are normalised to the number of signal/background events in the validation sample (2500).

boson signal significance will be evaluated. This region has to be defined in advance to avoid bias in the results. The use of mass windows centred on the nominal Higgs boson mass as carried out in the TDR is not realistic when considering real data. The use of many windows in which to carry out the search will reduce the significance of the result found, and as seen the reconstructed Higgs mass distribution does not peak at the nominal mass used. Figure 6.39a displays the significance obtained for each of the Higgs masses being studied in this thesis versus the mass of the

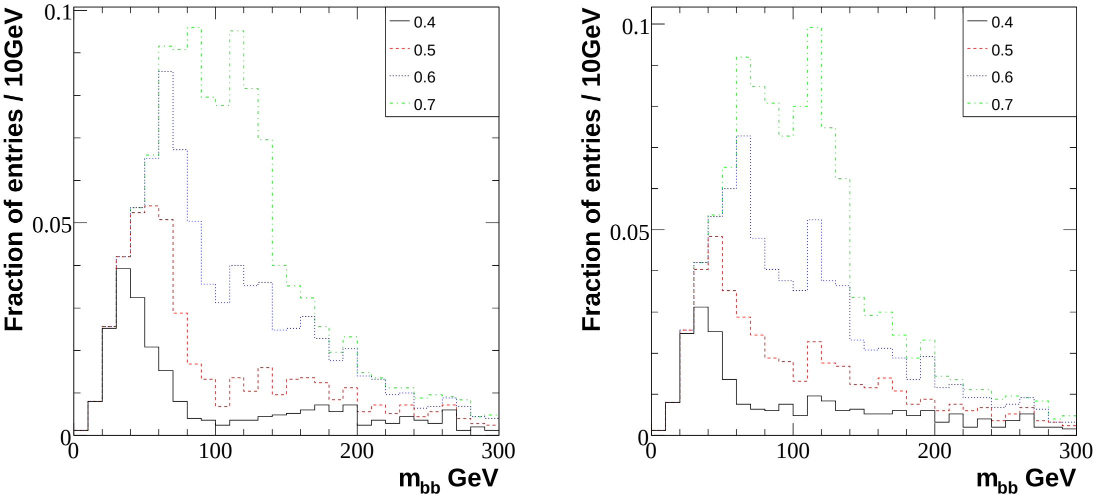

Figure 6.37: Distribution of m_{bb} for rejected signal events using cuts of 0.4, 0.5, 0.6 and 0.7 on the ANN output. The left hand plot is from the final trained network. The right hand plot is from a network incorporating the variables m^1_{bb} and m^2_{bb}.

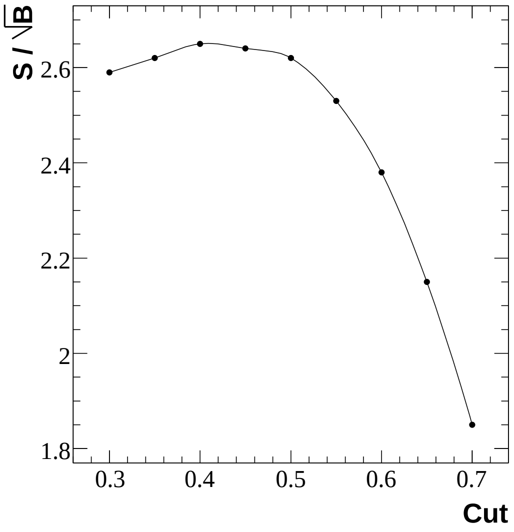

Figure 6.38: A graph showing the significance of the channel versus the cut used on the neural network output.

central point in the window used. As can be seen, the significance peaks around 10-15GeV lower than the nominal mass, but also the distributions are fairly flat such that a single window around 110GeV could be used for all Higgs masses. Figure 6.39b suggests that the significance of the channel would benefit from a larger mass window.

Cut	Efficiency			
	$t\bar{t}H^0$ (120)	$t\bar{t}b\bar{b}$ (QCD)	$t\bar{t}jj$	$t\bar{t}b\bar{b}$ (EW)
0.30	0.93	0.78	0.80	0.78
0.35	0.88	0.68	0.70	0.69
0.40	0.82	0.58	0.59	0.59
0.45	0.74	0.48	0.49	0.49
0.50	0.66	0.38	0.39	0.39
0.55	0.55	0.28	0.30	0.29
0.60	0.43	0.19	0.21	0.19
0.65	0.30	0.12	0.13	0.11
0.70	0.20	0.07	0.07	0.06

Table 6.12: Corresponding signal and background efficiencies obtained by applying a cut on the ANN output.

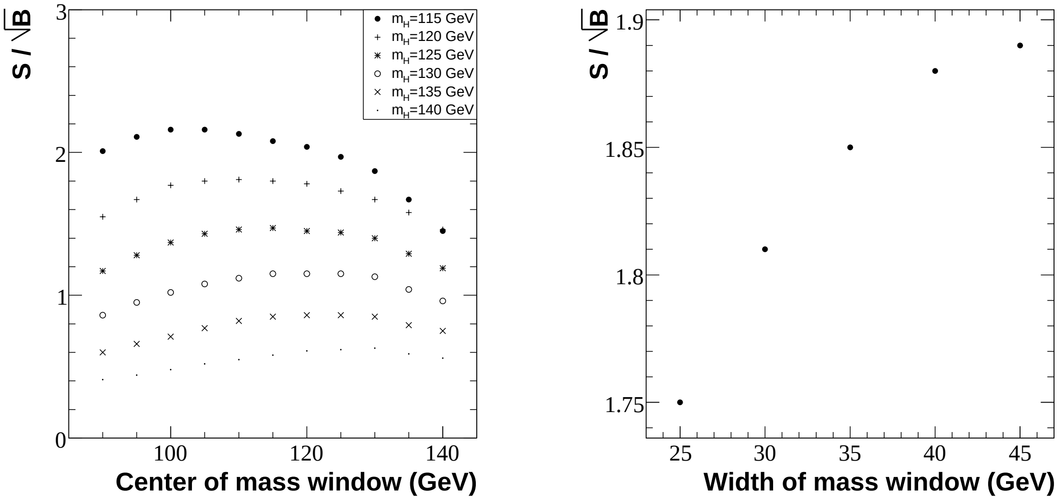

Figure 6.39: (a) The significance obtained versus the central value of the mass window used, for each of the Higgs masses studied in this thesis. (b) Significance obtained versus the width of a mass window centred on 110GeV, for a nominal Higgs mass of 120GeV.

The final reconstructed Higgs mass spectrum for signal and background combined is shown in figure 6.40 for cuts of 0.5, 0.6 and 0.7 on the neural network output. For the final results a Higgs mass window of 110±40GeV is applied with a cut of 0.5 on the neural network output (0.5 is optimal for use with the mass window). The significances obtained are shown in figure 6.41.

One issue that has to be considered relates to the use of the reconstructed Higgs boson mass distribution in the ANN. In order to carry out the search with real data it is necessary to have an accurate measurement of the background level and shape.

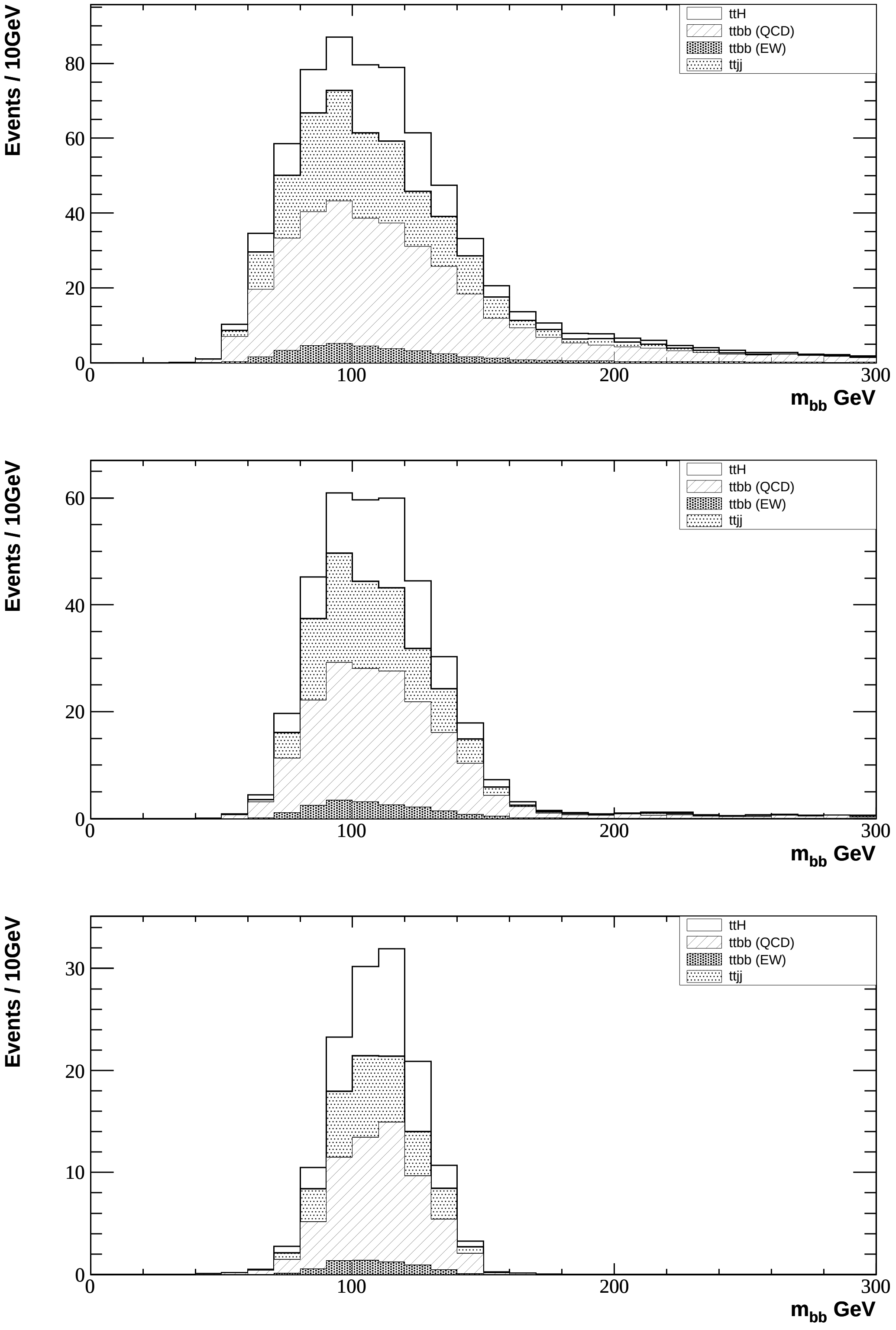

Figure 6.40: The reconstructed Higgs mass spectrum for signal and background events obtained when using the following cuts on the neural network output: 0.5 (top), 0.6 (middle) and 0.7 (bottom). The histograms are normalised to the expected number of events for L=30fb^{-1}.

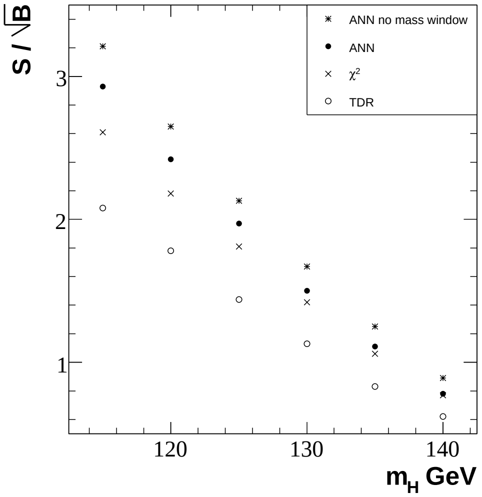

Figure 6.41: The significance of the $t\bar{t}H, H \rightarrow b\bar{b}$ channel over a range of Higgs boson masses; using the TDR analysis reconstruction method (open circles), using an updated method presented in this chapter (cross) and using this updated method with an ANN for the final event selection with a Higgs mass window cut of 110±40GeV (solid circles). The results from the ANN without the Higgs mass window cut and a neural network output cut of 0.4 (rather than 0.5) is also shown (asterisks).

By using m_H within the ANN, the shape of the background has been made to follow that of the signal. This could present an issue when trying to obtain an accurate description of the background shape, which is vital in evaluating the significance of the signal seen within the mass window defined. If this is the case, the ANN could have the effect of reducing the sensitivity of the channel to a Higgs boson due to the large systematic uncertainty on the backgrounds. This is an area that would need further study. If the background can be measured accurately the channel can benefit from an increased significance around the mass region with which the ANN was trained.

A summary of the effect of the methods and techniques studied in this chapter is provided in table 6.13.

Method	Change in significance (m_H=120GeV)
Hadronic W - incorporation of three jets	1.78 to 1.80
Hadronic W - energy rescaling	1.78 to 1.79
Correcting for semi-leptonic b-decays	1.78 to 1.72
χ^2	1.78 to 1.90
χ^2 with ‘collinear approx’	1.78 to 2.19
Likelihood with ‘collinear approx’	1.78 to 2.31
ANN with χ^2 and ‘collinear approx’ with mass window cut (110±40GeV)	1.78 to 2.42
ANN with χ^2 and ‘collinear approx’	1.78 to 2.65

Table 6.13: Summary of the gains or losses from each new method or technique studied in this thesis.

Chapter 7

Conclusions

For the ATLAS experiment, the channel $t\bar{t}H^0, H^0 \to b\bar{b}$ is one of the three that will contribute to the discovery of a Higgs boson in the low mass region $115 < m_H <$ 130GeV. This region is a particularly difficult region for a Higgs discovery, and all three channels are needed to achieve a 5σ observation. The channel requires full reconstruction of the two top-quarks in the event to reduce the large backgrounds. The channel has been previously studied in references [51],[20],[49],[50],[56]. In the most recent [51], the expected significance of the channel dropped from 3.6 as reported in the physics TDR [20] to 2.0 for a Higgs boson mass of 120GeV. This reduction, due to more realistic calculations of the cross-sections of both the signal and background, highlighted the need for improvements to the analysis procedure.

In this thesis the $t\bar{t}H^0, H^0 \to b\bar{b}$ channel was investigated using the fast simulation of the ATLAS detector, Atlfast. Improvements included changes to the reconstruction of the hadronic W candidates: the introduction of Ws created from three jets in the event and a new rescaling method. Rather than using the Δ^2 quantity used in the TDR analysis to select the correct jet pairing for the top-quarks, a new χ^2 quantity

$$\chi^2 = \frac{(m_{l\nu b} - m_t)^2}{\sigma^2_{l\nu b}} + \frac{(m_{jjb} - m_t)^2}{\sigma^2_{jjb}} + \frac{(m_{jj} - m_W)^2}{\sigma^2_{jj}}$$

was constructed using energy uncertainties for the jets and the lepton as parameterised within Atlfast. The top-quark mass cut was replaced by a cut on the χ^2, the optimum value being twenty. These three changes improved the TDR analysis significance from 1.78, as found in this analysis, to 1.9 with a small increase in the purity of the reconstructed Higgs boson mass distribution. With the addition of a correction to keep events with no neutrino solution [51] this value increased to 2.19.

The likelihood method used to reconstruct the top-quarks in [51] was reviewed and additional likelihood functions, including the use of the χ^2 quantity, were tested. The original likelihood outperformed the simple χ^2 minimisation, with a final significance of 2.31 compared to 2.19. The addition of two extra variables to the original likelihood produced a small increase in expected significance to 2.33, with a small drop in the purity of reconstructed signal events.

An Artificial Neural Network was built and trained to carry out the final event selection of signal from background. The ANN provided an effective separation of signal from background and combined with a wider mass window of 110±40GeV, resulted in an increase in significance from 2.19 to 2.42.

There is still a lot of work to be carried out on the $t\bar{t}H^0, H^0 \to b\bar{b}$ channel before the LHC starts running. One of the main areas of consideration is the improvement of the b-tagging efficiency. The requirement of four b-jets reduces the number of signal events by 92%, thus any improvement should have a large effect on the significance of this channel. Another major question involves how the $gg, q\bar{q} \to t\bar{t}b\bar{b}$ background level and shape can be determined. A strategy for obtaining this will be crucial to the effectiveness of this channel.

An overview of the Atlantis event display for the ATLAS experiment has been presented. One of the major areas of development carried out as part of this doctorate has been the adaption of the display for use in the 2004 Combined Test Beam. Development of an algorithm to obtain the detector geometry from the ATLAS computing framework, in a format readable by Atlantis, was carried out and methods to obtain event data in an 'online' mode were also investigated.

Future development of the display will centre around its use for detector commissioning. It has already been used to assist with the commissioning of the SCT barrel before its installation in the ATLAS cavern. There are also plans to use Atlantis for the Pixel and TRT cosmic tests.

Appendix A

Likelihood and Artificial Neural Network Methods

A.1 The Likelihood Method

The likelihood method is a technique used to separate different classes of events. It involves the use of a number of input variables, n_{var}, that are combined into a single output variable, known as $\mathcal{L}$, which is then used to discriminate between event classes.

For a class of events, j, the distribution of each variable, i, follows a probability density function $f_i^j(x_i)$. The distributions are normalised to unit area. The probability $p_i^j(x_i)$ that an event belongs to class j, when the variable i is measured to have value x_i is given by the likelihood:

$$p_i^j(x_i) = \frac{f_i^j(x_i)}{\sum_{j=1}^{n_{class}} f_i^j(x_i)}.$$

Once calculated for a given event the variables $p_i^j(x_i)$ are combined into a single quantity using the equation:

$$P^j(x_1, ..., x_{n_{var}}) = \prod_{i=1}^{n_{var}} p_i^j(x_i).$$

Finally, the combined likelihood, $\mathcal{L}$, is calculated using:

$$\mathcal{L}^j(x_1, ..., x_{n_{var}}) = \frac{P^j(x_1, ..., x_{n_{var}})}{\sum_{j=1}^{n_{class}} P^j(x_1, ..., x_{n_{var}})}.$$

If the variables used to construct the likelihood are uncorrelated, $\mathcal{L}$ can be interpreted as the probability of an event belonging to class j. If the variables are correlated, as is the case in this thesis, the quantity calculated is no longer a likelihood but can still be used to discriminate between classes.

A.2 Artificial Neural Networks

An Artificial Neural Network (ANN) is a mathematical tool inspired by the way biological systems, such as the brain, process information. The brain is an interconnected network of neurons, these are specialised cells that are able to transmit signals to neighbouring neurons through interconnecting synapses. A neuron produces an output depending on the signals it receives from other neurons. An important aspect of neural networks is that the output from a neuron is a non-linear function of its inputs. The human brain consists of around 10^{11} neurons, with each neuron having between a few and a few thousand connecting synapses. An ANN has a far simpler structure but still provides a system that is able to learn by example and acquire knowledge to solve a specific problem, such as recognising a pattern or classifying data into types.

The architecture of a typical ANN (known as a multi-layer perceptron) is shown in figure A.1. An ANN is composed of a series of nodes that have multiple connections to each other. In a structured ANN the nodes are organised into input, output and hidden layers. Every node is connected to all of the nodes in the previous and next layers, but no connections exist between nodes in the same layer. Each connection has a weight associated with it that can be varied in strength. The input to a given node is the weighted sum of the outputs of the nodes in the previous layer. For example, the input to the the jth node in the first hidden layer is given by:

$$a_j = \sum_i w_{ij} z_i$$

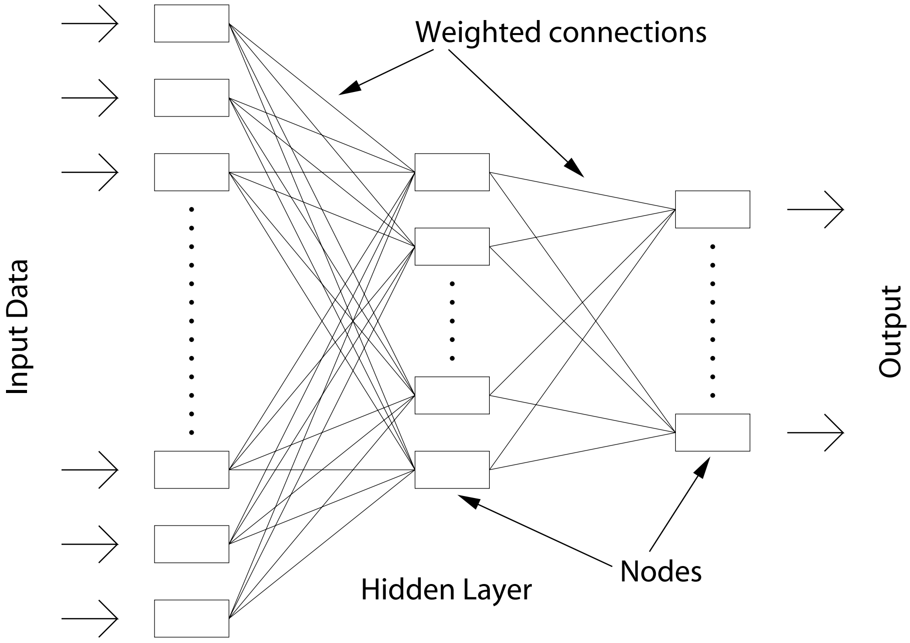

Figure A.1: Architecture of a multilayer perceptron.

where z_i is the output from the ith node in the input layer and w_{ij} is the weight of the connection between the two nodes. The output from this node is then:

$$z_j = f(a_j + W_{j0})$$

where $f(x)$ is a sigmoid function for example:

$$f(x) = \tanh(x) \quad \text{or} \quad f(x) = \frac{1}{1+e^{-x}}.$$

and W_{j0} is the bias or threshold of the node.

To obtain the desired output(s) from the network for a given set of inputs, it is necessary to train the network. Supervised learning is where both the input data and associated output data are presented to the ANN. The ANN calculates its output according to the current weights within the network and compares this to the desired output. The weights are then updated in such a way that the ANN produces an output as close as possible to the desired one. The aim of training the network is to produce a generalised mapping so the trained network can be applied to a new set of data for which the outputs are not known.

The training of an ANN involves the minimisation of an error function using a technique such as the gradient descent method. This process can be divided into two distinct steps. For each training event it is first necessary to evaluate the derivatives of the error function with respect to each weight within the network. This is carried out using the back-propagation algorithm. The second stage involves the use of these derivatives to calculate the necessary adjustments to the weights in order to minimise the error function.

An overview of the back-propagation algorithm follows, this is a summary of the more detailed description found in [57]. The algorithm starts with an error function that is a differentiable function of the network outputs (y_i).

$$E = \sum_n E^n \quad \text{where} \quad E^n = E^n(y_1, ..., y_i)$$

The error is summed over the n data in the training set. The weights can be updated after all n events have been read or after each event. Since E^n only depends on the weights w_{ji} through the summed input a_j to unit j, the differential of the error with respect to the weight is:

$$\frac{\partial E^n}{\partial w_{ji}} = \frac{\partial E^n}{\partial a_j}\frac{\partial a_j}{\partial w_{ji}}$$

Using,

$$\frac{\partial E^n}{\partial a_j} \equiv \delta_j \quad \text{and} \quad \frac{\partial a_j}{\partial w_{ji}} = z_i,$$

the partial derivative of the error function with respect to each weight can be calculated using:

$$\frac{\partial E^n}{\partial w_{ji}} = \delta_j z_i,$$

where z_i is the output from node i in the previous layer. For the output units δ_j is simply:

$$\delta_k \equiv \frac{\partial E^n}{\partial a_k} = f'(a_k)\frac{\partial E^n}{\partial y_k},$$

whereas for hidden units this becomes:

$$\delta_j \equiv \frac{\partial E^n}{\partial a_j} = \sum_k \frac{\partial E^n}{\partial a_k}\frac{\partial a_k}{\partial a_j},$$

where k is the index for all units to which j sends information. This generalises to

$$\delta_j = f'(a_j) \sum_k w_{kj} \delta_k,$$

which allows the δ for a particular hidden unit to be obtained by propagating the δ values backward though the network.

A typical error function is the summed square error:

$$E = \frac{1}{2} \sum_i (y_i - t_i)^2$$

where y_i is the actual output and t_i is the target output. The updates to the weights using the gradient descent method are then given by:

$$\Delta w_{ij} = -\eta \frac{\partial E}{\partial w_{ij}} = -\eta \delta_i z_j$$

where η is the learning rate parameter (η <1).

More detailed introductions to Artificial Neural Networks can be found in [58, 59]. The training method used in this thesis was the Broyden-Fletcher-Goldfarb-Shanno (BFGS) method for minimisation (a description can be found in [57]). The Artificial Neural Network implementation used is the TMultiLayerPerceptron within ROOT [60].

APPENDIX B

Atlantis Paper in the Computing in High Energy Physics 2004 Conference Proceedings

THE ATLANTIS VISUALISATION PROGRAM FOR THE ATLAS EXPERIMENT

J. Drohan, J. Couchman, N. Konstantinidis, Z. Maxa, University College London
Hans Drevermann, CERN
F. Crijns, E. Jansen, P. Klok, C. Timmermans, University of Nijmegen
D. Petrusca, G. Taylor, UC Santa Cruz

Abstract

We describe the philosophy and design of Atlantis, an event visualization program for the ATLAS experiment at CERN. Written in Java, it employs the Swing API to provide an easily configurable Graphical User Interface.

Atlantis implements a collection of 2D/3D data-orientated projections which enable the user to quickly understand and visually investigate complete ATLAS events. Event data is read from XML files, produced by a dedicated algorithm running in the ATLAS software framework ATHENA, and translated into internal data objects. Multiple views of the data can be displayed within the main canvas area, with varying size and position. Interactions such as zoom, selection and query can occur between these views using Drag and Drop.

Associations between data objects, as well as the values of their member variables, provide criteria upon which the Atlantis user may filter a full Atlas event. By choosing whether or not to show certain data, and if so in what colour, a more personalised and useful display may be obtained. The user can dynamically create and manage their own associations and perform context dependent operations upon them.

INTRODUCTION

Atlantis is an event display for the ATLAS experiment at CERN. When the LHC starts running in 2007, it will collide protons with a centre of mass energy of 14TeV at a bunch crossing rate of 40MHz. At the design luminosity of $10^{34}\mathrm{cm}^{-2}\mathrm{s}^{-1}$ there will be approximately 23 interactions per bunch crossing. Atlantis aims to provide easy, fast, error free visual investigation and physical understanding of these complicated events. This involves enabling the user to understand and check aspects of the reconstruction such as clustering, tracking and associations between data objects, e.g. tracks to clusters.

PROGRAM OVERVIEW

Atlantis is a Java application employing the Java2D package for graphics and Swing for the Graphical User Interface (GUI). The main Atlantis canvas is a layered panel, allowing multiple projections to be displayed on the screen at once, with varying size and position. These displays can be adjusted within the GUI by the graphical window controls and they can be moved between positions using Drag and Drop.

Access to Event Data

Atlantis reads events from XML files. At present, these files are created by a dedicated algorithm, JiveXML, running in the ATLAS software framework ATHENA. This algorithm runs after full reconstruction or fast simulation and produces one file per event. These files can either be read locally by Atlantis or accessed over a network, either as XML or within a zip file. JiveXML can also act as an XMLRPC server to send files directly to Atlantis. A design luminosity event is approximately 20MB in size, or 4MB compressed within a zip.

Detector Geometry

Atlantis displays an idealised detector geometry to rapidly convey the context in which hits are to be viewed. This information is read at startup from an XML configuration, enabling Atlantis to be easily extended for use with different geometry setups such as test beams.

Interactions

Atlantis provides the user with the following mouse based interactions, made available by selecting the corresponding tab on the GUI (Figure B.1).

Zoom/Move/Rotate (ZMR) Zooming is carried out with respect to a central position specified by the user. Mouse modifier keys M and R enable use of the Move and Rotate functions.

Rubberband Rubberbands provide an alternative method for zooming by drawing a band around the region of interest. A summary of data contained within the area is available as an option.

Pick This interaction allows selection of hits and tracks or detectors. It also provides the ability to navigate to selected data in different projections.

Fisheye Transformation This is a radially dependant zoom allowing relative magnification of the inner detectors without increasing the outer radius (Figure B.2).

Clock Transformation This is an angular fisheye transformation that allows a selected azimuthal region to be shown in detail whilst still displaying the full 360^o.

Synchro-Cursors Cursors are simultaneously visible in all projections.

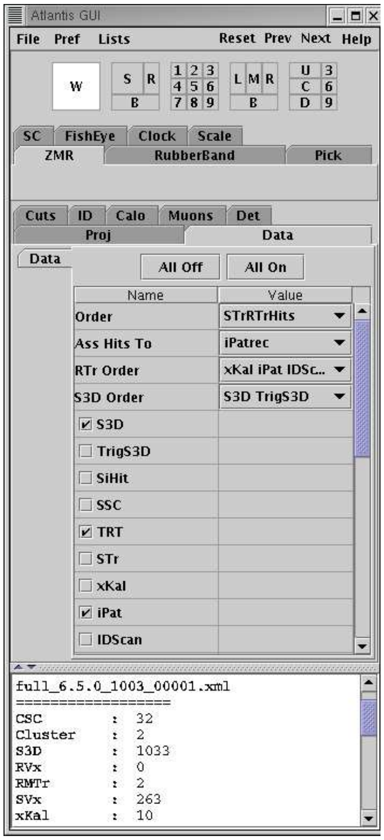

Name	Value
Order	STrRTrHits
Ass Hits To	iPatrec
RTr Order	xKal iPat IDSc...
S3D Order	S3D TrigS3D
☑ S3D	
☐ TrigS3D	
☐ SiHit	
☐ SSC	
☑ TRT	
☐ STr	
☐ xKal	
☑ iPat	
☐ IDScan	

```
full_6.5.0_1003_00001.xml
==================
CSC        :  32
Cluster    :  2
S3D        :  1033
RVx        :  0
RMTr       :  2
SVx        :  263
xKal       :  10
```

Figure B.1: The Atlantis Graphical User Interface.

Menus

The user interface contains a tabbed panel of menus for display manipulation (Figure B.1). The Data menu allows selection of the data types to be drawn on screen. It also allows for reordering of different track and hit types, e.g. reconstructed and simulated tracks. The Projection menu changes the projection in the current window and the Cuts menu allows data to be cut by parameter or association to other data types. There are a series of sub-detector specific menus which provide the ability to alter the colour, shape and size of data objects from that sub-detector and also to colour the objects by association.

The user can create a more useful display by using this ability to cut and colour objects in combination. For example, by selecting only hits belonging to truth tracks, and then colouring these by their association to reconstructed tracks, it is easy to see possible problems with track reconstruction and investigate the cause of unused truth hits.

Configuration and Image Output

Atlantis is easily configurable, offering the possibility to modify and save colour maps, projection/window setup and the GUI content. These saved settings are automatically loaded on startup. EPS, PNG and GIF image output is available.

DATA ORIENTATED PROJECTIONS

3D Cartesian coordinates are not always optimal for colliding beam experiments. Atlantis utilises a collection of 2D projections[1], including the intuitive Y/X, Y'/Z, X'/Z, ρ/Z projections as well as the more powerful but non-intuitive ϕ/ρ, ϕ/Z projections and the V-Plot (3D).

Y/X

The Y/X projection is an easily understandable projection looking along the beam line. This projection is useful to view tracks and hits in the inner silicon detectors, providing estimation of charge and P_T, and associating them to the TRT, LAr and TILE barrels. This projection is also useful to look at the Muon RPC ϕ-strips. Endcap information is not displayed for the calorimeters and muon system as these would fall ontop of the tracking and calorimeter barrel data, complicating the picture. Separate views in this projection are available for the muon endcaps and forward calorimeters (FCAL). Figure B.2 is the Y/X projection with a fisheye transformation applied.

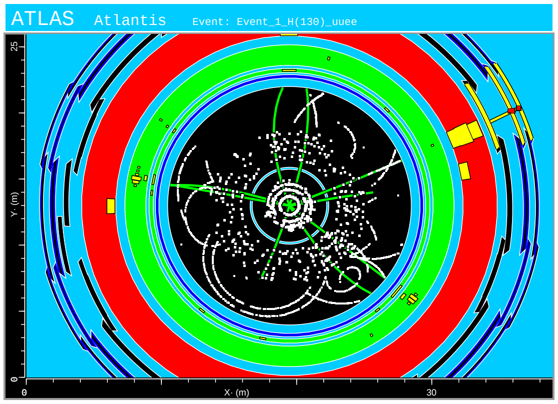

Figure B.2: The Y/X Projection with fisheye applied.

X'/Z

The X'/Z projection is a useful view for the muon system and vertex region. The eight muon sectors, both barrel and endcap, can be viewed individually. This enables comparisons between the reconstructed muon tracks and hits in the Monitored Drift Tubes (MDTs), seen as circles in this view (Figure B.3).

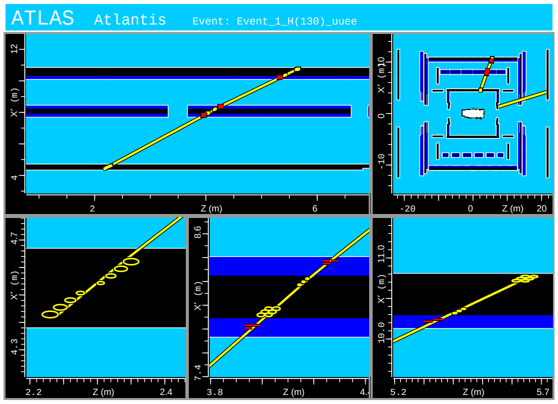

Figure B.3: The X'/Z Projection showing a single muon sector (top right), a zoomed view into the upper most muon track (top left) and a zoomed view for each muon MDT layer (bottom).

ρ/Z

The ρ/Z projection is the only projection where all the main detector units can be displayed without overlapping (Figure B.3). It enables the user to associate between inner detector hits and tracks and the full calorimeter system. It provides a rough association to muon data from all sectors superimposed. This is a non-linear projection but is intuitively understandable, with tracks from the origin taking the form of approximately straight lines.

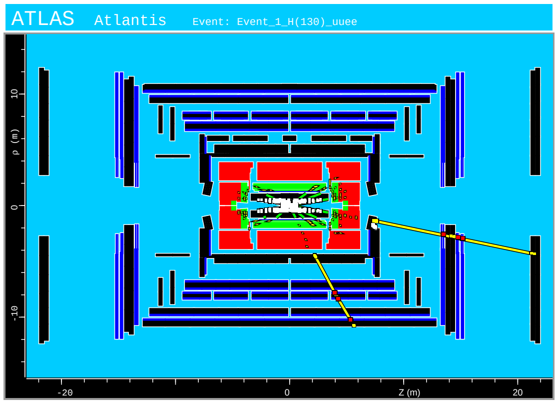

Figure B.4: The ρ/Z Projection.

ϕ/ρ

The ϕ/ρ can be regarded as a modified Y/X projection, with the same data being displayed in both. This is not an intuitive projection but allows a better angular separation of data from the innermost detectors. Pattern recognition is easier in this projection (Figure B.5) as helices are approximately straight lines. Tracks not pointing to the origin are distinctly non-linear when approaching ρ=0 and both the particle's charge and P$_T$ can be estimated from the track slope.

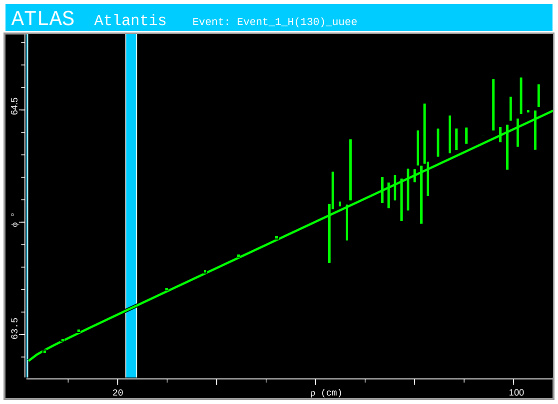

Figure B.5: The ϕ/ρ Projection showing a track in the inner detector.

V-Plot

The V-Plot is a modified form of the ϕ/η projection. ϕ/η provides optimal separation of tracks but doesn't provide charge, P$_T$ estimation or ρ information for hits. The V-Plot provides a solution to this, drawing two points for each single point on the ϕ/η plot using the equation

$\eta \pm kx(\rho_{max} - \rho)$, where ρ_{max} is normally the outer SCT radius. ϕ, η, ρ may be recalculated from each pair of points, making this a 3D projection. The following rules apply to interpret the V-Plot (Figure B.6).

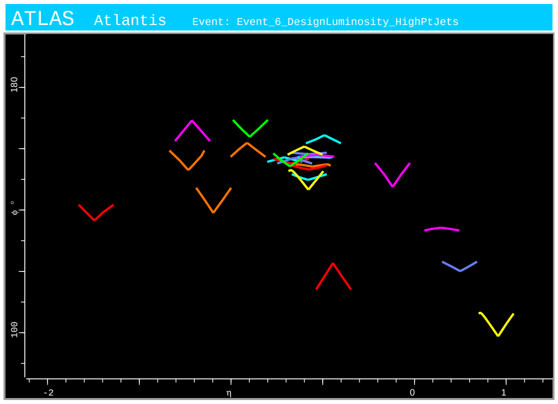

Figure B.6: The V-Plot.

- Helices transform into a V-like pattern.
- For helices pointing to the origin with not too low P_T the arms of the Vs are straight.
- For helices not pointing to the origin the arms of the Vs are curved, with the same sign of curvature for tracks separated from the origin in z and the opposite sign for tracks separated in ρ.
- Positive tracks give Vs pointing upwards.
- Negative tracks give Vs pointing downwards.
- The gradient of a V is proportional to $1/P_T$. High P_T tracks give Vs with an obtuse angle.

ADVANCED FEATURES

Filtering Algorithm

Within Atlantis it is possible to filter inner detector space points to remove those not consistent with tracks originating from a given primary vertex position (Figure B.7). The filtering algorithm is based on the fact that all hits of a track with sufficiently high P_T are contained in a small solid angle in (ϕ,η) that starts from the track's initial z position, in contrast to hits from tracks originating from different z positions. If enough hits are contained in a (ϕ,η) bin then they are accepted by the filter. This algorithm is extremely efficient and is now the basis of a fast tracking algorithm for the ATLAS Level 2 Trigger[2].

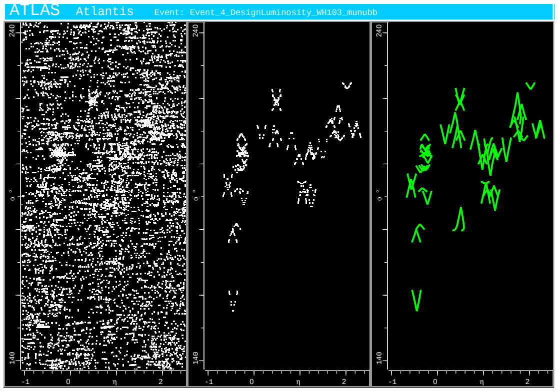

Figure B.7: V-Plot projection of a high luminosity event before (left) and after (middle) filtering. Reconstructed tracks for comparison (right).

Lists

Lists provide the user with the ability to dynamically create and manage their own associations. One of the main uses of lists is to construct secondary vertices from a group of reconstructed tracks.

3DBox Projection

The 3DBox projection allows the user to investigate a small 3D region around a newly formed secondary vertex (Figure B.8). The box is formed with default size (2mm x 2mm x 4mm) around the direction of flight of the incoming particle. The box contains three vertically orientated planes. The intersection of the planes and the tracks within the box are shown as ellipses representing the correlated impact parameter errors of the track. The user can zoom and rotate the area contained by the box to check the validity of the vertex.

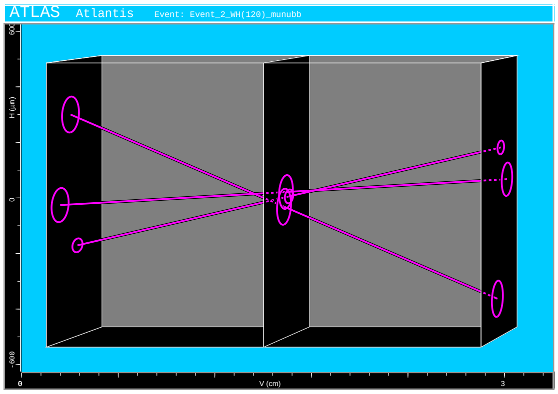

Figure B.8: The 3D Box Projection.

CONCLUSIONS

Atlantis is an event display tailored for the visual investigation of complete ATLAS events. It provides the user with a set of data orientated projections, including a modified form of the ϕ/η projection known as the V-Plot. Atlantis has an intuitive menu system, is fast and easy to use. The program is available to download from `www.cern.ch/atlantis`, along with documentation and a picture database.

REFERENCES

[1] H.Drevermann D.Kuhn B.S.Nilsson, 'Is there a Future for Event Display?', Proc. of 1992 CERN School of Computing, L'Aquila, Italy, CERN Yellow Report 93-03.

[2] N. Konstantinidis H. Drevermann, "Fast Tracking in Hadron Collider Experiments", ACAT, October 2000

Abbreviations

ANN Artificial Neural Network

API Application Programming Interface

CERN the European Organisation for Nuclear Research

CSC Cathode Strip Chambers

CTB Combined Test Beam

DOM Document Object Model

DTD Document Type Definition

ECAL Electromagnetic Calorimeter

EM Electromagnetic

EW Electroweak

FSR Final State Radiation

GUI Graphical User Interface

LAr Liquid Argon

LEP Large Electron Positron collider

LHC Large Hadron Collider

LVL1 First Level Trigger

LVL2 Second Level Trigger

MDT Monitored Drift Tube

QED Quantum Electrodynamics

QCD Quantum Chromodynamics

RoI Region of Interest

RPC Resistive Plate Chamber

SAX Simple API for XML

SCT Semi-Conductor Tracker

SM Standard Model

SPS Super Proton Synchrotron

TDR Technical Design Report

TDS Transient Data Store

TGC Thin Gap Chamber

TRT Transition Radiation Tracker

UML Unified Modelling Language

XML Extensible Markup Language

Bibliography

[1] R. Barate et al. Search for the standard model Higgs boson at LEP. *Phys. Lett.*, B565:61–75, 2003.

[2] OPAL Collaboration. Search for the standard model Higgs boson in e^+e^- collisions at $\sqrt{s} = 192$GeV - 209GeV. *Phys. Lett.*, B499:38–52, 2001.

[3] DELPHI Collaboration. Search for the standard model Higgs boson at LEP in the year 2000. *Phys. Lett.*, B499:23–37, 2001.

[4] ALEPH Collaboration. Final results of the searches for neutral higgs bosons in e^+e^- collisions at $\sqrt{s}$ up to 209-GeV. *Phys. Lett.*, B526:191–205, 2002.

[5] L3 Collaboration. Higgs candidates in e^+e^- interactions at $\sqrt{s}$=206.6GeV. *Phys. Lett.*, B495:18–25, 2000.

[6] The ALEPH, DELPHI, L3, OPAL, SLD Collaborations, the LEP Electroweak Working Group, the SLD Electroweak and Heavy Flavour Groups. Precision Electroweak Measurements on the Z Resonance. *Phys. Rept.*, 427:257, 2006.

[7] S.L. Glashow, J. Iliopoulos, and L. Maiani. Weak interactions with lepton - hadron symmetry. *Phys. Rev.*, D2:1285–1292, 1970.

[8] S. Weinberg. A model of leptons. *Phys. Rev. Lett.*, 19:1264–1266, 1967.

[9] P.W. Higgs. Broken symmetries, massless particles and gauge fields. *Phys. Lett.*, 12:132–133, 1964.

[10] P.W. Higgs. Broken symmetries and the masses of gauge bosons. *Phys. Rev. Lett.*, 13:508–509, 1964.

[11] F. Englert and R. Brout. Broken symmetry and the mass of gauge vector mesons. *Phys. Rev. Lett.*, 13:321–322, 1964.

[12] G.S. Guralnik, C.R. Hagen, and T.W.B. Kibble. Global conservation laws and massless particles. *Phys. Rev. Lett.*, 13:585–587, 1964.

[13] F. Halzen and A.D. Martin. *QUARKS AND LEPTONS: AN INTRODUCTORY COURSE IN MODERN PARTICLE PHYSICS*. John Wiley and Sons, 1984.

[14] W.N. Cottingham and D.A. Greenwood. *AN INTRODUCTION TO NUCLEAR PHYSICS*. Cambrige University Press, 1986.

[15] I.J.R. Aitchison and A.J.G. Hey. *GAUGE THEORIES IN PARTICLE PHYSICS. A PRACTICAL INTRODUCTION*. Bristol, UK: Hilger, 1982.

[16] M. Spira. QCD effects in Higgs physics. *Fortsch. Phys.*, 46:203–284, 1998.

[17] M. Quiros. Constraints on the Higgs boson properties from the effective potential. In G. L. Kane, editor, *Perspectives on Higgs Physics II*. World Scientific, 1997.

[18] J.A. Casas, J.R. Espinosa, and M. Quiros. Standard Model stability bounds for new physics within LHC reach. *Phys. Lett.*, B382:374–382, 1996.

[19] B.W. Lee, C. Quigg, and H.B. Thacker. The strength of weak interactions at very high-energies and the Higgs boson mass. *Phys. Rev. Lett.*, 38:883, 1977.

[20] ATLAS Collaboration. ATLAS Detector and Physics Performance Volume II. Technical report, CERN, May 1999. CERN-LHCC-99-15.

[21] S Asai, G Azuelos, C Buttar, V Cavasinni, et al. Prospects for the search for a Standard Model Higgs boson in ATLAS using vector boson fusion. *Eur. Phys. J.*, C32S2:19–54, 2004.

[22] J. Tanaka. Discovery potential of the standard model higgs at the lhc. *Nucl. Phys. Proc. Suppl.*, 144:341–348, 2005.

[23] LHC web site. http://lhc.web.cern.ch/lhc/.

[24] ATLAS Collaboration. ATLAS Detector and Physics Performance Volume I. Technical report, CERN, May 1999. CERN-LHCC-99-14.

[25] ATLAS Collaboration. ATLAS: Letter of intent for a general purpose pp experiment at the Large Hadron Collider at CERN. Technical report, CERN, 1992. CERN-LHCC-92-4.

[26] ATLAS Collaboration. ATLAS: Technical proposal for a general-purpose pp experiment at the Large Hadron Collider at CERN. Technical report, CERN, June 2003. CERN-LHCC-94-43.

[27] ATLAS Collaboration. ATLAS Inner Detector Technical Design Report. Technical report, CERN, April 1997. CERN-LHCC-97-16.

[28] ATLAS Collaboration. ATLAS Liquid Argon Calorimeter: Technical Design Report. Technical report, CERN, December 1996. CERN-LHCC-96-41.

[29] ATLAS Collaboration. ATLAS Muon Spectrometer: Technical Design Report. Technical report, CERN, June 1997. CERN-LHCC-97-22.

[30] ATLAS Collaboration. ATLAS level-1 trigger: Technical Design Report. Technical report, CERN, June 1998. ATLAS-TDR-12.

[31] ATLAS Collaboration. ATLAS high-level trigger, data acquisition and controls: Technical Design Report. Technical report, CERN, October 2003. CERN-LHCC-2003-022.

[32] H. Drevermann. DALI. http://aleph.web.cern.ch/aleph/dali/.

[33] H. Drevermann, B.S. Nilsson, and D. Kuhn. Is there a future for event display? In *CERN School of Computing*, pages 102–134, 1992. L'Aquila, Italy.

[34] ATLAS Collaboration. ATLAS Computing: Technical Design Report. Technical report, CERN, June 2005. CERN-LHCC-2005-022.

[35] N. Konstantinidis and H. Drevermann. Fast tracking in hadron collider experiments. In *7th International Workshop on Advanced Computing and Analysis Techniques in Physics Research*, Batavia, Illinois, October 2000.

[36] Xerces Java parser. http://xerces.apache.org/xerces-j/.

[37] B.D. Girolamo, M. Gallas, and T. Koffas. *ATLAS Barrel Combined Run in 2004 Test Beam Setup and its evolutions.*, February 2005. ATLAS Internal Note.

[38] M.D. Gomez, C. Padilla, I. Rui, and V.P. Reale. *Performance of the Second Level Trigger Electron Selection Algorithms with the 2004 ATLAS Combined Test Beam Data*, November 2005. ATLAS Internal Note.

[39] Torbjorn Sjostrand et al. High-energy-physics event generation with pythia 6.1. *Comput. Phys. Commun.*, 135:238–259, 2001.

[40] B. Andersson. The lund model. *Camb. Monogr. Part. Phys. Nucl. Phys. Cosmol.*, 7:1–471, 1997.

[41] B.P. Kersevan and E. Richter-Was. *The Monte Carlo event generator AcerMC version 2.0 with interfaces to* PYTHIA *6.2 and HERWIG 6.5*, 2004. hep-ph/0405247.

[42] G. Corcella, I.G. Knowles, G. Marchesini, S. Moretti, K. Odagiri, P. Richardson, M.H. Seymour, and B.R. Webber. HERWIG 6.5. *JHEP*, 0101(010), 2001.

[43] E. Richter-Was and D. Froidevaus. *Atlfast 2.0 a fast simulation package for ATLAS*, November 1998. ATLAS Internal Note.

[44] J. Drohan, N. Konstantinidis, Z. Maxa, H. Drevermann, J. Couchman, C. Timmermans, P. Klok, F. Crijns, G. Taylor, D. Petrusca, and E. Jansen. The Atlantis event visualisation program for the ATLAS experiment. In *Computing in High Energy Physics*, September 2004. http://atlantis.web.cern.ch/atlantis/.

[45] B. Mellado, G. Unal, and S.L. Wu. *Higgs Production Cross-Sections and Branching Ratios for the ATLAS Higgs Working Group*, October 2004. ATLAS Higgs WG Internal Note.

[46] M. Spira. The HQQ program. http://people.web.psi.ch/spira/hqq/.

[47] A. Djouadi, J. Kalinowski, and M. Spira. HDECAY: A program for Higgs boson decays in the standard model and its supersymmetric extension. *Comput. Phys. Commun.*, 108:56–74, 1998.

[48] H.L. Lai et al. Global QCD analysis of parton structure of the nucleon: CTEQ5 parton distributions. *Eur. Phys. J.*, C12:375–392, 2000.

[49] D. Froidevaux and E. Richter-Was. Is the channel H$\rightarrow b\bar{b}$ observable at LHC? *Z. Phys.*, C67:213–226, 1995.

[50] E. Richter-Was and M. Sapinski. Search for the SM and MSSM higgs boson in the $t\bar{t}H^0, H^0 \rightarrow b\bar{b}$ channel. *ATLAS Internal Note*, November 1998. ATL-PHYS-98-132.

[51] J. Cammin. *Study of a light standard model Higgs boson in the* $t\bar{t}H^0$ *channel with ATLAS at LHC and decay mode independent searches for neutral Higgs bosons with OPAL at LEP.* PhD thesis, University of Bonn, 2004. BONN-IR-2004-06.

[52] J.M. Butterworth, J.P. Couchman, B.E. Cox, and B.M. Waugh. Ktjet: A C++ implementation of the k_t clustering algorithm. *Comput. Phys. Commun.*, 153:85–96, 2003.

[53] F. James and M. Roos. 'Minuit' a system for function minimization and analysis of the parameter errors and correlations. *Comput. Phys. Commun.*, 10:343–367, 1975.

[54] A.I. Etienvre, J.P Meyer, and J. Schwindling. Top reconstruction and mass measurement. ATLAS Rome Physics Workshop, June 2005. http://prorm3.roma3.infn.it/atlas/apw/.

[55] ATLAS Collaboration. ATLAS Detector and Physics Performance Volume I, May 1999. Figure 6-16, page 190.

[56] A.N. Pickford. *b-quark tagging performance and Higgs detection via top production using the ATLAS detector.* PhD thesis, University of Glasgow, 2001.

[57] C. Bishop. *Neural Networks for pattern recognition.* Oxford University Press, 1995.

[58] C. Peterson and T. Rognvaldsson. An introduction to Artificial Neural Networks. In *CERN School of Computing*, Ystad, Sweden, August 1991.

[59] G. Mavromanolakis. *Neural networks technique based signal-from-background separation and design optimization for a W/quartz fiber calorimeter*, 2003. hep-ex/0303021.

[60] R. Brun and F. Rademakers. Tmultilayerperceptron. http://root.cern.ch/cgi-bin/print_hit_bold.pl/root/html/TMultiLayerPerceptron.html.